Prediction of concentrated vortex aerodynamics: Current CFD capability survey

James M. Luckring [a,1], Arthur Rizzi [b,2,*]

[a] NASA Langley Research Center, USA
[b] Royal Institute of Technology (KTH), Sweden

A B S T R A C T

Concentrated vortex flows contribute to the aerodynamic performance of aircraft at elevated load conditions. For military interests, the vortex flows are exploited at maneuver conditions of combat aircraft and missiles. For transport interests, the vortex flows are exploited at takeoff and landing conditions as well as at select transonic conditions. Aircraft applications of these vortex flows are reviewed with a historical perspective followed by a discussion of the underlying physics of a concentrated vortex flow. A hierarchy of computational fluid dynamics simulation technology is then presented followed by findings from a capability survey for predicting concentrated vortex flows with computational fluid dynamics. Results are focused on military and civil fixed-wing aircraft; only limited results are included for missiles, and rotary-wing applications are not assessed. Opportunities for predictive capability advancement are then reported with comments related to digital transformation interests. A hierarchical approach that merges a physics-based perspective of the concentrated vortex flows with a systems engineering viewpoint of the air vehicle is also used to frame much of the discussion.

1. Introduction

Vortex flows are a naturally occurring phenomenon in fluid dynamics. Concentrated vortex flows can be characterized by coherent vorticity and can be created from highly-swept sharp edges of a lifting surface. The concentrated vortex flow can be exploited for aerodynamic design purposes, and such use of these flows is referred to as vortex-flow aerodynamics; see Luckring [1], Rizzi [2], and AGARD [3].

Fundamental characteristics of a concentrated vortex flow can be studied with simple wing geometries such as a sharp-edged slender delta wing, Fig. 1. The flow is inherently three-dimensional, and the delta wing can generate all the flow physics entities of a concentrated vortex. In this regard, the delta wing serves much as a unit problem to understand the basic fluid mechanics as well as the aerodynamics of a concentrated vortex flow; it is a useful platform for flow physics measurements as well as CFD assessments. One of the best-established examples is the unit-aspect-ratio investigations performed by Hummel [4].

Aircraft can often develop separation-induced vortex flows at elevated load conditions. In some instances, these vortex flows have been exploited to augment high-lift or maneuver performance while, in others, they must be either tolerated as a byproduct of configuration design and/or operational requirement or possibly even avoided (Lovell [5]). One example of exploiting concentrated vortices is shown in Fig. 2 (a) for the F-16 aircraft. Separation-induced concentrated vortex flows are generated by a strake and persist over the wing to provide vortex lift increments at maneuver conditions. Fig. 2(b) shows a single vortex that is formed by an engine nacelle strake and that persists over the wing upper surface of a commercial transport in elevated loading. Concentrated vortices from nacelle strakes enhance wing high-lift performance at takeoff and landing conditions; they helped enable integration of high-bypass-ratio engines with commercial transport wings. In both examples, the vortices can be seen due to natural condensation effects. For other configurations and flow conditions, these concentrated vortex flows can become more complex and involve interactions among multiple vortices, between vortices and shocks, and between vortices and vehicle components.

Current design activity includes the interest for a digital engineering transformation whereby more of the aircraft design process can be accomplished with modelling and simulation and physical experimentation can be reduced to targeted needs or, in some domains, even eliminated. (See, Zimmerman et al. [6], Bone et al. [7], Hale et al. [8].) To realize this digital engineering goal, confidence in the modelling and simulation must be established for the operating conditions of interest. This is a daunting objective, given the many physical properties associated with an aircraft as well as the many operating domains of the

* Corresponding author.
E-mail address: rizzi@kth.se (A. Rizzi).
[1] Distinguished Research Associate.
[2] Emeritus Professor of Aeronautics.

Nomenclature

AR	aspect ratio
b	wing span
C_{fx}	Streamwise skin-friction coefficient
C_L	lift coefficient
$C_{L,max}$	maximum lift coefficient
C_m	pitching moment coefficient
C_p	pressure coefficient
$C_{p,le}$	leading-edge pressure coefficient
$C_{p,t}$	total pressure coefficient
c	wing chord
c_l	section lift coefficient
c_R	root chord
c_{ref}	reference chord
c_t	tip chord
D	diameter
d	length scale
f	frequency, Hz
h_{wm}	wall-modeled thickness
k	wave number, 2π/wavelength. Also, turbulent kinetic energy
M	Mach number
mac	mean aerodynamic chord
p	pressure
p_t	total pressure
$p_{t,\infty}$	freestream reference total pressure
Q	½ ($\|\|\Omega\|\| - \|\|S\|\|$)
q_w	wall heat flux
Re_c	Reynolds number, $U_\infty\, c/\nu$
Re_{cref}	Reynolds number, $U_\infty\, c_{ref}/\nu$
Re_D	Reynolds number, $U_\infty\, D/\nu$
Re_{mac}	Reynolds number, $U_\infty\, mac/\nu$
Re_τ	Reynolds number, $u^*\, \delta/\nu$
r/R_0	nondimensional radial distance from vortex core
r_{le}	leading-edge radius
r_N	leading-edge radius normal to leading edge
S	Entropy. Also, strain component of velocity gradient
s	semispan
T	temperature
t	time
t/c	thickness-to-chord ratio
U_∞	freestream reference velocity
u^*	wall friction velocity, $\sqrt{(\tau_w/\rho)}$
u,v,w	Cartesian velocity components
v_θ	circumferential velocity
x_{le}	longitudinal distance to leading edge
x_v	longitudinal distance to vortex separation
x,y,z	Cartesian coordinate system
α	angle of attack, degrees
β	angle of sideslip, degrees
γ	intermittency
Δ	increment. Also, grid spacing
δ	boundary layer thickness
δ_f	vortex flap deflection
ε	turbulent kinetic energy dissipation rate
η	semispan fraction, 2 y/b
$\Lambda_{c/4}$	quarter-chord sweep angle, degrees
Λ_{le}	leading-edge sweep angle, degrees
λ	taper ratio, c_t/c_R. Also, roll angle, deg
λ_2	second eigenvalue of the tensor $\mathbf{J} = [\mathbf{\Omega}^2 + \mathbf{S}^2]$
μ	viscosity
ν	kinematic viscosity, μ/ρ
ξ	fraction distance aft of leading edge, $(x\text{-}x_{le})/c$
ρ	density
σ	total angle of attack, deg
τ_w	wall shear stress
Ω	rotational component of the velocity gradient
ω	frequency scale for the turbulent fluctuations. Also, specific dissipation of k
$(\,)^+$	viscous inner-law-scaled quantity

Abbreviations

AFRL	Air Force Research Laboratory
AIAA	American Institute of Aeronautics and Astronautics
AMR	Adaptive Mesh Refinement
ARSM	Algebraic RSM
AVT	Applied Vehicle Technology
CAWAP	Cranked Arrow Wing Aerodynamics Program
CAWAPI	Cranked Arrow Wing Aerodynamics Program, International
CNRS	National Center for Scientific Research, *France*
CODA	CFD for Onera, DLR, and Airbus
CPU	Central Processing Unit
DES	Detached Eddy Simulation
DDES	Delayed DES
DLR	German Aerospace Center, *Germany*
DNS	Direct Numerical Simulation
DoD	Department of Defense
DoF	Degrees of Freedom
DRSM	Differential RSM
EADS	European Aeronautic Defense and Space Company
EARSM	Explicit Algebraic Reynolds Stress Model
EAS	Equivalent Air Speed
FC	Flight Condition
FOI	Swedish Defense Research Agency, *Sweden*
FS	Fuselage Station
GN&C	Guidance, Navigation, and Control
GPU	Graphical Processing Unit
HATP	High Angle-of-Attack Technology Program
HARV	High Alpha Research Vehicle
IDDES	Improved DDES
LBM	Lattice Boltzmann Method
LES	Large Eddy Simulation
LEX	Leading Edge Extension
M&S	Modelling and Simulation
NACA	National Advisory Committee on Aeronautics
NASA	National Aeronautics and Space Administration
NATO	North Atlantic Treaty Organization
ONERA	French Aerospace Lab, *France*
QCR	Quadratic Constitutive Relation
RANS	Reynolds-averaged Navier-Stokes
RC	Turbulence model rotation correction
RSM	Reynolds Stress Model
RTO	Research and Technology Organization
SA	Spalart-Almaras turbulence model
SST	Shear Stress Transport turbulence model
STO	Science and Technology Organization
TKE	Turbulent Kinetic Energy
TNT k-ω	Turbulent nonturbulent k-ω turbulence model
TUM	Technische Universität München, *Germany*
URANS	Unsteady RANS
USAF	United States Air Force
USN	United States Navy
V&V	Verification and Validation
VFFE	Vortex Flap Flight Experiment
VG	Vortex Generator
μVG	Micro Vortex Generator
WMLES	Wall-Modeled LES
WRLES	Wall-Resolved LES

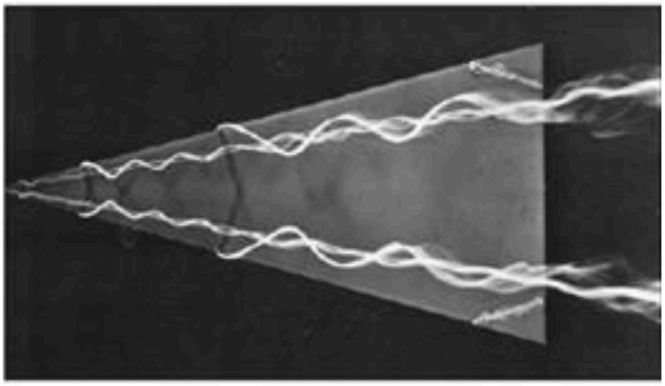

Fig. 1. Fundamental concentrated vortex flow. [Photo: courtesy of ONERA, reprinted with permission].

(a) Military aircraft. F-16, first flight in January 1974. [Photo: USAF, public domain]

(b) Commercial transport. A340-500, first flight in February 2002. [Photo: C. Frank Starmer, reprinted under Creative Commons License]

Fig. 2. Configuration applications of concentrated vortex flows.

aircraft.

With a down select to aircraft aerodynamics, one would require confidence in Computational Fluid Dynamics (CFD) for predicting vehicle performance. Some progress has occurred for cruise aerodynamics, but much less so for high-lift and maneuver conditions. This inhibits progress toward all-envelope CFD, and the problem is further exacerbated by the large number of conditions requiring simulation. (See, for example, Hitzel and Osterhuber [9], 2018.) With a further down select to concentrated vortex flow aerodynamics, confidence would be required for predictions of the concentrated vortex flows used not only on current aircraft but also on anticipated aircraft. The requirement for confident modelling and simulation of future concepts stresses a need to have the underlying physics correctly represented in the numerical technique.

In this article we present a review for the prediction of concentrated vortex flow aerodynamics using CFD. First, we review some fundamental considerations for concentrated vortex flows. Our approach to this part of the article is to summarize (i) the aircraft application interests for use of concentrated vortex flows, (ii) the fundamental physics of concentrated vortex flows, and (iii) the suite of CFD methodologies available to compute concentrated vortex flows. Next, we will present the findings from a survey of present capabilities to compute concentrated vortex flows. In addition to the authors' experience, the survey is based upon a literature database of over 6000 articles spanning approximately 20 years that was generated with the aid of the NASA Langley technical librarian staff. Finally, we will present some perspectives for a path forward to advance the prediction capabilities for concentrated vortex flows. A hierarchical approach that merges a physics-based perspective of the concentrated vortex flows with a systems engineering viewpoint of the air vehicle is used to frame much of the discussion.

The authors have selected survey results to report the state of the art of CFD predictive capability for concentrated vortex flows. These results come from a range of formulations spanning research codes to production software systems. Other notable findings from the survey have been excluded in the interest of brevity.

2. Review of concentrated vortex flow fundamentals

This section addresses three facets of concentrated vortex flow fundamentals. First, some terminology used through the report is reviewed, Subsection 2.1. Next, we summarize aircraft applications of concentrated vortex flows, Subsection 2.2. This includes both military and civil interests, and a historical development perspective is taken. Following this, we address the fundamental flow physics of concentrated vortex flows, Subsection 2.3. Finally, we review the hierarchy of modelling and simulation formulations available for the computation of concentrated vortex flow aerodynamics and include some representative applications, Subsection 2.4.

2.1. Terminology

The authors have chosen several definitions to clarify reporting for the prediction of concentrated vortex flow aerodynamics from modelling and simulation techniques. As regards concentrated vortex flow physics, we distinguish steady and unsteady concentrated vortex flows as follows:

- Steady concentrated vortex flow: a flow where the unsteadiness in the concentrated vortex is no greater than the unsteadiness associated with typical attached-flow turbulence.
- Unsteady concentrated vortex flow: a flow where the unsteadiness in the concentrated vortex is greater than the unsteadiness associated with typical attached-flow turbulence. Unsteadiness is further distinguished (i) as occurring due to vortical fluid dynamics for steady boundary conditions or (ii) as occurring due to unsteady boundary conditions (e.g., an oscillating wing).

The authors also refer to the coherence of a concentrated vortex flow:

- Coherent concentrated vortex flow: Elements of the concentrated vortex flow (e.g., shear layer, vortex core) are stable and steady. An example is the leading-edge vortex formed from a slender (highly-swept) sharp-edged delta wing at moderate angles of attack. Coherent concentrated vortex flows are stationary fluid structures.

- Semicoherent concentrated vortex flow: Elements of the concentrated vortex flow exhibit instability and unsteadiness within an otherwise organized vortical flow. An example is the leading-edge vortex formed from a not-so-slender (moderately-swept) sharp-edged delta wing at moderate angles of attack. Semicoherent concentrated vortex flows are still stationary fluid structures but with more extensive unsteady content than coherent concentrated vortex flows.
- Incoherent vorticity: Unsteady vorticity occurs without evidence of an organized vortical flow. An example is a bluff body wake. Incoherent vorticity is not a stationary feature because it is uncorrelated in time.

Concentrated vortex flows can be entirely coherent or semicoherent. They can also undergo a longitudinal change of state from coherence to semicoherence, such as due to the onset of vortex breakdown or shear-layer instabilities, and in some cases further devolve into a state of incoherent vorticity. Examples are discussed in the text.

The authors will distinguish among the hierarchy of modelling and simulation formulations (e.g., Direct Numerical Simulation, Large Eddy Simulation) and among formulations as methods (e.g., a Reynolds-averaged Navier-Stokes method). The article reviews predictive capability from modelling and simulation methods for concentrated vortex flows, and we will follow several definitions from either the AIAA Guide [10] or the ASME Guide [11] as summarized by Oberkampf and Roy [12]:

- Verification: The process of determining that a model implementation accurately represents the developer's conceptual description of the model and the solution to the model [10].
- Validation: The process of determining the degree to which a model is an accurate representation of the real world from the perspective of the intended uses of the model [10].
- Prediction: Use of a computational model to foretell the state of a physical system under conditions for which the computational model has not been validated [10].
- Calibration: The process of adjusting physical modelling parameters in the computational model to improve agreement with experimental data [11].

The authors will also refer to an *anchored* formulation as one with some degree of pedigree (historical applications, calibration history, validation history) for a new prediction.

2.2. Aircraft applications of concentrated vortex flows

Aircraft applications of concentrated vortex flows began shortly following World War 2 in association with the development of high-speed aircraft and persist to this day. The applications often take the form of a controlled vortical separation from the edge of a surface with elevated loading and can be thought of as a form of separation management. The concentrated vortex flows are exploited both for direct and induced effects, and the applications can occur from sub-boundary-layer flow scales to full configuration flow scales. Aircraft application interests are summarized in the following two subsections.

2.2.1. Military interests

The closing years of World War 2 saw the invention and deployment of jet-powered swept-wing combat aircraft. Interests in supersonic combat aircraft following this war led to the delta-wing concept, as presently known, and the subsequent invention of the area rule concept resulted in the first production jet-powered, slender-wing combat aircraft capable of supersonic flight, the F-102A, Fig. 3. A summary of this design evolution is included in an article by Luckring [1] regarding the discovery and prediction of vortex flow aerodynamics. The F-102A thin wing with a highly-swept leading edge was developed to enable

Fig. 3. Slender wing. F-102A, first flight in December 1954. [USAF, public domain].

supersonic flight and, as a by-product, these wings produced vortex lift increments at low speeds and high angles of attack. In work leading up to the F-102A, the experimental XF-92A delta-wing aircraft demonstrated in 1948 that (i) the vortex lift significantly reduced the landing speed requirements from what was expected for attached-flow aerodynamics and (ii) the naturally occurring separation-induced leading-edge vortices could be exploited for these purposes. This high angle-of-attack vortex lift could also be exploited for maneuver aerodynamics.

In the early 1970s, the development of highly-agile light-weight combat aircraft resulted in a hybrid-wing concept that combined attached-flow cruise aerodynamics with vortex-flow maneuver aerodynamics. Aircraft such as the F-16 (Fig. 2(a)) and, slightly later, the F-18 (Fig. 4) incorporated a slender sharp-leading-edge[3] lifting surface next to the fuselage that was integrated with a moderately-swept wing. The slender sharp-edged lifting surface was known as a strake, or leading-edge extension (LEX), At low-to-moderate angles of attack, the wing was designed following attached-flow principles. At high angle-of-attack maneuver conditions, the strake was designed to generate vortex lift from a concentrated leading-edge vortex following a concept of controlled separation (Polhamus [13]). The strake had only small effects on the attached-flow wing aerodynamics at cruise angles of attack, while, at maneuver angles of attack, the strake vortex not only developed significant vortex-lift increments but also delayed wing stall effects.

Controlled separation from strakes has been exploited at several scales for combat aircraft, and one example is shown in Fig. 5 for the Eurofighter. In this photograph, a body strake generates a concentrated

[3] More precisely, the leading edge is *aerodynamically* sharp. The leading-edge radius and thickness are sufficiently small to force leading-edge separation while meeting manufacturing tolerances. (See, Hirschel et al. [193], p136-139, for further discussion.) The same reasoning applies to an aerodynamically sharp trailing edge.

Fig. 4. Leading-Edge Extension, F–18C/D. F-18A/B, first flight in November of 1978. [USN, public domain].

Fig. 6. Maneuver vortex lift. Contemporary design. F-22, first flight in September 1997. [Photo: copyright Russell F Spencer, www.russellfspencer.com, reprinted with permission].

Fig. 5. Maneuver application of concentrated vortex flows. Eurofighter, first flight in March 1994. [Photo: Reddit.com, reprinted with permission].

Fig. 7. UCAV class, not-so-slender wing. nEUROn, first flight in December 2012. [Photo: wallspic.com, reprinted under Content Agreement License].

leading-edge vortex that persists aft along the upper portion of the fuselage. This strake was added to the aircraft to eliminate some high angle-of-attack maneuver deficiencies and resulted in an all-envelope maneuver capability of the Eurofighter. (See, Hitzel and Osterhuber [9].) In this application, the strake vortex was not used for vortex lift effects but to manipulate other separated flows on the airframe through vortex persistence. It should be noted that another vortex forms from the wing glove, below the body strake vortex, and this indicates that vortex interactions can also be an important consideration for combat aircraft.

More contemporary combat aircraft designs have introduced stealth considerations to vehicle shaping, and this has resulted in an increased extent of small-radius, or even sharp, edges on the airframe. The presence of these edges to support low observability interests also increases the presence of separation-induced vortical flows on the airframe. An example is shown in Fig. 6 for the F-22 raptor where separation-induced concentrated vortices are generated from the upper edges of the airframe inlet. These concentrated vortices form from a small-radius edge on a thick vehicle component (the inlet), and details of this vortical flow can be anticipated to be quite different from those of the sharp-edged and thin strakes just discussed. Sustained interest in stealth for current and future generation combat aircraft indicates that the separation-induced concentrated vortices will also have a sustained presence for combat aircraft.

Uninhabited Combat Air Vehicles (UCAVs) represent another contemporary class of combat aircraft that develop separation-induced vortex flows. An example is shown in Fig. 7 for the nEUROn vehicle. Observability considerations still result in wing geometries (e.g., sweep, leading-edge radius) that are conducive to forming separation-induced vortex flows at moderate to high angles of attack. However these vehicles include designs that fall in the not-so-slender class of wings with leading-edge vortices that are unsteady and burst for a greater part of the flight envelope. Because the vehicles are uninhabited, they can develop more extreme maneuvers that include higher rates and angles of attack and sideslip, further promoting unsteady and semicoherent vortex flows than for inhabited vehicles. The UCAV vehicle class stresses the attributes of concentrated vortex flows differently from inhabited vehicles.

A summary of combat aircraft leading-edge sweep values is shown in Fig. 8 as a function of first flight date, and several X-planes are included. Vehicles are dominated by the hybrid wing design concept that enables lower leading-edge sweep values for cruise performance along with the highly-swept surface (strakes, fuselage edges) to enable high angle-of-attack maneuver performance from the separation-induced concentrated vortex flows. It is also seen that the recent slender wing (non-hybrid) designs fall in a sweep range better characterized by not-so-slender wing flows. Designs from the mid-1990s on have stressed concentrated vortical flow features not encountered as much with the earlier designs. Earlier history of the slender wing development and vortex flow aerodynamics has been given by Küchemann [14].

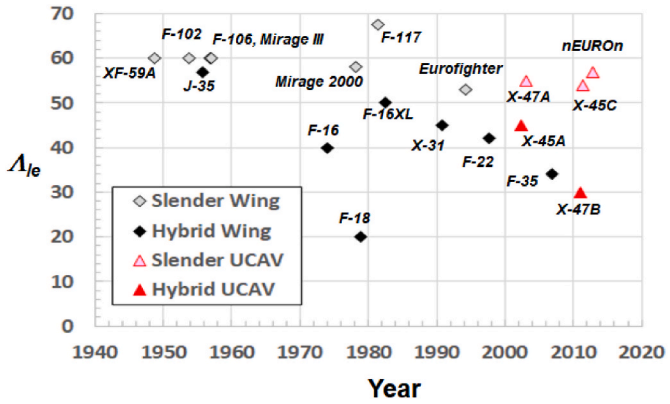

Fig. 8. Leading-edge sweep values, combat aircraft.

2.2.2. Commercial interests

During the 1940s all aircraft manufacturers were eager to exploit fully the performance potential of the jet engine by sweeping the wing in their design concepts. The first such military configurations to fly were the North American F-86 and the Boeing XB-47, both in late 1947 (Loftin [15]). The B-47 emerged as the world's first large multi-engine swept--wing airplane – a design configuration that became the standard for all modern jetliners, beginning with the B-707 as explained by Cook [16]. In addition to its 35° swept wings, the B-47 featured pod-mounted engines and "bicycle" landing gear. A photograph of the B-47 is shown in Fig. 9.

Sweeping the wing, however, had unwanted repercussions on performance and flying qualities. At a given angle of attack, a swept wing generates less lift than a straight wing, necessitating higher incidence for landing and higher stall speeds. Sweep also changes the spanwise distribution of induced flow angle such as to load the outboard wing section more heavily. Flow separation and consequent loss in lift over the outboard sections then would necessarily precede that over the inboard sections. The induced angle-of-attack distribution and the characteristic boundary-layer growth on such wings promote tip stall (Furlong and McHugh [17]). Both the tip-stalling tendencies and low values of attainable lift of swept wings constituted takeoff and landing problems requiring considerable mitigation at low speeds.

In an early summary of the longitudinal stability characteristics of swept wings, Weil and Gray [18] established a relation between wing planform parameters and the type of longitudinal stability that existed at or prior to maximum lift. Their correlation showed that longitudinal instability due to tip stalling was dependent primarily on aspect ratio and sweep angle, and they established an empirical variation of aspect ratio with sweep angle that defined a stability boundary shown in Fig. 10.

At transonic speeds, the appearance of a shock wave on the outboard section of the wing causes the boundary layer to separate. For example, wind tunnel tests had shown the XB-47 would pitch up at maximum speed due to wing stall. Thus, some form of separation management was required at both low and high speeds for the B-47.

Control of boundary-layer separation and of vortex flow is an important aerodynamic design tool; an aircraft today is unthinkable without such control. The benefits of separation control and vortex control include reduced drag, increased lift, improved stability, and overall enhanced performance. Separation control can be a direct design means or a "repair" solution, after wind tunnel or flight tests have shown a need for correction. Concentrated vortex flows can be used to mitigate an undesirable flow separation through a controlled separation. Vortex generators and strakes are two such significant control means.

2.2.2.1. Vortex generators. Vortex Generators (VGs) are applied to many aircraft as small passive flow control devices that delay flow separation and wing stall to reduce stall speed, increase maximum lift coefficient $C_{L,max}$, and improve control surface effectiveness. (See the review by Lin [19], 2002, and the doctoral dissertation by Jirásek [20], 2006.) They generate a concentrated longitudinal vortex near the boundary-layer edge that persists downstream to resolve the undesired flow features, often reducing or even preventing a downstream separation.

Discovered by two United Aircraft engineers in 1947, Brynes and Taylor [21] used vortex generators to cure a flow separation problem in the diffuser of a wind tunnel in East Hartford, Connecticut. At that time, Boeing was developing the XB-47 and had recently changed the design to incorporate a new concept, the swept wing. Early designs with the swept wing indicated an unacceptable shock-boundary-layer interaction leading to separated flow. Knowledge of vortex generators had spread to Boeing, and they were used to resolve the shock-induced separation issue (Ganzer [22], 1947). This was the first application of vortex generators to a swept wing for what became a production aircraft, the B-47. Fig. 11 from Cook [16] shows how the Boeing engineers applied VGs to the XB-47 to effectively delay flow separation.

Vortex generators differ in size and shape and can be denoted by different names, but their fundamental fluid dynamic mechanism is the same. The longitudinal vortices transport high momentum flow from the outer domain of the boundary layer into the near-wall domain of the boundary layer. In this way, the momentum of the near-wall boundary-layer flow is enhanced and its proneness to separation is reduced. Vortex generators are commonly used on the wings of transonic aircraft to avoid large areas of shock-induced boundary-layer separation as well as

Fig. 9. Swept wing. B-47, first flight in December 1947. [Photo: Wikipedia, reprinted under Creative Commons License].

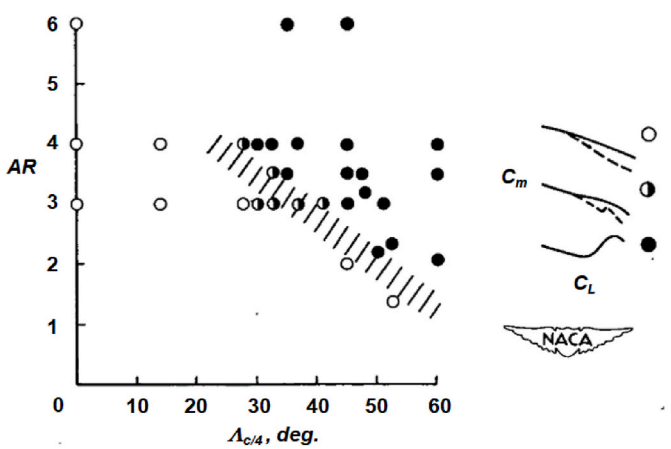

Fig. 10. Aspect ratio-sweep stability diagram. $0.8 < M < 0.95$, $0.03 < t/c < 0.06$, $0 < \lambda < 0.7$. Weil and Gray [18], 1953.

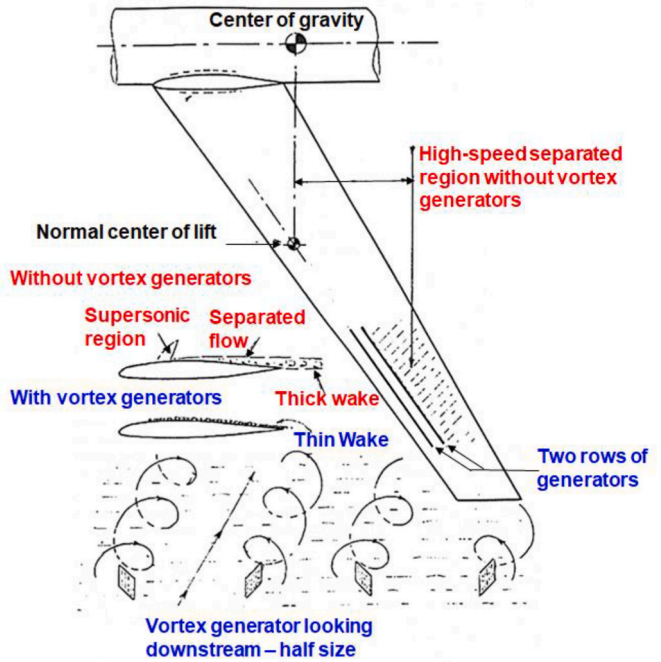

Fig. 11. Transonic pitch-up on B-47 cured by vortex generators. Cook [16], 1991.

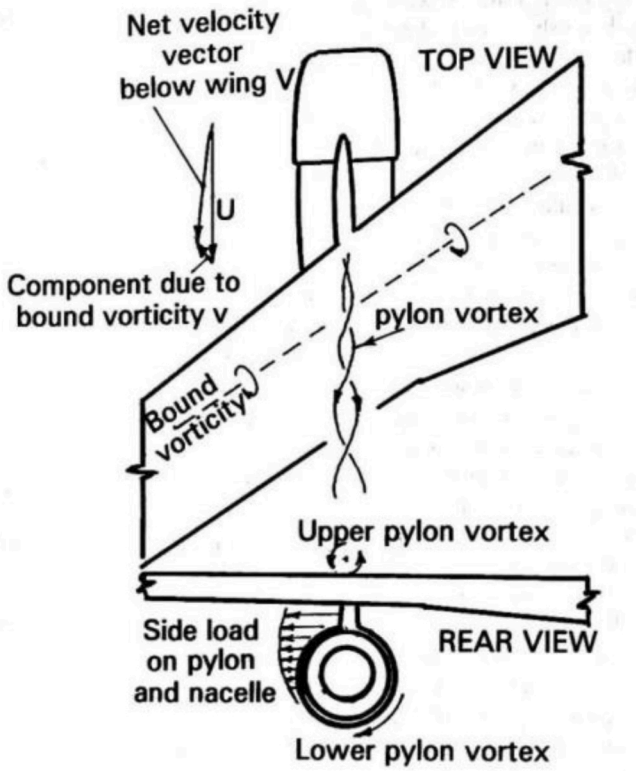

Fig. 12. Pylon-shed vortex for separated flow management. Abzug and Larrabee [26], 1997.

to relieve buffet and pitch up (Pearcey [23], ESDU [24]). Separation management with vortex generators applies to low-speed interests as well. More recently, micro vortex generators (μVGs, also known as sub-boundary-layer vortex generators) have been developed. These are fully submerged in the boundary layer but the momentum transfer via a concentrated vortex flow remains the mechanism. As an industry demonstrator of the possible benefits, Bohannon [25] adapted an array of μVGs in 2006 to an A340-300 test aircraft where flight tests showed that, by reducing flap separation, it allowed a larger flap angle that increased lift in landing by approximately 2.5% across the incidence range. In 2006 Lin [19] reviewed the μVG technology. The status of CFD predictions for concentrated vortex flows from vortex generators can be found in Subsection 3.2.1.

2.2.2.2. Pylon vortices and vortilons. In addition to establishing the swept wing, the B-47 also established the podded engine and nacelle pylon as the configuration for high-speed jet-powered transports. The swept wing introduced new challenges for separated flow management, and it was found that the pylon could be another source for using a concentrated vortex to manage the swept-wing flow.

At low speed, the swept wing of the XB-47 experienced stalling characteristics with severe pitching and rolling moments due to outboard wing separation. Wing-tip stalling could also cause the loss of aileron control and rolling in the stall. Cook [16] writes that the mitigation Boeing applied was selective placement of the engine pods together with drooping of the wing leading edge. At high angles of attack, the pylons supporting the pods caused the boundary layer on the upper surface of the wing to peel off and form a longitudinal concentrated vortex that trailed chordwise at the pylon-wing juncture, Fig. 12. The pylon vortices mitigate the spanwise wing flow at elevated loading conditions with a net effect that stall would start further inboard and near the wing center of lift. As a result, the aircraft pitch up was eliminated at stall conditions. At low angle of attack cruise conditions, the pylon vortex was absent and thus did not interfere with cruise design considerations. Boeing used this same mitigation on its first commercial airliner, the B-707. Other aircraft designs (e.g., the French Caravelle) explored the use of streamwise physical fences to manage the swept wing spanwise flow, and, in this regard, the pylon vortex could be considered a fluid fence.

In the early 1960s, the McDonnell Douglas Aircraft Corporation was developing the DC-9 with aft-fuselage-mounted nacelle/pylon/engines. Spanwise flow on the swept wing still was conducive to pitch up issues, and aerodynamicists working on this design invented and patented the vortilon[4] [27]. Vortilons are truncated pylons (no nacelle) that generate the pylon vortex just described. They can be positioned solely for the purpose of separation management and were used to address wing stall properties including pitch up. The vortilons were also beneficial to wing lift and upwash at the tail at the low-speed stall conditions. More recent aircraft employing vortilons are the McDonnell Douglas MD-90, the Boeing 717 and the Embraer ERJ 145 family of regional jets, Fig. 13.

2.2.2.3. Nacelle strakes. The advent of high-bypass-ratio engines presented a new separated flow challenge for transport aircraft. At takeoff and landing conditions, smooth-surface separation from the enlarged nacelles could induce a local wing stall aft of the nacelle with unacceptable losses in lift. This deficiency was resolved by developing the nacelle strake.

A strake is an aerodynamic surface that generates a concentrated vortex to improve aircraft flight characteristics with controlled separation, either by direct vortex lift effects (e.g., Fig. 2(a), F-16) or by induced effects through vortex persistence (e.g., Fig. 2(b), A340). Strakes are larger than vortex generators, interacting with the local inviscid flow.

Nacelle strakes were patented by Kerker and Wells in association with the McDonnell Douglas Aircraft Corporation in 1973 [28] and used for the first time on the DC-10 (first flight in August 1970). Persistence of the nacelle strake vortices over the wing resolved the local wing stall and provided a solution to avoid a significant lift loss at high lift conditions

[4] Vortilon is an abbreviation for VORTex generating pYLON.

Fig. 13. Vortilons on an ERJ-175. [Photo: Stackexchange, reprinted under Creative Commons License].

(see Shevell [29], 1986). Nacelle strakes can lower stall speed in approach configuration and reduce the required takeoff and landing runway length. In the case of the DC-10 aircraft, this reduction was about 6 percent. Nacelle strakes have become commonly adopted, and an example of a nacelle strake is shown in Fig. 14 for a Boeing 737–400 aircraft.

Older airframes have been retrofitted for high-bypass-ration engines, and nacelle strakes have been included in this design upgrade. Fig. 15 shows a Boeing 707–700 retro-fitted with high-bypass-ratio engines and illustrates the nacelle strake concentrated vortices persisting over the wing configured for high lift through natural condensation effects. These vortices can persist to the wing trailing edge and will be a critical feature for CFD to simulate accurately for commercial transport high lift interests. Nacelle strake vortices have superseded the pylon vortices discussed in the previous section. The status of CFD predictions for concentrated vortex flows from nacelle strakes can be found in Subsection 3.2.2.

2.2.2.4. Supersonic transports. Research and development in the 1960s led to the first supersonic commercial transport, Concorde (Fig. 16). The Concorde used a thin ogee wing to enable efficient supersonic cruise (supercruise up to $M = 2.04$) and to develop high lift from separation-induced leading-edge vortices at takeoff and landing conditions. The concentrated vortices were crucial to achieving the necessary low-speed high-lift increments and prevented the need for mechanical high-lift systems. Research leading to the development of this design concept is included in Küchemann [31].

Supersonic operation of the Concorde was restricted to over-sea

Fig. 14. High-bypass-ratio engine with nacelle strake. Boeing 737–400. [Photo: Stackexchange, reprinted under Creative Commons License].

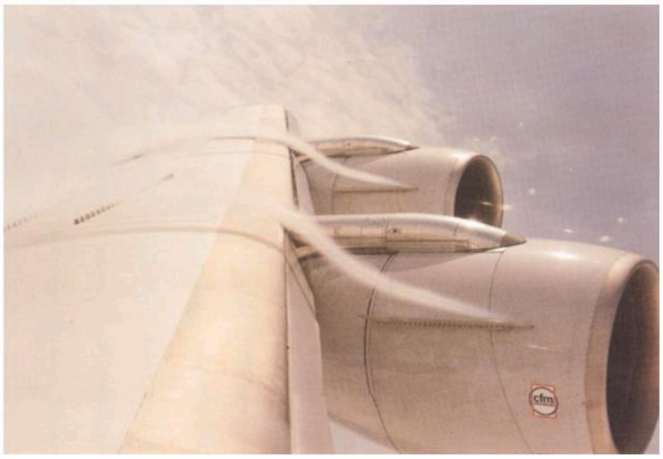

Fig. 15. Nacelle strakes on the Boeing 707–700. Campbell and Chambers [30], 1994.

Fig. 16. Ogee wing. Concorde, first flight in March 1969. [Photo: Stackexchange, reprinted under Creative Commons License].

conditions due to its sonic boom, and the lack of sanctioned supersonic over-land operations contributed to financial challenges for the aircraft. A research program at NASA has led to a low-sonic-boom concept that could enable over-land supersonic flight if successful. An X-plane program is underway at the time of this writing to fabricate and fly the X-59 low-boom demonstrator in collaboration with Lockheed-Martin, Fig. 17. Initiation of the flight-test research program is anticipated for 2024. The X-59 incorporates a highly swept ogee wing and is designed to operate up to moderate angles of attack. It is anticipated that the ogee wing will still have some leading-edge vortex flows at takeoff and landing conditions. The vehicle also has canards that could lead to vortex interactions with the wing flow. To the extent the flight test program is successful the X-59 could lead to a new generation of supersonic transports, somewhat reminiscent of how the XF-92A X-plane program led to a new generation of military combat aircraft such as the F-102A (see Luckring [1]).

2.2.3. Summary comments

Concentrated vortex flows are exploited over a wide range of scales for enhanced performance of both military and civil aircraft. Here we introduce a hierarchical perspective that merges these scales for concentrated vortex flow physics with conventional systems engineering levels (e.g., systems, subsystems, components, subcomponens) as shown in Fig. 18. Aerodynamic performance metrics are established at the configuration level and are addressed with concentrated vortex flows from the airframe system, and often with the lifting surface subsystem. For example, the slender wings that are required for efficient supersonic

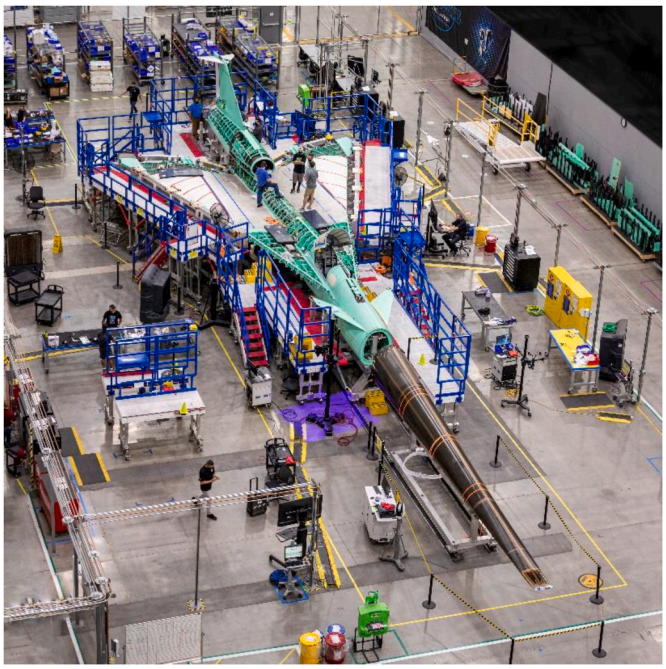

Fig. 17. Slender wing. NASA/Lockheed-Martin X-59, first flight projected for 2024. [Photo: NASA, public domain].

flight are conducive to generating system-scale concentrated vortex flows that are useful for takeoff and landing high-lift increments. Maneuver lift increments can be realized from lifting surface subsystems such as the hybrid wing concept using vortex-lift strake component in conjunction with an attached-flow wing component. Strakes are also used as a component on high bypass-ration propulsion systems to enhance takeoff and landing lift trough vortex persistence effects. Subcomponents, such as VGs, generate concentrated vortex flows either at the edge of a wing boundary layer or even within the boundary as is the case with μVGs (see Lin [19]). In both cases, vortex persistence is exploited to ameliorate adverse separation effects downstream on the lifting element.

At subcomponent system scales, the concentrated vortices are on the order of boundary layer scales and the physics often include vortex interactions with boundary layers. These concentrated vortices are generally used for flow control. At component system scales, the concentrated vortices are on the order of a component characteristic length, and the physics often include vortex interactions with surrounding inviscid flow. These concentrated vortices are used either for flow control or for lift enhancement. At subsystem scales, the concentrated vortices are on the order of a subsystem characteristic length, and the physics generally include vortex interactions with surrounding inviscid flow. These concentrated vortices are used primarily for lift enhancement. Performance increments from the concentrated vortex flows are assessed for the airframe system as well as for the integrated configuration. In the next section the elemental flow physics of concentrated vortex flows are reviewed.

2.3. *Elemental flow physics of concentrated vortex flows*

In this section, the flow physics of a concentrated vortex flow are presented from two perspectives. First, the elemental components of a concentrated vortex flow are reviewed, Subsection 2.3.1. This is followed by a presentation of concentrated vortex flow physics manifestations, Subsection 2.3.2.

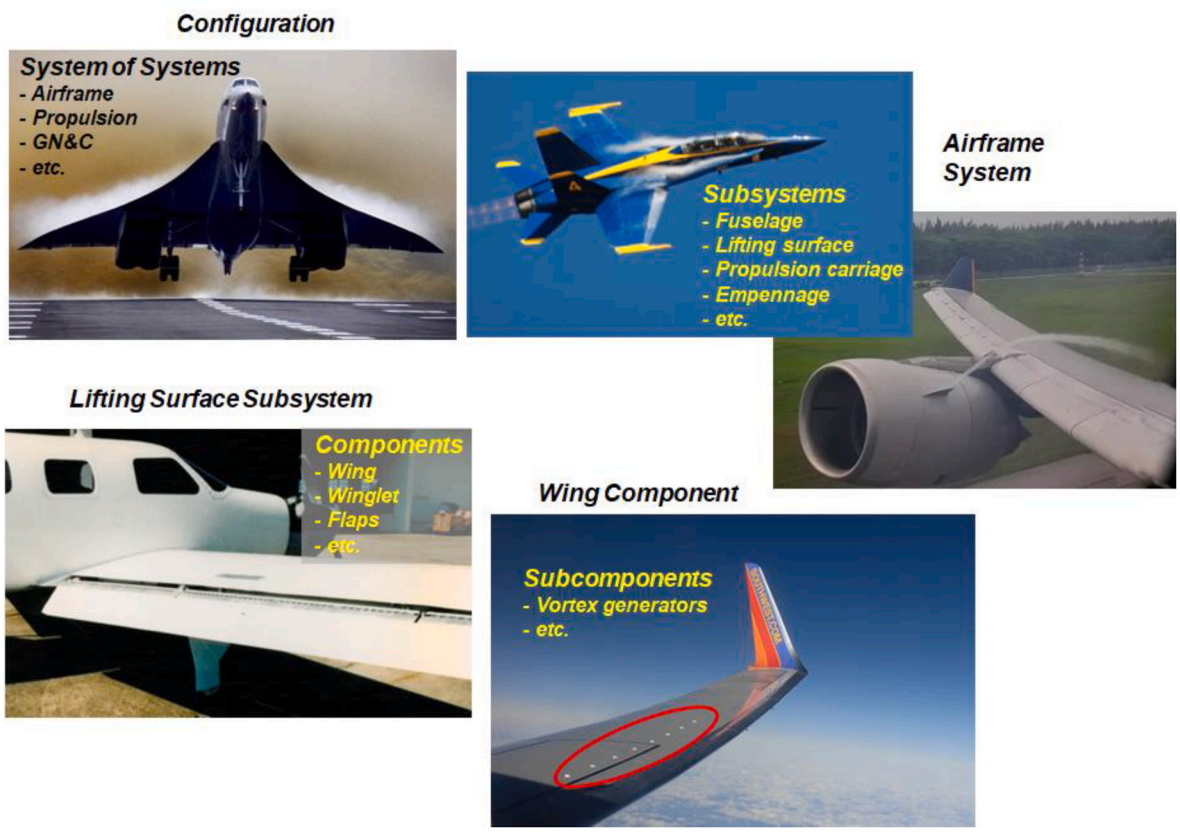

Fig. 18. Concentrated vortex flow applications span multiple system scales. [Photos: Concorde: Reuters, reprinted under Reuters Institute License; F-18: shinforce.com, reprinted under Content Agreement License; A340: C. Frank Starmer, reprinted under Creative Commons License; Piper Malibu: NASA, public domain; 737: copyright photovault.com Inc., reprinted under license].

2.3.1. Flow physics components

Here we review the fundamental flow physics components of concentrated vortex flows. These elemental components constitute the basic physics of a concentrated vortex flow which, although always present, are stressed differently based upon the intended use of the vortex. The review first addresses sharp-edge separation (Subsection 2.3.1.1) followed by treatment of the additional vortex flow physics that arise for smooth surface separation (Subsection 2.3.1.2).

2.3.1.1. Sharp-edge separation. Here we introduce the basic components of a separation-induced concentrated vortex flow from sharp leading and trailing edges. These basic components are discussed in terms of slender delta wing, and include the primary vortex shear layer, the primary vortex core, and the trailing-edge shear-layer rollup in association with a concentrated vortex flow. Secondary vortices are discussed in the following Subsection 2.3.1.2 on smooth-surface separation.

Sharp leading-edge separation: For the sharp-edged and highly-swept delta wing, the flow undergoes a primary separation at the wing leading edge in the form of a highly-swept free shear layer, also known as a vortex sheet. The vortex sheet rolls up upon itself to form a vortex core, and collectively this constitutes the separation-induced primary leading-edge vortex. A sketch of this flow is shown in Fig. 19. The primary vortex induces reattached flow on the wing upper surface that includes high-speed spanwise flow under the vortex. This high-speed flow is the source for much of the vortex lift associated with separation-induced vortex flows on slender wings at moderate to high angles of attack. The primary vortex can remain stable over these conditions, and its properties depend on wing geometric details as well as angle of attack and Mach number; Reynolds number is less influential.

A more detailed view for the structure of a concentrated leading-edge vortex is shown in Fig. 20 from Nelson and Pelletier [33]. The thickness of the leading-edge vortex sheet grows with distance along the spiral trajectories shown in Fig. 19. The vortex sheet can also exhibit stable sub-scale vortical structures in association with the Kelvin-Helmholtz shear-layer instability process. Both attributes will vary with Reynolds number. As the vortex sheet rolls up upon itself, it feeds vorticity into the vortex core such that two regions occur. The outer region of the vortex core is dominated by inviscid but rotational flow physics. This flow would be governed by the Euler equations. The inner region is dominated by viscous flow physics and is referred to as the viscous subcore. The demarcation between the inviscid rotational outer core flow and the inner viscous subcore flow depends upon Reynolds number.

Theoretical modelling of the vortex core flow has been performed by Hall [34] in 1961 for the inviscid rotational vortex core flow physics and by Stewartson & Hall [35] in 1963 to include the viscous subcore flow physics using matched asymptotic expansions. Conical flow assumptions were used, and an example of the vortex core flow from this modelling is shown in Fig. 21 from Luckring [1]. Axial and circumferential velocities are shown as a function of an inner-law scaled radial variable. The outer inviscid but rotational flow is singular at the vortex core axis while the

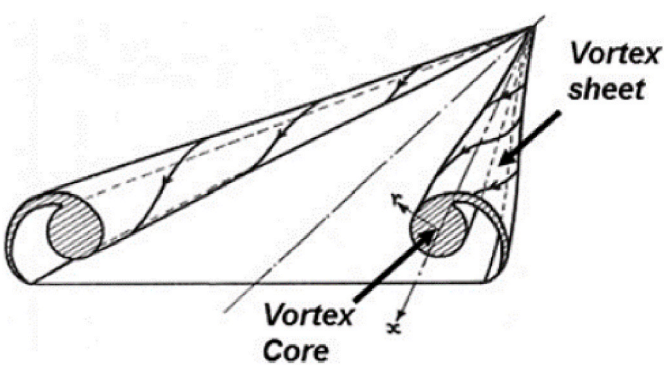

Fig. 19. Leading-edge vortex sheet and vortex core. Hall [32], 1959.

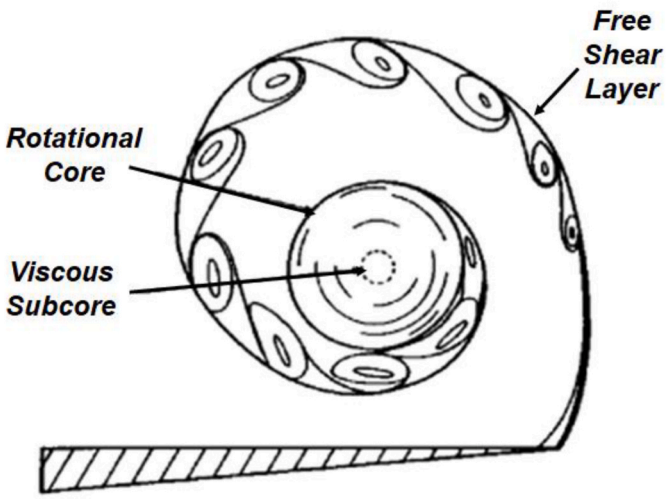

Fig. 20. Three regions within a leading-edge vortex. Nelson and Pelletier [33], 2003.

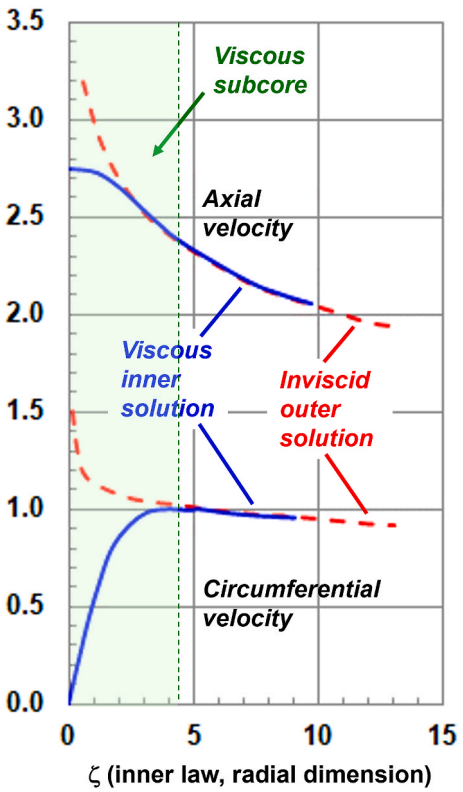

Fig. 21. Theoretical vortex core velocities. Luckring [1], 2019.

viscous inner flow removes this singularity and asymptotically matches the outer solution. Departure of the viscous flow solution from the inviscid rotational solution established the boundary of the viscous subcore for this modelling. Velocities are normalized by the freestream velocity, and we note that the circumferential velocity is on the order of freestream velocity while the axial flow approaches three times the freestream value. Compressible flow physics can be anticipated within the core of a concentrated vortex flow, and this effect was studied by Brown [36]. Use of the inner-law variable in Fig. 21 enables display of the viscous vortex core properties. The physical scale of the viscous subcore can be quite small and decreases with Reynolds number.

A flow-visualization image is shown in Fig. 22 from Nelson and

Pellitier [33] that illustrates a number of these concentrated vortex flow features. Shear-layer instabilities can be seen at the third and subsequent chordwise stations. These instabilities are steady; they take the form of helical subvortices within the vortex sheet. The dark region in the center of the vortices contains the vortex core but does not necessarily indicate the edge of the core. Flow visualization particles will depart from streamline trajectories due to centrifugal and pressure gradient effects in association with the high circumferential velocities within concentrated vortices. This feature was addressed by Greenwell [38] in 2003.

Sharp trailing-edge separation: The presence of a concentrated leading-edge vortex flow alters the structure of the wing trailing wake. For a fully attached flow, the spanload diminishes continuously from root to tip and this results in the familiar rollup of the trailing-edge wake into two counterrotating wake vortices. The presence of a concentrated leading-edge vortex flow introduces an inflection to the spanload distribution on a slender wing, and consequently a counterrotating vortex forms in the wing wake inboard of the wing semispan. A sketch of the wake flowfield is shown in Fig. 23 from Le Moigne [37], and detailed wake measurements are shown in Fig. 24 from Hummel [4]. As the flow develops in the downstream direction, the trailing-edge wake vortex will affect the position and eventually the strength of the wing primary leading-edge vortex as the two vortices interact and eventually merge. The trailing-edge wake vortex is small as compared to the wing leading-edge vortex, but the interaction effects could be important for applications of concentrated vortex flows where vortex persistence is of interest (e.g., the nacelle strake vortex as shown in Fig. 2(b) and is discussed in Subsection 2.2.2.3).

2.3.1.2. Smooth surface separation. Smooth-surface separation introduces additional flow physics to separation-induced concentrated vortex flows. The wing primary vortex, as discussed in the preceding section, always induces a secondary vortex flow, and the secondary vortex occurs from a smooth-surface separation even if the wing leading edge is sharp. Moreover, smooth-surface separation from a blunt leading-edge fundamentally alters the concentrated vortex flows on slender wings. With the blunt leading edge, the origin of the vortex is displaced from the apex of the wing, Fig. 25, and several new physical phenomena occur. The primary leading-edge vortex still induces a secondary vortex, but a new region of incipient leading-edge separation occurs upstream of the vortex separation. In addition, a new *inner* vortex forms from the region of the primary vortex origin and persists downstream over the wing. Neither of these occur for the sharp-leading-edged wing. Finally, we observe that there is a region of attached flow from the

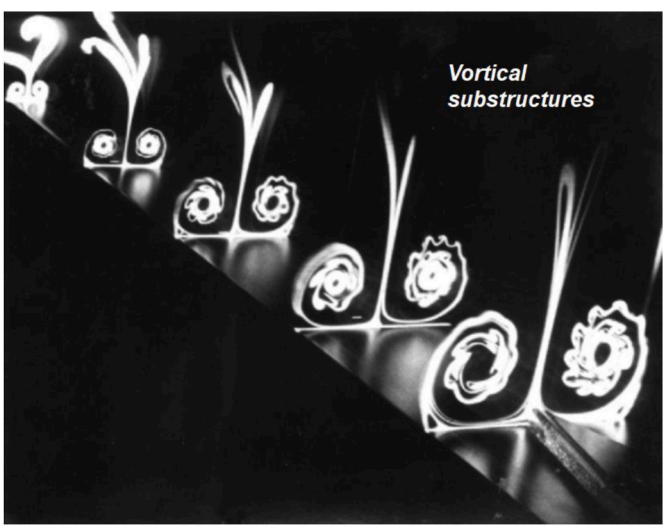

Fig. 22. Vortical substructures. $\Lambda = 85°$, $M \sim 0$, $Re_{cr} = 85 \times 10^3$, $\alpha = 20°$. Nelson and Pelletier [33], 2003.

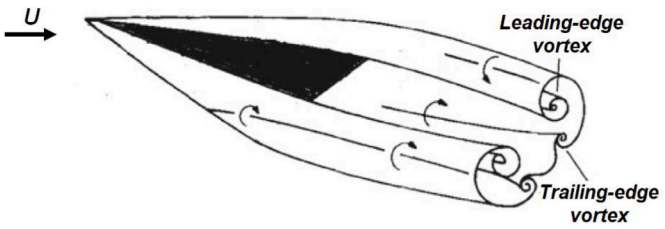

Fig. 23. Trailing-edge vortex sketch. Le Moigne [37], 2004.

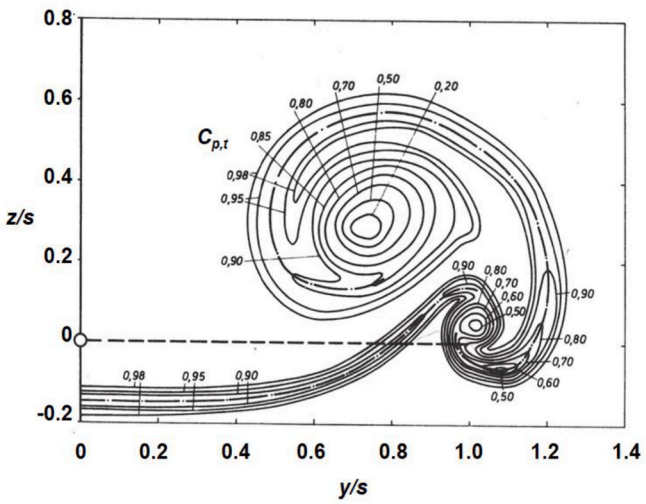

Fig. 24. Leading-edge vortex effect on trailing-edge wake, $\Delta x/s = 0.533$. $AR = 1$, $M \sim 0.1$, $Re_{cr} = 2 \times 10^6$, $\alpha = 20.5°$. Hummel [4], 1978.

upstream blunt leading edge that persists downstream over the wing. Smooth-surface vortical separation presents a challenge for modelling and simulation since the phenomena occur simultaneously and stress different flow physics. Each of the four smooth-surface vortical separation features are described in the following subsections.

Secondary separation: Spanwise reattached flow under the primary vortex experiences a favorable followed by an adverse pressure gradient as it passes under the leading-edge vortex. The adverse pressure gradient separates the spanwise boundary layer flow from the smooth wing upper surface, and this separated flow rolls up into a counterrotating secondary vortex. A sketch from Hummel [4] of this secondary vortex

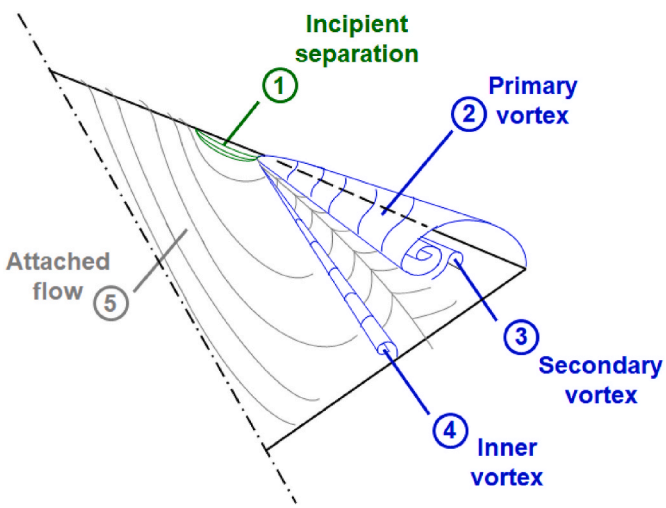

Fig. 25. Blunt-leading-edge vortex separation.

separation for a sharp-edge delta wing is shown in Fig. 26. Although the secondary vortex is small, it can exert significant effects on the primary vortex due to its proximity to the primary vortex sheet and primary vortex core. Hummel demonstrated experimentally [4] that details of the secondary vortex separation can significantly alter the primary vortex strength and location. The two vortices constitute a closely coupled vortex system. Detailed surface oilflow patterns have also shown tertiary vortices in some cases.

Blunt-leading-edge separation: Some fundamental flow physics for blunt-leading-edge vortex separation vortices were described by Luckring [39] in 2004 based on an experimental investigation for a 65° delta wing with blunt leading edges in the NASA Langley National Transonic Facility (NTF). (See, Chu and Luckring [40].) A sketch from Luckring [39] contrasting sharp and blunt leading-edge vortex separation for delta wings is shown in Fig. 27. The left semispan of the delta wing shows the sharp-leading-edge case with the origin of the vortex at the apex of the delta wing and vortex separation fixed at the sharp leading edge. The right semispan shows the blunt-leading-edge case where the origin of the vortex is displaced from the apex of the delta wing. This vortex origin varies with angle of attack, Mach number, Reynolds number, and leading-edge bluntness among other effects (camber, surface roughness, etc.). In addition, the vortex separation will now occur near, but not necessarily at, the leading edge.

Some general findings from Luckring's analysis are summarized as follows:

- An increase in angle of attack *promotes* leading-edge vortex separation;
- An increase in leading-edge bluntness *delays* leading-edge vortex separation;
- An increase in Mach number *promotes* leading-edge vortex separation;
- An increase in Reynolds number *delays* leading-edge vortex separation.

For example, at low angles of attack the wing could exhibit fully attached flow and, as angle of attack is increased, leading-edge separation will first occur near the wing tip and then progress upstream along the leading edge in association with leading-edge upwash and crossflow bluntness effects. Increased leading-edge bluntness will lessen adverse pressure gradients while increased Mach number can introduce local compressibility effects at the leading edge. Increased Reynolds number generally delays separation, and all these effects influence the attached boundary layer flow about the highly curved leading edge. The physics of this flow are quite different from the sharp-edged case. The blunt leading edge also introduces two additional flow structures that are not present for the sharp-edged case. These new structures were found in two recent North Atlantic Treaty Organization (NATO) Applied Vehicle Technology (AVT) research task groups, and details of this research are included in the presentation of survey findings Subsection 3.1.1.2. Basic features are described in the following subsections.

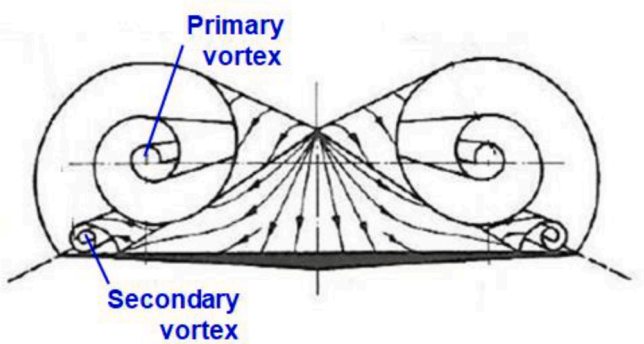

Fig. 26. Secondary vortex separation. Hummel [4], 1978.

Incipient separation region: An insipient separation region occurs near the leading edge and upstream of the blunt-leading-edge vortex separation. A dividing surface streamline separates the flow within this region near the leading edge from the attached flow inboard on the wing upper surface. Several characteristics of this region on the slender wing blunt leading edge resemble leading-edge bubble physics known from swept wing and airfoil aerodynamics. Additional understanding of the incipient separation region can be found from these airfoil and swept wing analyses.

Polhamus [41] summarized a succession of separation classes and a phenomenological notion of the physics which occur on blunt leading-edge airfoils and swept wings. His analysis included cases with blunt-leading-edge separation, and one example is shown in Fig. 28(a). At some angle of attack, a laminar separation bubble occurs near the leading edge of the airfoil and contracts with increasing angle of attack. With sufficient bubble contraction, the adverse leading-edge pressure gradient causes a turbulent reseparation of the boundary layer aft of the short bubble reattachment. This turbulent reseparation creates an expanding long bubble and an abrupt airfoil stall. The long bubble may eventually reach the trailing edge and no longer close. Visbal and Garmann [42] simulated a somewhat similar case with wall-resolved LES (WRLES) and found vortical features in their solution that are compatible with Polhamus' analysis.

Polhamus carried his analysis further to a swept constant-chord wing, Fig. 28(b). Spanwise loading increases toward the tip due, in part, to the spanwise increase of upwash at the leading edge associated with the vorticity of the swept-wing attached flow and wake. (See, for example, the Rizzi-Oppelstrup textbook [43].) Angle-of-attack trends discussed with the airfoil would correspond to spanwise variations of the flow at a fixed wing angle of attack. The spanwise pressure gradient along the leading edge sweeps the turbulent reseparation and introduces a swirl component to the expanding long bubble. Polhamus reasoned that, with sufficient wing sweep, these flows could lead to leading-edge vortex flows.

In a systematic wind tunnel campaign with constant-chord swept wings, Poll [44] investigated how blunt leading edge separation flow topology changed with (i) leading-edge radius and wing sweep as well as (ii) angle of attack and Reynolds number. Poll's swept wing results support the Polhamus analysis and is consistent with Luckring's delta wing findings. One highlight from his research is shown in Fig. 29 for a 56° swept wing with a leading-edge radius $r/c = 1.2\%$ measured normal to the leading edge. Flow conditions for Fig. 29(a) resulted in a full-span leading-edge vortex for the blunt-edged wing. A modest increase in Reynolds number from 1.4×10^6 to 2.7×10^6 (Fig. 29(b)) eliminated this leading-edge vortex separation in favor of an attached flow with a short-bubble separation near midspan. A 1° increase in angle of attack (Fig. 29(c)) shifted the short-bubble separation inboard and produced a part-span swirling flow, either as an expanding long bubble or a nascent leading-edge vortex flow, consistent with the Polhamus analysis above. By 16° angle of attack (Fig. 29(d)) the short bubble separation has moved further inboard, and a full-span leading-edge vortex has formed with the inner portion occurring after a short-bubble flow, perhaps in association with turbulent reseparation again.

Poll identified three mechanisms for the formation of spiral vortices, dependent upon the sweep angle, the leading-edge bluntness, and the Reynolds number:

(a) A full-span vortex can be formed by a rolling up of the shear layer which leaves the wing surface at the primary separation line. This type of vortex flow is very similar in appearance to the flows generated on sharp-edged thin delta wings at incidence.
(b) A part-span vortex can be formed when conditions are such that the shear layer from the primary separation reattaches to form a short bubble on the inboard portion of the wing but fails to reattach on the more heavily loaded outboard sections.

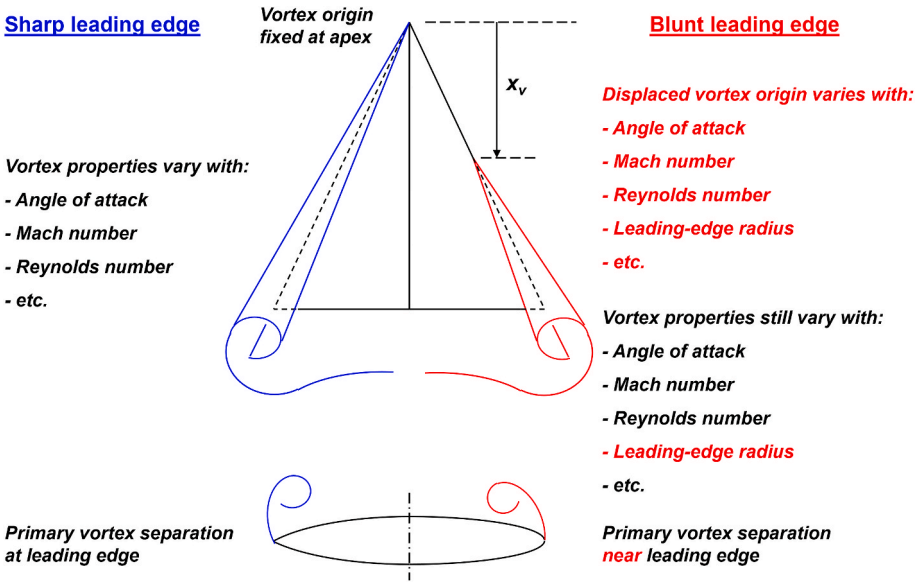

Fig. 27. Bluntness effect for-leading-edge vortex separation, delta wing. Luckring [1] 2019, [39] 2004.

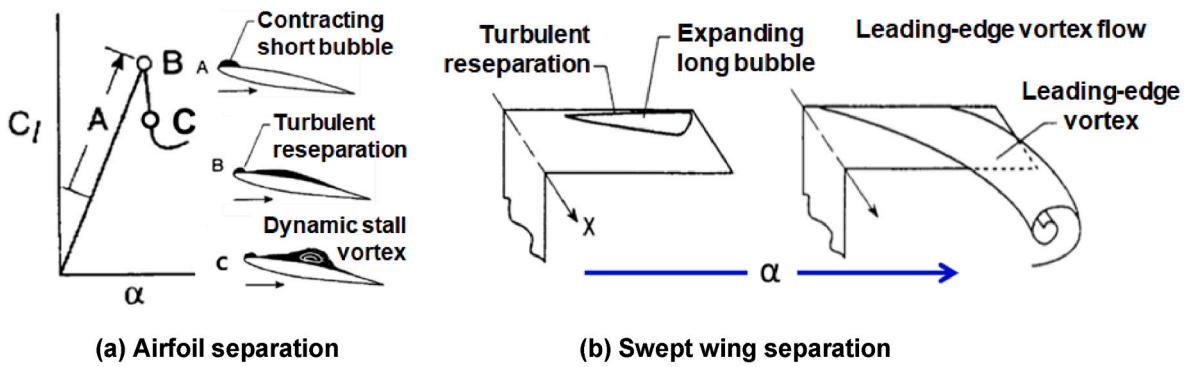

Fig. 28. Swept-wing/bubble physics. Polhamus [41], 1996.

(c) A part-span vortex can be formed when the boundary layer flow downstream of a short separation bubble leaves the surface close to the bubble along a line of turbulent reseparation in Polhamus' terminology.

The flow physics associated with these separation classes pose a challenge for accurate CFD simulation of the incipient separation leading to blunt-leading-edge concentrated vortex flows.

Inner vortex: An additional inner vortex forms on the wing upper surface in association with the blunt-leading-edge vortex separation. The origin of the vortex is near the origin of the primary vortex, and the inner vortex has the same rotation as the primary vortex. This inner vortex was part of the study in two recent AVT task groups and a first explanation of its existence was given by Hitzel et al. [45]. A simplified sketch based on their analysis is shown in Fig. 30. With a blunt leading edge, the upstream portion of the wing has attached flow and further downstream these streamlines will have an outboard component in association with the slender wing. The downstream portion of the wing has a blunt-leading-edge vortex, and this vortex will induce the usual reattachment line with outboard reattached flow outboard of the reattachment line and inboard reattached flow inboard of the reattachment line. The vortex-induced inboard reattached flow collides with the outboard attached flow resulting in the inner vortex. The inner vortex does not exist for the sharp-edged case because there is no upstream attached flow. The inner vortex can induce a small suction peak on the wing and requires additional grid resolution to capture. Further details of the inner vortex are included among the survey findings from a range of simulation formulations for both blunt leading-edge vortex separation (Subsection 3.1.1.2) and blunt side-edge vortex separation (Subsection 2.4.1.2).

Forebody flows: Most of the analysis in this report focuses on concentrated vortex flows in the context of aircraft lifting surface (wing) aerodynamics. However, many of the physics-based features discussed for wings are applicable to slender body interests such as arise for forebodies and missiles. One example from Keener [46] is shown in Fig. 31(a) for smooth-surface separation. In this analysis from his experimental studies, Keener shows concentrated vortex separation from a smooth forebody that includes laminar separation (LS), turbulent reattachment (R), laminar separation bubble (B), turbulent separation or reseparation (TS), transitional separation patterns (TRS), and secondary vortex separation (SS). Fig. 31(b) shows a sharp-edged forebody cross section with the sharp-edge primary vortex separation and the smooth-surface secondary vortex separation. The coupled vortex system is smaller (weaker) and displaced outboard by the forebody thickness as compared with a slender wing. Only limited missile results are included in this survey article, Subsection 3.2.3.5. Full treatment of forebody and slender body concentrated vortex flows would warrant a separate investigation.

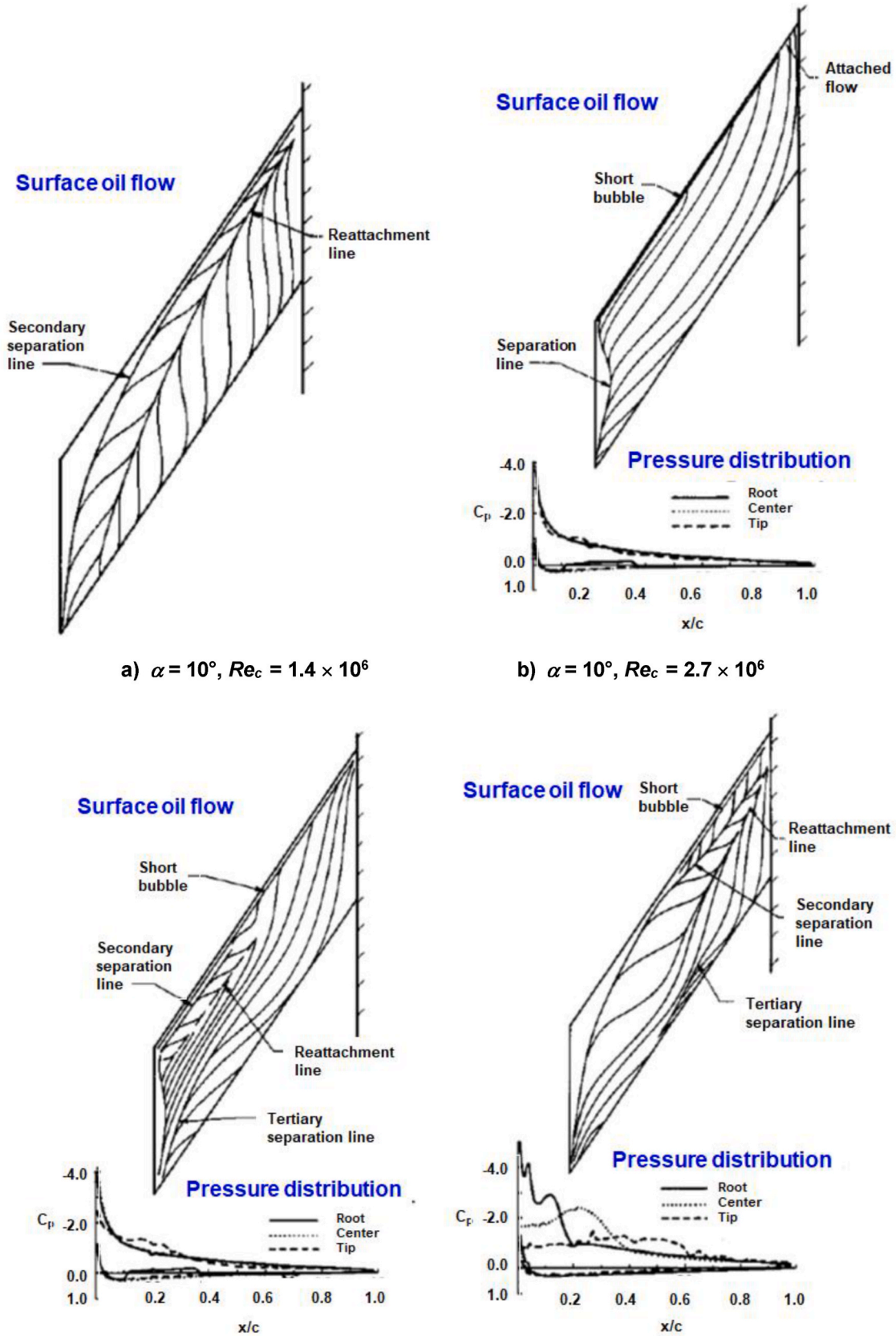

Fig. 29. Experimental surface oil flow patterns and pressure distributions. $AR = 2.68$, $\Lambda_{le} = 56°$, $r_{le}/c = 1.20\%$, $M = 0.1$. Poll [44], 1986.

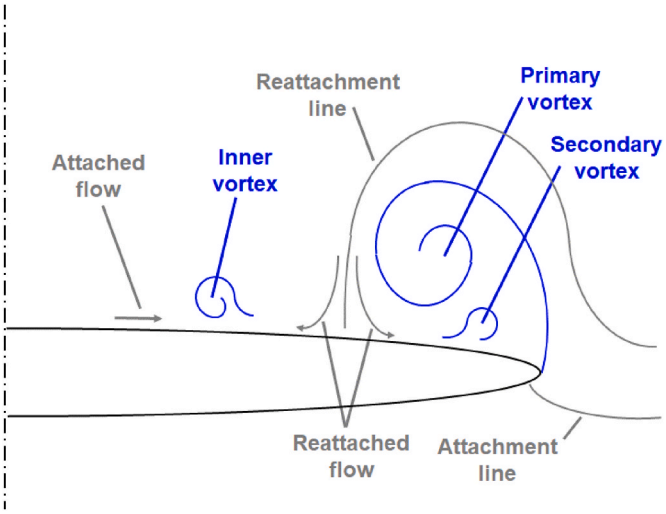

Fig. 30. Inner vortex.

2.3.2. Flow physics manifestation

The flow physics elements discussed in Subsection 2.3.1 can be, and often are, present for any concentrated vortex flow. However, the degree to which they occur can vary depending on the conditions associated with the concentrated vortex. Put another way, the physics can be modulated by the intended use of the concentrated vortex in association with configuration performance. New phenomena, such as vortex breakdown, can also arise. In this section we review these manifestations of concentrated vortex flows with a view toward the associated vortical flow physics. The review first addresses steady flows (Subsection 2.3.2.1) followed by unsteady flows (Subsection 2.3.2.2). For this article, flows for which the unsteadiness is no larger than typical turbulence scales are referred to as steady flows; flows for which the unsteadiness is larger than typical turbulence scales are referred to as unsteady flows.

2.3.2.1. Steady concentrated vortex flows. *Single vortex system:* A primary application of concentrated vortex flows is to generate vortex lift at high angle-of-attack maneuver conditions. An example of the vortex lift is shown in Fig. 32 for a unit-aspect-ratio delta wing. Spanwise pressure coefficient distributions from Hummel [4] are shown in Fig. 32(a) at several longitudinal stations from near the wing apex to the trailing edge. The suction peak near seventy percent local semispan results from the accelerated spanwise flow due to the primary leading-edge vortex. The adverse pressure gradient outboard of the suction peak results in secondary vortex separation. For turbulent secondary vortex separation, the outboard pressures are often flat as indicated in the figure. The concentrated leading-edge vortex pressure distributions result in a nonlinear vortex lift increment as shown in Fig. 32(b). The vortex lift has very little effect at low angles of attack, whereas it provides significant maneuver lift increments at high angles of attack. A theoretical estimate of the vortex lift from Polhamus [47] is included in the figure. Comparable accuracy from Polhamus' theoretical work based upon a leading-edge suction analogy has been shown over a range of flow conditions for simple wing shapes with concentrated vortex flows separated by sharp leading edges. (See, Luckring [1].)

A second application of concentrated vortex flows is to affect flow control through vortex persistence. This often takes the form of reducing or even eliminating a downstream adverse separation by virtue of an upstream controlled separation with the concentrated vortex. Examples of this application include vortex generators, as discussed in Subsection 2.2.2.1, and nacelle strakes, as discussed in Subsection 2.2.2.3 and shown in Fig. 2(b). Discussion of the present survey findings for these topics are in Subsection 3.2.1.

Vortex interactions: Vortex interactions can occur in several ways stressing different physics of the vortical flows. The concentrated vortex unit interactions (i.e., between two fluid entities) that arise on complex aircraft geometries have been decomposed into classes based upon the underlying physics of the vortex interaction. For this review we consider three classes of vortex interactions:

- Vortex-vortex interactions
- Vortex-shock interactions
- Vortex-surface interactions

Different fluid entities (e.g., shear layers, shocks, boundary layers) will be stressed differently among these three classes of vortex interactions. Each of these interaction classes will have different consequences as regards computational modelling effects and physical measurement interests.

Multiple vortices often form on a configuration from separate vehicle components or from geometric changes of a single component. An example of vortex-vortex interactions from a single component is shown in Fig. 33 for a double delta wing tested by Brennenstuhl and Hummel [48]. This example is for Wing VI from their studies with $\Lambda_{le} = 80°/60°$

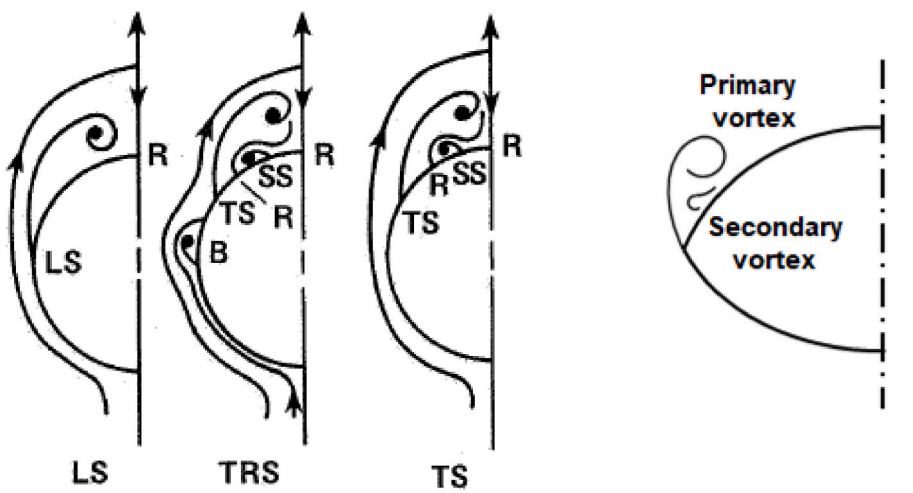

Fig. 31. Forebody concentrated vortex flows.

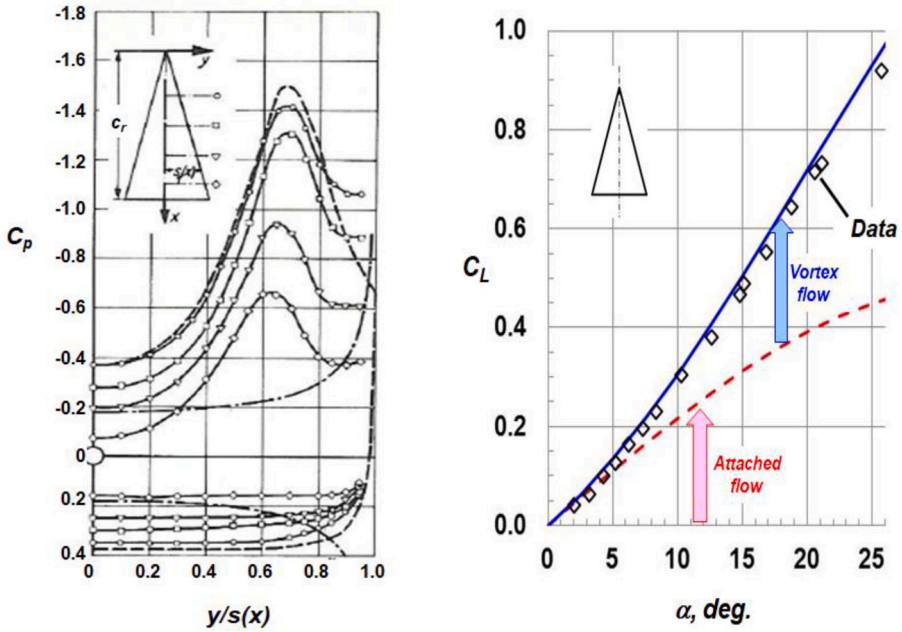

(a) Pressure distributions. Hummel [4], 1978. **(b) Vortex lift. Polhamus [47], 1966.**

Fig. 32. Concentrated leading-edge vortex effects. $AR = 1$ delta wing.

for the inboard/outboard wing portions, respectively. The abrupt change in leading-edge sweep results in both an inner and an outer vortex forming over the wing. The figure shows spanwise contours of the total pressure coefficient at two longitudinal stations and illustrates the inner and outer vortices. For this vortex-vortex interaction, the vortex shear layers have begun to merge, and the two stations show evidence of a convective merging process. At a lower angle of attack, the vortices can be unmerged, and at higher angles of attack, or greater distances downstream, they can undergo viscous merging. For the case shown, the vortices are coupled, and the coupling is manifested through a vortex shear layer interaction. The data also evidence a vortex-vortex interaction between the outboard primary and secondary vortices that results in an inflexion in the feeding shear layer of the outboard primary vortex. This interaction can be a source of shear-layer instabilities and is further discussed in Subsections 3.1.1.2 and 3.1.2.1.

At higher speeds concentrated vortex flows and shocks can form in proximity to one another thus leading to vortex-shock interactions. Two classes of vortex-shock interactions are considered. In the first case, formation of the vortex and the shock are mutually dependent and often occur on a single lifting surface. An example of this case is shown in Fig. 34 for a supersonic delta wing tested by Miller and Wood [49]. The observer is looking upstream, and the leading-edge vortices have induced several off-body shocks. Due to their relative orientations, this vortex-shock interaction can often result in the shock affecting the vortex circumferential flow more than the vortex axial flow. In the second case, the vortex and shock form independently but subsequently interact, such as for a close-coupled canard/wing configuration with the canard vortex encountering a downstream wing shock. Due to their relative orientations, this vortex-shock interaction can often result in the shock affecting the vortex axial flow more than the vortex circumferential flow.

Vortex surface interactions also categorize into two classes. In the first case, the vortex-surface interaction is confined to one lifting surface. The vortex interacts with its own lifting surface, and, as one example,

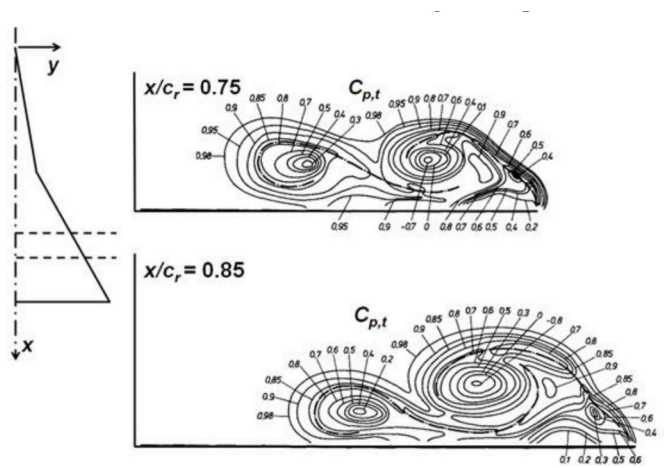

Fig. 33. Vortex-vortex interactions, double delta wing. $\Lambda_{le} = 80°/60°$, $M \sim 0.1$, $Re_c \sim 1.3 \times 10^6$, $\alpha = 12°$. Brennenstuhl and Hummel [48], 1982.

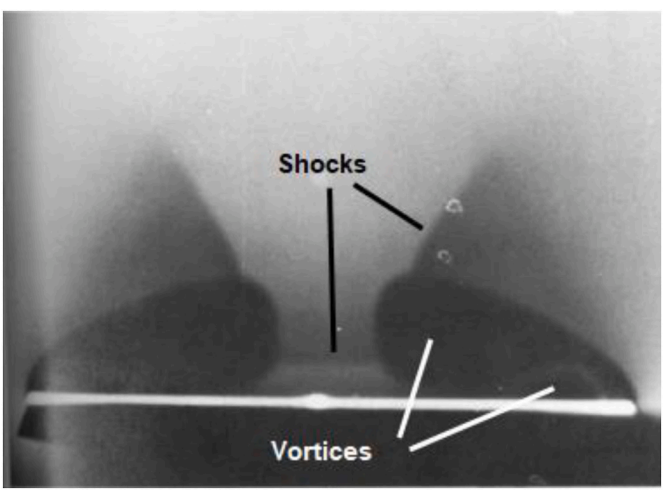

Fig. 34. Vortex-shock interactions, vortex-induced shocks. $\Lambda_{le} = 75°$, $M = 2.8$, $Re_{mac} = 2.5 \times 10^6$, $\alpha = 20°$. Miller and Wood [49] 1984.

the vortex circumferential flow induces a boundary-layer effect on its wing upper surface. An example, as discussed with Fig. 26, is for the formation of the secondary vortex. In the second case, the vortex-surface interaction occurs with multiple lifting surfaces. Examples of this vortex-surface interaction are often found on missiles where the concentrated vortex from an upstream control surface encounters the downstream missile fins. A second example is the interaction that occurs on transports between a nacelle strake vortex and the downstream wing. Vortex persistence is important for this second class of vortex-surface interaction.

Vortex tearing: Concentrated leading-edge vortices can tear from one to multiple vortices due to geometric discontinuities near the leading edge. One example was shown with Fig. 33. The abrupt change in leading-edge sweep changes the vorticity feeding into the vortex shear layer such that the sheet tears and two vortices form on the double-delta wing. Subtler geometric effects can also cause vortex tearing, and an example is shown in Fig. 35 from the Vortex Flap Flight Experiment (VFFE) [50]. In this work, an F–106B aircraft was configured to assess a leading-edge vortex-flap designed to capture the leading-edge vortex on the flap upper surface. The flap was fabricated in segments and the segment gaps were covered with thin strips to eliminate gap flow between the segments. The small discontinuity from the strip thickness resulted in vortex tearing and the succession of concentrated vortices shown in Fig. 35. Subsequent wind tunnel testing by Hallissy et al. [51] confirmed this feature.

Fluid mechanics can also result in vortex tearing. Gap flow between flap segments is another source of vortex tearing, and an example of this is included in the survey findings Subsection 3.2.3.4 for an X-31 configuration. Secondary vortices can disrupt the vortex feeding sheet of the parent primary vortex and contribute to vortex tearing. This interaction was just discussed with Fig. 33.

2.3.2.2. Unsteady concentrated vortex flows. In general, there will be a cascade of scales over which unsteady vortical flow physics will be manifested, and here we distinguish two classes of unsteady concentrated vortex flows. The first arises within the vortex physics itself for otherwise steady boundary conditions, i.e., the unsteadiness arises within the vortical fluid mechanics. The second arises due to unsteady boundary conditions, such as for a pitching wing. In this instance, unsteadiness is imposed upon the vortex flow. For both classes, additional phenomena arise in association with the unsteady flows, and several of these are highlighted in this section. Additional discussion of unsteady leading-edge vortex flows has been given by Breitsamter [52] in 2008.

Steady boundary conditions, unsteady vortex flow: Here we consider unsteadiness on a scale larger than turbulence that can arise within and due to concentrated vortices under otherwise steady conditions. Unsteadiness can occur locally, within an otherwise steady vortical flow, or globally, i.e., on the scale of the entire concentrated vortex. Several examples follow.

Fig. 35. Vortex tearing, F–106B VFFE. $M \sim 0.3$, $Re_{cref} \sim 40 \times 10^6$, $\alpha = 10°$, $\delta_f = 40°$. Brandon et al. [50], 2003.

The first example is the vortex breakdown phenomenon. One well-known example was documented experimentally in 1962 by Lambourne and Bryer [53] at low speeds for a 65° delta wing with sharp leading edges, Fig. 36(a). The bursting corresponds to an abrupt deceleration of the axial flow in the core of the vortex resulting in locally reversed and fluctuating flow. Upstream of the vortex breakdown location the vortex remains steady, whereas downstream of vortex breakdown the vortex is unsteady. The photograph shows two modes of vortex breakdown, spiral and bubble, that occurred simultaneously in the Lambourne and Bryer experiment. The breakdown structure is locally unsteady and can either be stationary in space or oscillate longitudinally, either in phase or out of phase between the two semi-spans. Vortex breakdown first occurs near the trailing edge and moves upstream with increasing angle of attack (Wentz and Kohlman [55]). This can contribute to adverse pitch up and, for asymmetric breakdown, adverse rolling moment effects. The onset and upstream progression over the wing of vortex breakdown occurs at lower angles of attack as leading-edge sweep is decreased. Nonslender wings will have increased vortex breakdown aerodynamics within their practical operating envelope as compared to slender wing flows.

Experiments on the unsteady nature of vortex breakdown over delta wings have been given by Menke et al. [56] in 1999. In this work, coherent pressure fluctuations in the form of helical waves result from the helical-mode instability of swirling breakdown wake flow on delta wings. Detailed flow physics of the breakdown have also been studied with swirling flow in a pipe (Sarpkaya [57], Leibovich. [54], Leibovich [58]), Fig. 36(b). Despite the absence of the wing vortex sheet, the bursting in these pipe flows retains many similarities to the breakdown observed with wings. Multiple modes of vortex breakdown have been

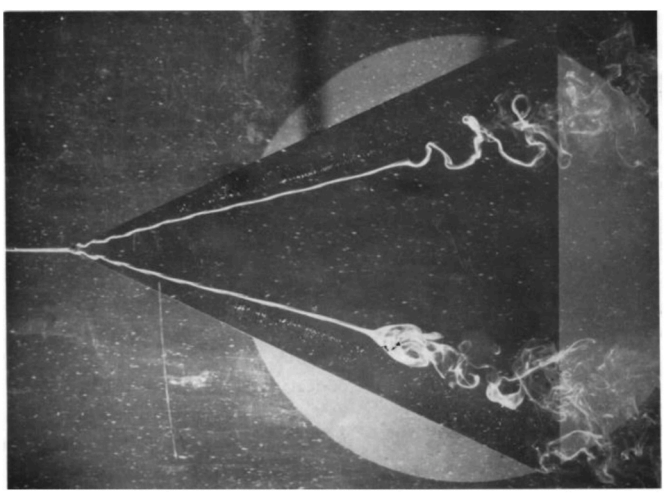

(a) 65° delta wing. Lambourne and Bryer [53], 1962.

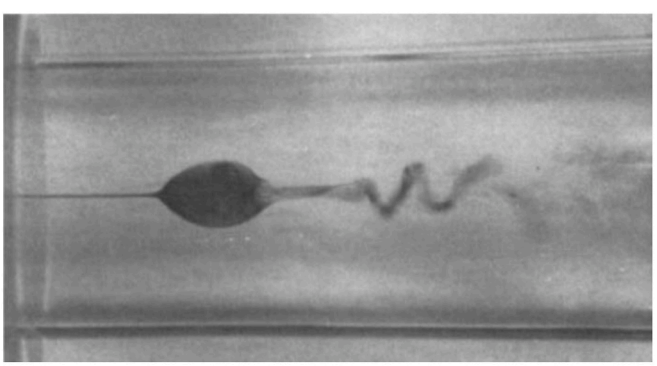

(b) Tube vortex. Leibovich [54], 1978.

Fig. 36. Vortex breakdown.

documented from experimental studies of tube vortices (e.g., Faler and Leibovich [59,60]).

A range of theoretical treatments of vortex breakdown has added understanding of this phenomenon (Hall [62]), but there is still no comprehensive theory for predicting vortex breakdown. CFD can simulate vortex breakdown, and one example is shown in Fig. 37 from Görtz [61] in 2005. However, accurate predictions of vortex breakdown, even for the sharp-edged slender delta wing, remain elusive.

Vortex breakdown and the associated unsteady flowfields can become more complex at higher speeds due to the added interaction with shock waves. An example is shown in Fig. 38 from Rizzi and Luckring [63] for a delta wing at $M = 1.1$ and $\alpha = 14°$; in this image the flow is from right to left. The vortex (labelled V) encounters an oblique shock wave which induces vortex breakdown along with a subsequent separation of the wing boundary layer (labelled S in the figure). Unit interactions for concentrated vortex flows were discussed earlier in Subsection 2.3.2.1, and Fig. 38 provides an example of higher-order interactions among three fluid entities: the wing boundary layer, an oblique shock wave, and the concentrated leading-edge vortex.

When vortex breakdown occurs near the apex of the wing, the unsteady vortical flow downstream of the burst location will envelope most of the wing. This occurs at high angles of attack for slender wings and at much lower (and practical) angles of attack for the nonslender wings. (See, Gursul et al. [65].) An example was given by Gordnier et al. [64] in 2009 for a 50° sharp-edged delta wing using the Air Force Research Laboratory (AFRL) high-order wall-resolved LES solver FDL3DI [66], Fig. 39. The concentrated vortex is coherent ahead of vortex breakdown whereas it becomes semicoherent aft of vortex breakdown. Time averaging for the mean vortex stricture tends to mask this change of state.

Several other unsteady phenomena occur for concentrated vortex flows that tend to be global for the nonslender wing. Vortex wandering, or meandering, can occur at relatively low frequencies about a mean vortex location. The vortex remains coherent, and the meander is often bound spatially and varies with angle of attack. (See, Menke and Gursul [67], 1997.) The vortex shear layer Kelvin-Helmholz instability, as shown in Fig. 22, also becomes unsteady for the nonslender wings. The shear-layer vortices can periodically roll up into discrete vortical structures. The shear-layer instability, unsteadiness and roll up are closely linked to the vortex/surface interaction and boundary-layer separation (Gordnier and Visbal [68], 1994). Depending on the aspect

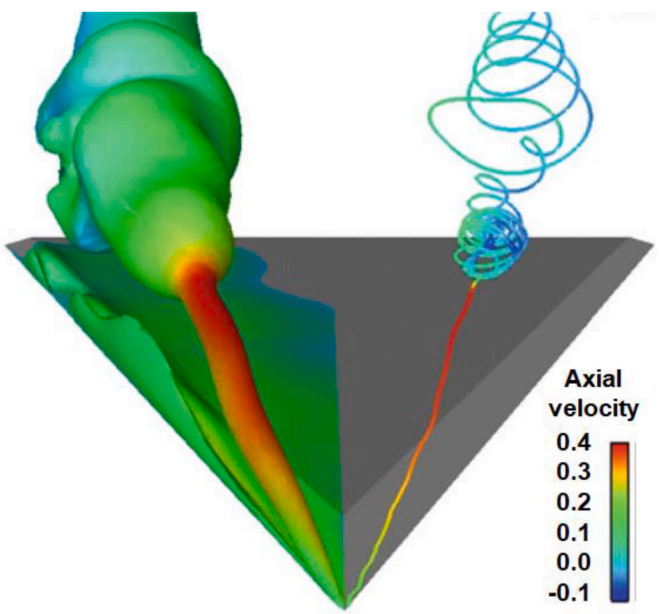

Fig. 37. Vortex breakdown RANS simulation. $\Lambda_{le} = 70°$, $M = 0.16$, $Re_{cr} = 1.97 \times 10^6$, $\alpha = 35°$. Görtz [61], 2005.

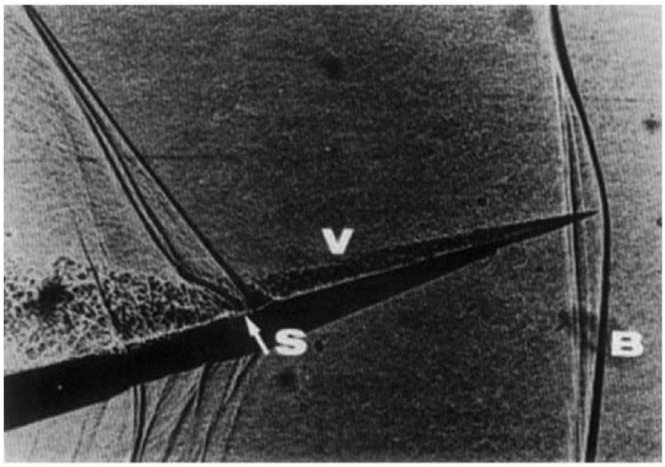

Fig. 38. Vortex breakdown due to oblique shock wave. $\Lambda_{le} = 65°$, $M = 1.1$, $Re_{cr} = 1.8 \times 10^6$, $\alpha = 14°$. Rizzi and Luckring [63], 2021.

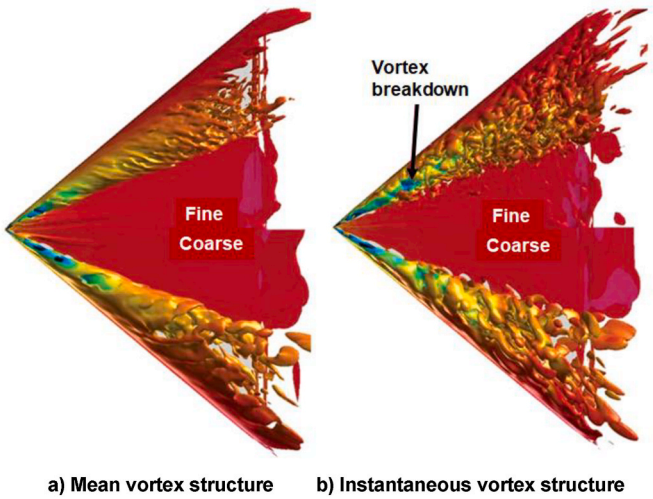

Fig. 39. Nonslender wing. WRLES, AFRL FDL3DI code. $\Lambda_{le} = 50°$, $M = 0.1$, $Re_{cr} = 0.62 \times 10^6$, $\alpha = 15°$. Gordnier et al. [64], 2009.

ratio, periodic vortex shedding can occur at very high angles of attack (Redinoitis et al. [69], 1993). All these phenomena contribute to both unsteady flow properties within the vortex as well as unsteady wing properties induced by the vortex. Additional review for unsteady flow phenomena over delta wings has been given by Gursul [70] in 1994 and Gursul and Xie [71] in 1999. Summary finding for unsteady concentrated vortex flows with steady boundary conditions are found in Subsection 3.1.2.1.

Unsteady boundary conditions, unsteady vortex flow: Maneuver conditions can introduce unsteady boundary conditions that alter the behaviour of concentrated vortex flows. Vortex hysteresis occurs that affects the strength and location of the vortex as well as vortex breakdown characteristics, as compared to the corresponding static case. Vortex hysteresis will occur for any unsteady motion with concentrated vortex flows and becomes more pronounced for higher rates of motion. Vortex hysteresis affects wing loads and these effects can be either favorable or adverse. A detailed review of the flow physics of pitching delta wings was given by Rockwell [72] in 1993. Some vortex hysteresis features observed with delta wings can also occur on slender forebody shapes.

One favorable unsteady effect is known as dynamic lift. Fig. 40 illustrates this phenomenon for a pitching delta wing with concentrated vortex flows. In the upstroke motion, more lift is created than for the

static wing at the same angle of attack because the vortex breakdown location lags (i.e., is further downstream) that of the static position. In the downstroke motion the vortex breakdown location also lags (i.e., is further upstream) that of the static position resulting in lower lift then the static case. Rapid pitch-up maneuvers can take advantage of this dynamic lift and may be of increased interest for UCAV concepts due to their increased g-limits as compared to piloted aircraft. Summary findings for unsteady concentrated vortex flows with unsteady boundary conditions are found in Subsection 3.2.3.2.

2.4. *Modelling and simulation technology considerations for concentrated vortex flows*

At typical full-scale flight conditions of $20 \times 10^6 < Re_c < 40 \times 10^6$, flows with concentrated vortices are mostly turbulent, so turbulence must be accounted for in a modelling and simulation technology. Accurate resolution or modelling of turbulence is key in obtaining correct and reliable CFD results. The principal difficulty of computing and modelling turbulent flows resides in the dominance of nonlinear effects and the continuous and wide spectrum of observed scales. A hierarchy of simulation technology is available for computing these vortical flows and these methods differ significantly in terms of resolved vs. modeled physics as well as computational resource requirements, A snapshot of the formulation hierarchy is presented in the following Subsection 2.4.1. All these formulations address macroscopic continuum fluid mechanics as represented with the Navier-Stokes equations, and the section concludes with a brief discussion of the mesoscopic approach based upon the Boltzmann equation. Some consequences due to these methods is presented in Subsection 2.4.2.

2.4.1. *Hierarchy of methods*

Why do we need to model turbulence? Can we resolve the turbulent concentrated vortex flowfield computationally, without the use of any modelling assumption? Let us address these questions by way of an overview.

In many vortex-aerodynamics applications, we are interested in mean or integral quantities like forces and moments on the aircraft, and computing turbulent flows with a turbulence model has proven to be an efficient and cost-effective way to obtain reliable solutions for a wide class of flight conditions. The flow physics in the solution, however, are constrained to those contained in the model. For cases where the physics are less certain, such as for vortex breakdown, one needs more general approaches.

Fig. 41, from Xiaoa and Cinnellab [73], illustrates the hierarchy of methods in descending order of complexity for resolving the flow physics. At the top of hierarchy, Direct Numerical Simulation (DNS) has the highest representation of the underlying fluid mechanics including turbulence with the least modelling approximations and the highest numerical cost. The bottom of the hierarchy, Reynolds-averaged Navier-Stokes (RANS) and unsteady RANS (URANS), has the lowest representation of underlying fluid mechanics with the most modelling approximations to turbulence, and lowest numerical cost. Turbulence itself contains a hierarchy of length scales, and this flow physics hierarchy is summarized in the following paragraphs along with the relation of the physics hierarchy to the computational formulation hierarchy of Fig. 41.

Fully developed turbulence contains eddies with a wide range of scales. These eddies interact with each other in a nonlinear fashion through their induced velocity fields, changing the orientation and shape of their neighbouring eddies. The net effect of this change-of-shape (i.e., straining) process is to 'cascade' kinetic energy from the largest to the smallest scales of the turbulence, as depicted in Fig. 42, where the turbulent kinetic energy is shown as a function of the wave number $k = 2\pi/\lambda$, and λ is the length scale of the flow features, i.e., the eddies. The full spectrum in wall turbulence is often divided into several ranges, including (i) a low-wave-number energy-containing range, termed the "integral" range in textbooks (Wilcox [74]), (ii) an intermediate range in which the motions scale on the distance from the wall (the attached eddies), and (iii) a high-wave-number dissipation range in which the motions are comparable in size to the viscous or Kolmogorov length scale.

As a result, the largest eddies are the most energetic, and their size, shape and speed are set by the details of the flow configuration and are not directly affected by the viscosity of the fluid. The size of the smallest eddies, on the other hand, is determined both by how much energy enters the cascade at the large scales and by the fluid's viscosity. The primary role of viscosity is to define the scale at which the energy is dissipated. The Reynolds number of the flow thus determines how small the smallest scales are, relative to the largest eddies. The subrange that overlaps the attached eddy and dissipation regions is where the energy is transferred by inertial mechanisms from low to high wave numbers and is known as the inertial subrange. The slope of the spectrum is −5/3 in the log-log representation of Fig. 42.

If, in our simulation, we want to resolve all the scales of motion, the

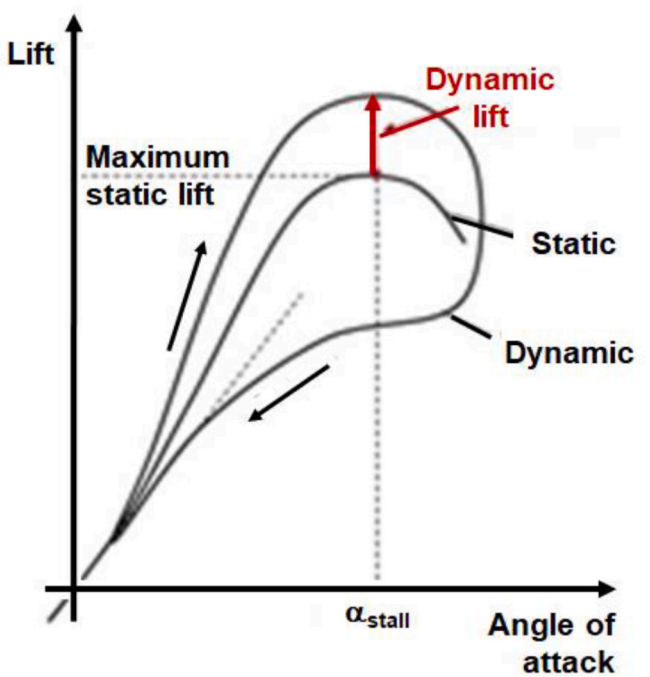

Fig. 40. Unsteady aerodynamic coefficients for a slender delta wing. Le Moigne [37], 2004.

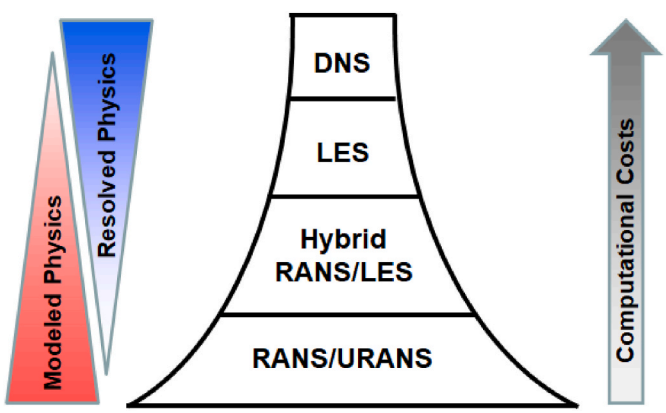

Fig. 41. Computational formulation hierarchy. Xiaoa and Cinnellab [73], 2019.

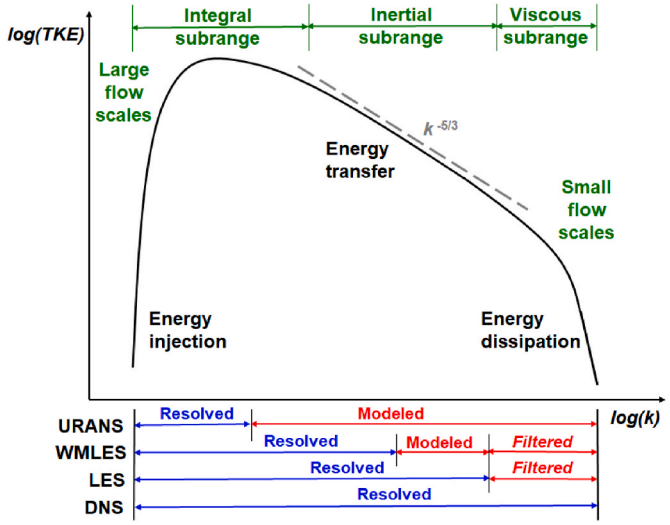

Fig. 42. Turbulence energy spectrum.

number of grid points we need in each direction becomes proportional to the ratio between the largest eddy, l_{LE}, and the smallest eddy, l_K (Kolmogorov scale), in the flow. This ratio is proportional to $Re_L^{3/4}$ (where Re_L is the Reynolds number based on an integral scale L of the flow). Thus, the number of points in three dimensions is:

$$N_x \times N_y \times N_z \propto \mathrm{Re}_L^{9/4}$$

effectively placing a Reynolds number constraint on any such simulation.

Fig. 42 also shows three classes from the computational hierarchy of Fig. 41, including two types of LES, and how these methods resolve, model, and/or filter the turbulence hierarchy. The formulation for each of the computational classes shown in Fig. 41 are briefly summarized in the following sections, and an application that is representative of contemporary practices is also included.

2.4.1.1. Direct numerical simulation. *Formulation:* The approach called Direct Numerical Simulation, or DNS in short, solves directly the governing equations of fluid flows, the Navier-Stokes equations, without the use of any modelling assumption. It requires solving the extensive range of temporal and spatial scales of a turbulent flow, from very large to very small, down to the Kolmogorov length scale. An estimate for the mesh resolution and time steps required to correctly solve the complexity of the fluid structures scales approximately with the cube of Reynolds number, thus making the DNS approach virtually impossible for flight conditions using current and anticipated computers. DNS is indeed almost exclusively used in academia and research institutions to model unit-problem flows and, along with experiments at wind tunnel Reynolds numbers, it is used to improve the understanding of turbulence and to develop simplified turbulence models that are less expensive to calculate but still useful to predict the main contribution of turbulence in the flow.

Representative applications: In 2016, Hosseini et al. [75] carried out a three-dimensional direct numerical simulation to study the turbulent flow around the asymmetric NACA 4412 wing section at a freestream Mach number of $M = 0.04$, a moderate chord Reynolds number of $Re_c = 0.4 \times 10^6$, and an angle of attack $\alpha = 5°$. The mesh was optimized to properly resolve all relevant scales in the flow and comprises around 3.2 billion grid points. The incompressible spectral-element Navier–Stokes solver Nek5000 performed the simulation in approximately 35 million core-hours over approximately 6 months of computer occupancy. The simulation advanced the flow approximately ten chord lengths. An unsteady volume force was used to trip the flow to turbulent on both sides of the wing at 10% of the chord. Full turbulence statistics are computed in addition to collection of time history data in selected regions revealing details of incipient separation on the upper surface. This simulation shows the potential of high-order (spectral) methods in simulating turbulent vortex shedding over a wing section at moderately high Reynolds numbers.

Fig. 43 shows vortex visualization of coherent vortices obtained from an instantaneous DNS field by means of the λ_2 criterion clearly showing the emergence of hairpin vortices immediately after the tripping strip, which leads to the development of a turbulent boundary layer. The comparison of streamwise mean velocity from the RANS and the DNS (in this case, obtained from the time- and spanwise-averaged field), as shown in Fig. 43(b), indicates how accurately RANS simulates this turbulent flow with the Swedish Defense Research Agency (FOI) EDGE code running an explicit algebraic Reynolds stress model (EARSM). This correlation also implies that the DNS results could be of interest for assessment of the EARSM turbulence modelling details.

2.4.1.2. Large eddy simulation. *Formulation:* In large eddy simulation (LES), the smallest scales of turbulence are spatially filtered out while the largest, most energy containing scales are resolved directly. Due to the nature of turbulence, at a very small scale, the flow structures tend to be similar to each other even in different applications. This allows the use of simpler turbulence models that tend to be more universal and can be applied to several applications with a reduced requirement of model tuning. Because LES still resolves the flow to the wall, it is equivalently referred to as wall-resolved LES (WRLES).

Similarly to RANS modelling, in LES turbulence models aim at resolving the unknown terms in the filtered Navier-Stokes equations, called the Sub-grid Scale stresses. The term comes from the fact that in most LES models, the filtering of the equations is obtained at mesh size level, relegating the modelling to flow scales smaller than the grid size.

LES modelling reduces numerical expenses as compared to DNS but is still very resource intensive by current standards. Compared to URANS, LES offers increased range of flow physics applicability with increased solution fidelity, but all of this comes with a significantly increased computational cost due to the time step requirements and increased mesh resolution required to capture the more detailed flow.

The LES flow field is redefined in terms of its filtered average and the unfiltered portion of the flow occurring on small length scales and small time scales, called the subgrid scale portion. Mathematically, the total flow is defined as a superposition of these two contributions. Conceptually, this gives two regions where the system can be described—within the highly sensitive spatially/temporally averaged region and in the subgrid region where flow can be described with a separate model.

Large eddy simulation involves solving the discretization of the filtered equations by CFD. LES resolves scales from the domain size L down to the chosen filter size Δ. This requires accurate discretization by high-order numerical schemes, or fine grid resolution if low-order numerical schemes are used. Ghosal [76] found that, for low-order discretization schemes, such as those used in finite volume methods, the truncation error can be the same order as the subfilter scale contributions, unless the cell size is considerably smaller than filter width Δ. Additional details of LES formulations, including recommended practices and research opportunities, have been given by Georgiadis et al. [77] in 2010. Recommended practices are still evolving at the time of this article, and in many instances handcrafted approaches are employed as part of the LES research.

Representative applications: An application of LES for a finite wing with a tip vortex has been given by Garman and Visbal [78,79] in 2017. High-fidelity implicit large-eddy simulation was used to investigate the dynamics of wingtip vortices formed on an aspect-ratio-four NACA 0012, rounded-tip wing at $Re_c = 0.2 \times 10^6$ for incidence of $4° \leq \alpha \leq 16°$. At its initial separation and inception, the tip vortex core exhibited a strengthening favorable pressure gradient with increased angle of attack

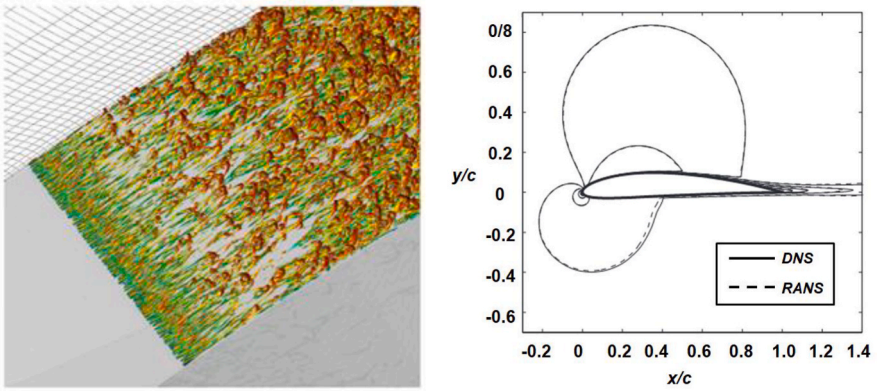

(a) Instantaneous DNS hairpin vortices, λ_2 criterion. **(b) Averaged chordwise velocities.**

Fig. 43. Comparison of DNS and RANS solutions. NACA 4412 airfoil, $M = 0.04$, $Re_c = 0.4 \times 10^6$, $\alpha = 5°$. Hosseini et al. [75], 2016.

that promoted acceleration of its axial flow to values higher than the freestream speed for $\alpha \geq 8°$, or jet-like vortices. Approaching the trailing edge, however, the core was subjected to an adverse pressure gradient that decelerated the core flow before entering the wake. The extent and strength of this adverse region grew with increased incidence, but it did not reach a sufficient level to stagnate the core flow and cause breakdown for the conditions examined.

Fig. 44(a) compares the instantaneous and time-averaged flow structure for $\alpha = 16°$ with isosurfaces of stagnation density. The unsteady shear-layer structures of the instantaneous flow were also quite evident in the time-averaged realization. This revealed that, despite the complex vortex interactions, the formation, separation, and entrainment of these discrete features over the wing were stationary events, i.e., fixed in space and time. The turbulent region inboard of the tip region, however, were uncorrelated in time leading to a smooth, continuous isosurface in the time-averaged solution.

The time-averaged solutions at the other angles of attack (Fig. 44(b)) also preserved the side-edge vortex structure as well as a smaller vortical structure inboard of the side-edge vortex. This smaller vortex appears to be a manifestation of an inner vortex for blunt-side-edge vortex separation that was discussed conceptually for blunt-leading-edge vortex separation (Figs. 25 and 30). This conceptual vortex topology is captured by the WRLES simulation for the blunt-side-edge vortex flow. It should be noted that the helical pattern of corotating shear-layer vortices present in both the instantaneous and time-mean flow resembles very closely the process described in the context of delta-wing vortices.

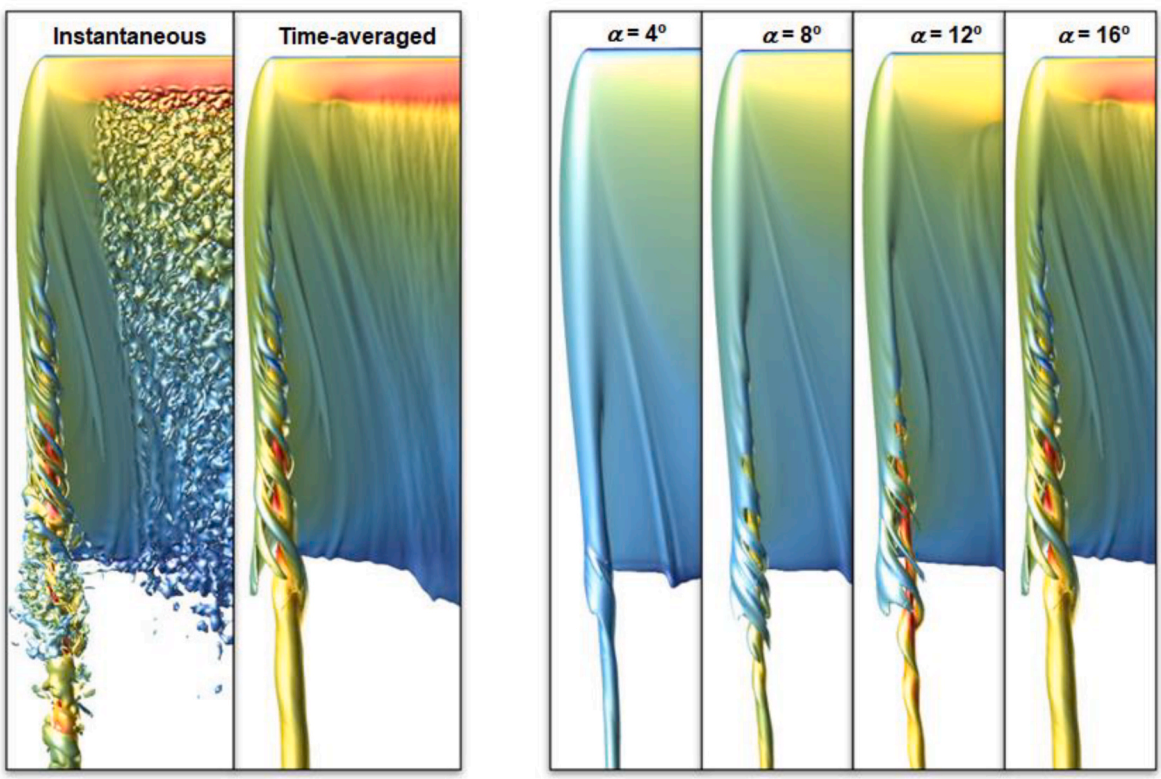

(a) Instantaneous and time-averaged flowfields, $\alpha = 16°$ **(b) Angle of attack effects, time-averaged flowfields.**

Fig. 44. $AR = 4$ wing solutions with an NACA 0012 airfoil. WRLES, AFRL FDL3DI code. $M = 0.1$, $Re_c = 0.2 \times 10^6$. Garman and Visbal [78], 2017.

2.4.1.3. Reynolds-averaged Navier-Stokes. Formulation: The solution of the Reynolds-averaged Navier-Stokes (RANS) equations is the tool that is most commonly applied, especially in industrial applications, to the solution of turbulent flow problems of high Reynolds number. The RANS equations are obtained for "steady" turbulent flow by time-averaging and for unsteady cases by ensemble-averaging (yielding URANS) the Navier-Stokes equations to yield a set of transport equations for the averaged momenta. The situation is sketched in Fig. 45. The time interval Δt for the averaging should be large compared to the typical timescale of the turbulent fluctuations. For $\Delta t \to \infty$, the steady RANS equations appear. A finite (but unspecified) Δt that is much shorter than the period of mean-flow unsteadiness allows unsteady URANS simulations.

Time or ensemble averaging results in a system of equations with new unknown terms, the Reynolds stress tensor. The function of turbulence modelling is to devise approximations for the Reynolds stresses in terms of mean flow properties to close the systems of equations. Turbulence models for the RANS equations (identical models for URANS) have been the object of much study over the last 30 years, but no model has emerged that gives accurate results in all flows without *ad hoc* adjustments of the model constants (see Wilcox [74] 2006). This may be because the large, energy-carrying eddies are much affected by the boundary conditions, and universal models that account for their dynamics may be impossible to develop.

Two basic levels of classical turbulence models are:

- Eddy viscosity/diffusivity models, known also as first-order models since the quantities modeled are scalars, such as turbulent kinetic energy k and its dissipation rate ε
- Second-moment closure models, known as Reynolds stress models (RSMs). These models approximate the individual Favre/Reynolds stress components.

Each category has several variants. The first-order models are categorized according to the number of equations they solve. In second-order models, if the equations for the stresses are algebraic, the models are known as algebraic RSMs (ARSMs) or, equivalently, Explicit Algebraic Reynolds Stress Models (EARSMs).[5] The most advanced models solve differential transport equations for the second moment and are known as differential RSMs (DRSMs).

First-order models are classified according to the number of additional transport equations for the turbulent quantities they require. The algebraic, or zero-equation, models are therefore the simplest. Methods using one additional differential equation are common (e.g., the Spalart–Allmaras model solves a single transport equation for the eddy viscosity) as are methods using two additional differential equations (e.g., the $k-\omega$ models with transport of turbulent kinetic energy k and ω, a frequency scale for the turbulent fluctuations).

Eddy-viscosity models perform reasonably well in attached boundary-layer flows as long as only one component of the Reynolds stress tensor is significant. In these cases, one could consider the eddy viscosity to represent that significant Reynolds stress component. But for more complicated flows where this is not the case, the validity of the eddy-viscosity approach is questionable. Two-equation turbulence models, such as $k-\varepsilon$ and $k-\omega$, are incapable of capturing the effects of anisotropic normal stresses. They also fail to correctly represent the effects on turbulence of extra strains and body forces. The second-moment closure models (i.e., RSMs) incorporate these effects exactly, but several unknown turbulence processes (e.g., pressure–strain correlations, turbulent diffusion of Reynolds stresses, dissipation) need to be approximated.

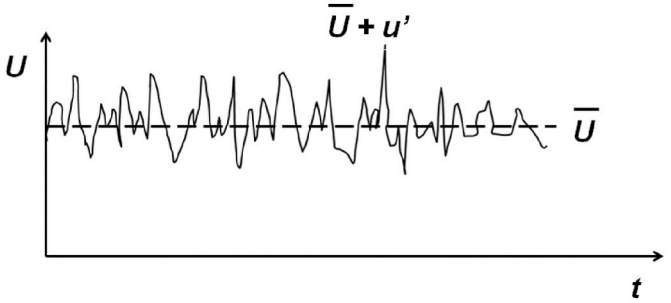

Fig. 45. Reynolds averaging: turbulent velocity fluctuations u' and statistical mean value $\bar{U}$.

In large-eddy simulation (LES), the large, energy carrying eddies are computed, whereas only the small, subgrid scales of motion are modeled. LES can be more accurate than the RANS approach because the small scales tend to be more isotropic and homogeneous than the large ones, and thus more amenable to universal modelling.

Representative applications: NASA executed the High Angle-of-Attack Technology Program (HATP) from the mid-1980s to the mid-1990s to assess performance enhancements and quantify flow properties of an F/A-18 aircraft known as the High Alpha Research Vehicle (HARV). Details of the program have been summarized by Hall et al. [80] in 1996 and the program was leveraged for CFD assessments of concentrated vortex flows with the emerging RANS simulation capability. Among several analyses, the RANS simulations by Ghaffari et al., in 1990 [81] and 1993 [82] demonstrated good correlations with flight measurements for the forebody attached flow and the LEX concentrated vortex flow at a subsonic maneuver condition ($M \approx 0.3$, $Re_c \approx 13 \times 10^6$ and $\alpha = 19°$). The HATP demonstrated that emergent RANS-based technology could successfully simulate concentrated vortex flows on a complex configuration at flight conditions. The breadth of this capability remained to be determined.

A second flight test program was executed in the 1990s to obtain wing vortex flow measurements using an F-16XL aircraft (Lamar et al. [83]). The program, known as the Cranked Arrow Wing Aerodynamics Program (CAWAP), provided in-flight measurements of static surface pressures, boundary layer profiles, and surface flow patterns at subsonic, transonic, and supersonic speeds. A subsequent international program [84], CAWAPI, was performed under the NATO Research and Technology Organization (RTO) to predict a subset of these data using both RANS and hybrid RANS/LES techniques. Results are shown in Fig. 46 from Rizzi et al. [85] for Flight Condition 7 ($M = 0.304$, $Re_{cref} = 44.4 \times 10^6$, $\alpha = 11.9°$), a case of fully developed vortical flow over the wing upper surface with no appreciable breakdown before the trailing edge (of at least the inner-wing vortex). The convergence-divergence of skin friction lines in Fig. 46(a) indicates the occurrence and location of primary or secondary vortex separation-reattachment, respectively. At Fuselage Station 300 (FS 300) in Fig. 46(b), there is some spread in the peak values at 80% span, and one set of results showed a strong secondary vortex peak. In general, RANS techniques did a good job predicting the primary vortex suction peak at this moderate maneuver condition. (See, Rizzi et al. [86].)

Fig. 47 presents comparisons of the computed and measured velocity profiles in the upper-surface boundary layer at four spanwise rake locations. Each rake was oriented into the local flow direction in an average sense, and the velocity profiles are normalized by the velocity at the edge of the rake measurements. Results are shown on a logarithmic scale of the vertical distance z over the upper surface to give a better view of the slope of the profile near the wall. The measured results do not go much below 1 mm above the wing. The rake flowfields correspond to: (rake 3) near the primary reattachment line, (rake 4) underneath the primary vortex, (rake 5) near the secondary reattachment line, and (rake 7) underneath the secondary vortex. There are substantial

[5] These model names, as well as Explicit Algebraic Stress Models (EASMs), all refer to the same thing. There are, however, various versions of these models in two-equation form. Additional discussion can be found at the NASA Langley Turbulence Modelling website [201].

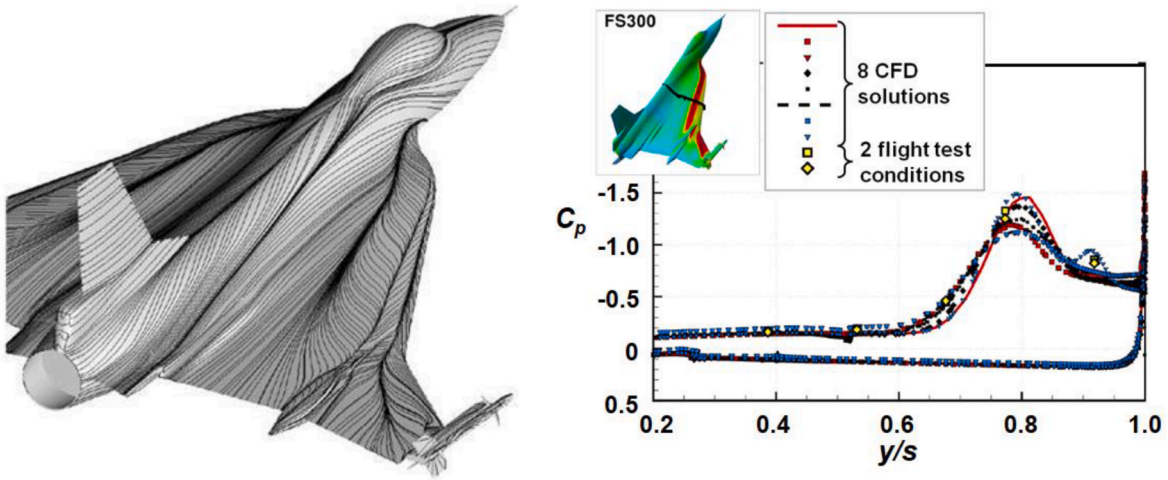

(a) Surface flow pattern **(b) Spanwise pressure predictions, *FS 300***

Fig. 46. Primary vortex predictions (RANS), CAWAPI. $\Lambda_{le} = 70°/50°$, *FC-07*: $M = 0.304$, *Recref* $= 44.4$ x 10^6, $\alpha = 11.9°$. Rizzi et al. [85], 2007.

flow dynamics taking place throughout these locations, and an equilibrium boundary layer cannot be assumed. Nevertheless, if the outlier computation (No 8) at Rake 7 is ignored, the computed RANS solutions correlate reasonably well with the measured values at all four rake positions.

Differences among the RANS simulations included grid resolution and turbulence models, and this led to differences in the computed boundary-layer profile details. At rake 3, above 1 mm, the computation 4 and 5 results are too full, but below 1 mm these appear to rejoin the trend of the other computed results. At rake 4, the computational results

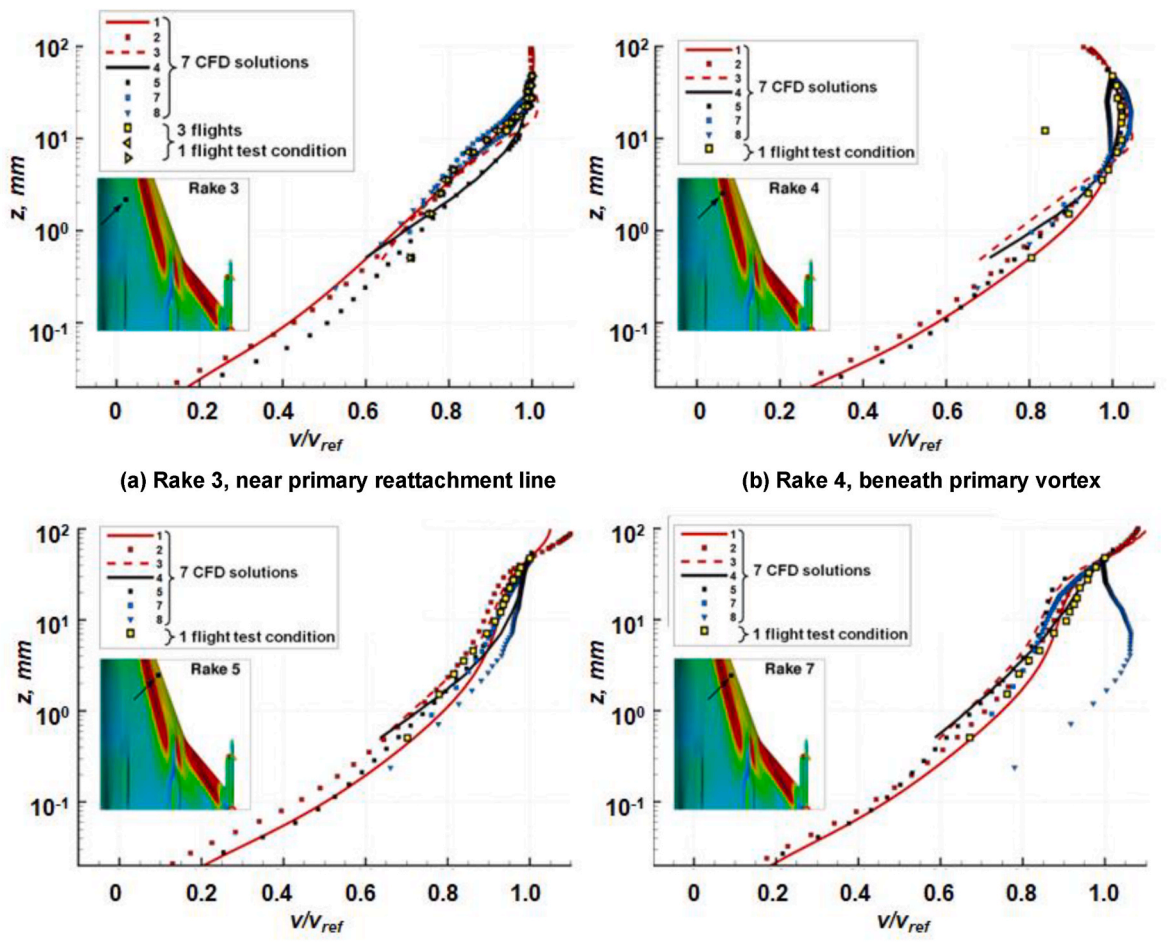

(a) Rake 3, near primary reattachment line **(b) Rake 4, beneath primary vortex**

(c) Rake 5, near secondary reattachment line **(d) Rake 7, beneath secondary vortex**

Fig. 47. Computed (RANS) and measured upper-surface boundary-layer profiles at four locations. *FC-07*: $M = 0.304$, *Recref* $= 44.4$ x 10^6, $\alpha = 11.9°$. Rizzi et al. [85], 2007.

are too full above 1 mm and rejoin the trend of the other computed results smoothly below 1 mm. At rake 5, it is the computation 8 results that are too full above 1 mm. Below 1 mm, the spread in the band of computed results is larger than at the previous two rake stations. At rake 7, apart from the computation 8 results, those of computation 1 are next most full above 1 mm. Below that level the spread in the band is less than in rake 5. Additional research would be needed to resolve these differences across these vortex/boundary-layer interaction domains.

2.4.1.4. Extensions to LES methods. *Near-wall dilemma of LES*: A turbulent boundary layer is truly a multi-scale phenomenon, and therein lies the (near-wall) problem - due, in large part, to the excessive computational cost of handling boundary layers where the turbulence kinetic energy is carried by eddies of different sizes in layers near and far from the wall.

That boundary layers by their very nature are thin relative to other dimensions makes their computation significantly costly regardless of how they are modeled, because smaller eddies dominate the inner part of the boundary layer $y/\delta < 0.2$ requiring finer grid spacing there, and larger eddies in the outer part $y/\delta > 0.2$ where the grid can be coarser. And the computational cost becomes acute at high Reynolds numbers.

In 2016 Larsson et al. [87] estimated the number of grid points required for LES simulation of a more realistic example: a NACA 0012 airfoil at $M = 0.1$ and $\alpha = 2.5^\circ$ angle of attack. The total (integrated along x) grid requirements are given in Table 1. The numbers are comparable to an estimate by Spalart et al. [88] from 1997. For every order-of-magnitude increase in chord Reynolds number, the number of inner-layer points increases by approximately two orders of magnitude. The growth of points in the outer layer is much slower. Increases in Re_τ (computed from friction velocity at wall) were comparable to the increase in chord Reynolds number. At a representative full-scale Reynolds number of 40×10^6, an LES simulation of this subcritical attached flow would require approximately 33 billion grid points. The introduction of additional flow physics, such as supercritical or separated flow, would likely increase this grid requirement. LES simulations are prohibitively expensive at moderate to full scale Reynolds numbers; this limitation is significantly exacerbated by three-dimensional applications.

Because of the high computational effort for resolving the energetic structures in the inner layer, many approaches have been proposed over the last 50 years to solve this "near-wall dilemma of LES." The approaches share a common objective: to model the turbulence in the inner part of the boundary layer, thus removing the need to resolve the flow there with the LES grid. These approaches are known as Wall-Modeled Large Eddy Simulation (WMLES). Interestingly, despite the decades of WMLES research, no well-established guidelines have been developed for many modelling choices, in particular for necessary grid resolution, but also for grid-cell topology, numerical schemes, subgridscale modelling, etc.

Wall-Modeled LES (WMLES) formulation: Many approaches to WMLES exist, but arguably the most wide-spread is so-called wall-stress modelling, which aims at incorporating the effect of inner-layer dynamics by predicting and enforcing the correct local value of the wall shear stress. The methods differ in their treatment of the outer part of the boundary layer, specifically whether this is modeled as it is in the original version of detached eddy simulation or resolved.

The principle of wall-stress-modeled LES is sketched in Fig. 48, an instantaneous snapshot of a boundary layer with overlaid LES grid, where the grid-spacing Δx_i in all directions is determined solely by the boundary-layer thickness δ. The idea can be stated in the following way: given an instantaneous velocity u_i at height $y = h_{wm}$ above the wall, estimate the instantaneous wall shear stress vector $\tau_{w,i}$. The wall model approximates the flow in a layer of thickness h_{wm}, chosen to fall within the log-layer. It is fed instantaneous velocity and temperature information from the LES and returns the instantaneous wall stress and heat flux to the LES, which then uses these as the wall boundary condition.

Fig. 49 illustrates how wall modelling reduces the grid size in two ways. In Fig. 49(a), the grid in the inner layer is dense and geared to x^+ and y^+ scales so that all the turbulent eddies within it are resolved. Due to constraints on grid smoothness and continuity, when the inner-layer grid is extended into the outer layer, it over-resolves the much larger turbulent eddies there, causing an excessive grid size. In Fig. 49(b), wall modelling removes the need for the inner grid, and frees the generation of the outer-layer grid to be sized appropriately to the turbulent eddies found there, on scales of some fraction of the boundary-layer thickness δ. These two effects lead to a large reduction in the overall grid size.

The models in WMLES formulations are being developed in close conjunction with WRLES simulations.

WMLES application: WMLES formulations are beginning to be used for complex separated flow analysis. One example is the prediction of $C_{L,max}$ aerodynamics about the High-Lift Common Research Model (CRM-HL) configuration as part of the high-lift prediction workshop series. Summary findings have been given by Kiris et al. [90] and Rumsey et al. [91], and the WMLES predictions of the maximum-lift flowfields, with numerous separated flow regions, appears to be promising. However, at the time of this publication the authors are unaware of applications of WMLES to concentrated vortex flows.

Hybrid RANS/LES Formulation: RANS methods have demonstrated an ability to predict attached flows very well at a relatively low computational cost. LES methods, on the other hand, have been shown to compute separated flow fields accurately. Although the computing cost of LES for turbulent flows is significantly less than that of direct numerical simulation (DNS), it is still too expensive for engineering applications involving thin boundary layers near surfaces, since the resolution needed to capture these layers results in exorbitant demands on central processing unit power and memory.

Spalart et al. [88] proposed a hybrid RANS/LES turbulence model based on the one-equation Spalart-Allmaris (SA) eddy viscosity model as an alternative approach to WMLES. This hybrid RANS/LES method was originally referred to as detached-eddy simulation (DES) and employs traditional RANS turbulence models for the near-wall region. Aimed at high-Reynolds number separated flows, it switches from RANS turbulence modelling in the wall boundary layer to LES farther away, improving results noticeably over pure RANS models. This is critical to obtaining accurate estimates of aerodynamic loads for massively separated flows with unsteady content, such as the flow over delta wings,

Table 1
Total grid points required for LES on the upper surface of a NACA 0012 airfoil. $M = 0.1$, $\alpha = 2.5^\circ$, various Reynolds numbers. Larsson et al. [87], 2016.

	$Re_c = 10^6$	$Re_c = 10^7$	$Re_c = 10^8$
Inner layer ($y/\delta < 0.2$)	1.6×10^7	1.9×10^9	2.0×10^{11}
Outer layer ($y/\delta > 0.2$)	3.3×10^7	7.2×10^7	2.5×10^8
Re_τ at trailing edge	1×10^3	1×10^4	7×10^4

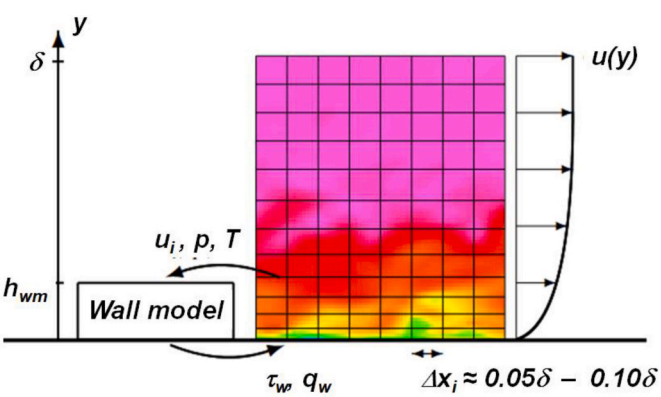

Fig. 48. WMLES concept. Larsson et al. [87], 2016.

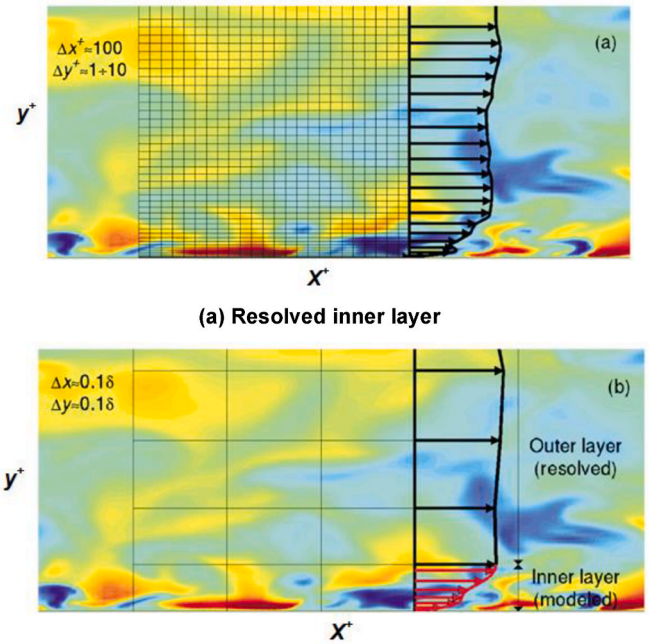

Fig. 49. Wall-layer modelling philosophy. Piomelli et al. [89], 2002.

forebodies, and configurations at high angle of attack.

In the hybrid RANS/LES approach, the length scale d in the destruction term of the SA model is modified so that the eddy viscosity crosses over from the usual SA RANS eddy viscosity near the wall to a proposed LES eddy viscosity, similar to that defined by Smagorinsky for LES, away from the wall. The SA wall destruction term, which reduces the turbulent viscosity in the laminar sublayer, is proportional to (ν_T/d),[2] where ν_T is the eddy viscosity and d is the distance to the nearest wall. When this term is balanced with the production term, the eddy viscosity becomes proportional to Sd,[2] where S is the local strain rate. The Smagorinsky LES model, on the other hand, varies its subgrid-scale (SGS) turbulent viscosity as follows:

$$\nu_T \propto S\Delta^2$$

where Δ is the diameter of the cell. Thus, if d is replaced with Δ in the wall destruction term, the SA model will act as a Smagorinsky LES model. Consequently, the DES formulation is obtained by replacing in the SA model the distance to the nearest wall, d, by d_1, where d_1 is defined as follows:

$$d_1 \equiv min(d, \text{CDES}\ \Delta)$$

Thus, the switch from RANS to LES depends on the spatial discretization. When the length scale d is smaller than the wall-parallel grid spacing Δ, which is typically the case for the highly stretched cells in the boundary layer, the model acts in RANS mode. When d is larger than Δ, the model acts in Smagorinsky LES mode. This is illustrated in Fig. 50 from Görtz [61]. This approach introduces only one additional model constant (CDES = 0.65) in the one-equation SA model.

A powerful feature of hybrid RANS/LES is that it directly resolves turbulent eddies with increasing fidelity as the grid is refined. RANS computes the mean flow, and grid refinement is to ensure grid-convergence of the numerical solution. In the fine-grid limit, the accuracy of RANS predictions is controlled by the turbulence model. In LES and hybrid RANS/LES, on the other hand, grid refinement resolves additional physical features and decreases the contribution of the turbulence model to the solution. The fine-grid limit of LES is a DNS solution free of turbulence modelling errors.

Although DES is not a zonal method, flow regions with very different gridding requirements emerge. Spalart [23] has given some guidelines for creating grids suitable for hybrid RANS/LES. He points out that it is desirable to have isotropic grid cells (cubic for structured grids) in the "LES region," in which unsteady, time-dependent features are resolved. Isotropic cells are desired because they ensure the lowest value of Δ for a given cell volume, lowering the eddy viscosity. In addition, the orientation of flow structures is not known *a priori*, so isentropic cells represent a logical approach to resolving turbulent length scales.

Several advances to the original DES implementation of hybrid RANS/LES formulation have been developed. Two if these, Delayed Detached Eddy Simulation (DDES) and Improved Delayed Detached Eddy Simulation (IDDES) are briefly summarized. The DES solution has been found to suffer from early separation, and the main idea of DDES is to avoid zonal measures, thus leaving it to the solution process to determine. DDES detects boundary layers and prolongs the full RANS mode, even if the wall-parallel grid spacing would normally activate the DES limiter. This detection device depends on the eddy viscosity, so that the limiter now depends on the solution.

Improved Delayed DES (IDDES) is more ambitious yet. The approach is also nonzonal and aims at resolving log-layer mismatch. One basis is a new definition of Δ, which includes the wall distance and not only the local characteristics of the grid. The modification tends to depress Δ near the wall and give it a steep variation, which stimulates instabilities, boosting the resolved Reynolds stress. Other components of IDDES include new empirical functions, some involving the cell Reynolds number, which further address log-layer mismatch.

Hybrid RANS/LES application: In 2003, Forsythe et al. [92] showed hybrid RANS/LES simulations using the Cobalt Solutions Cobalt code for a complete F-15E at an extreme angle of attack. Two of his results are reproduced in Fig. 51. Fig. 51(a) illustrates the complex vortical separations that were captured in this simulation. These appear to include coherent forebody vortices and incoherent vorticity over the aft wing; semicoherent vortex flows are likely also present but cannot be assessed from this figure. Fig. 51(b) contrasts unsteady RANS (URANS) and hybrid RANS/LES simulations for this case with massively separated flow. The cut over the wing shows instantaneous vorticity contours and clearly demonstrates the feature resolving capacity of the hybrid RANS/LES approach. Forsythe reported that these URANS simulations did not exhibit any significant unsteadiness, and they have virtually no vorticity content over the wing. The hybrid RANS/LES formulation appears to be necessary for simulating flows with significant unsteady separated flow.

Forsythe's work further demonstrated incoherent vorticity simulation capability, now including massively separated wing-stall flows about a complex aircraft configuration, by a hybrid RANS/LES formulation even without adaptive gridding.

2.4.1.5. Distinction among LES, WMLES and hybrid RANS/LES. It is

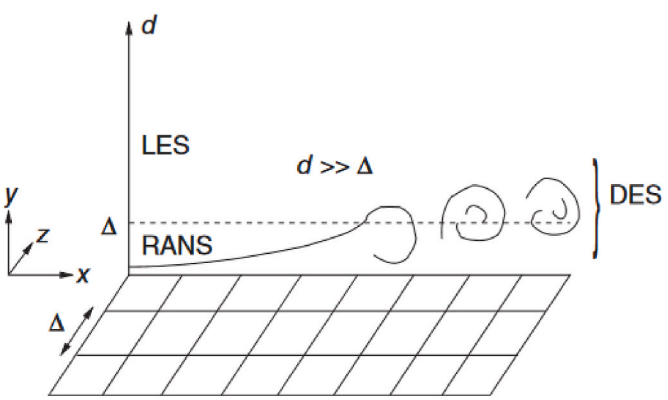

Fig. 50. Schematic of detached-eddy simulation. Görtz [61], 2005.

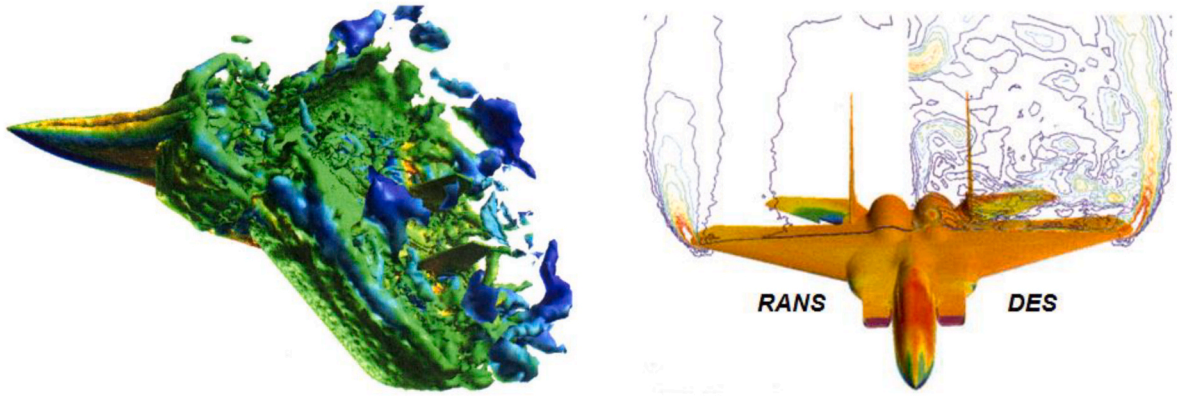

(a) Complex separated flow content. (b) Governing equation effect.

Fig. 51. F-15E example. Hybrid RANS/LES, Cobalt Solutions Cobalt code. $\Lambda_{le} = 45°$, $M = 0.3$, $Re_c = 13.6 \times 10^6$, $\alpha = 65°$. Forsythe et al. [92], 2004.

important to realize that wall-modeled LES and the original version of hybrid RANS/LES as conceived in 1997 by Spalart et al. [88] (DES97) are very different methods in terms of philosophy, computational cost, and potential accuracy. Consider three distinct regions of the boundary-layer flow: (a) the wall-bounded inner part of the boundary layer, (b) the outer part of the boundary layer; and (c) the detached shear layers. The energetic and dynamically important motions are resolved (above the SGS threshold) in all these regions in wall resolved LES.[6] The important distinction is that wall-modeled LES resolves the energetic motions in regions (b) and (c), while hybrid RANS/LES only resolves those in region (c). This distinction is very important: it means that WMLES has the potential to be significantly more accurate than hybrid RANS/LES in non-equilibrium flows. In RANS and hybrid RANS/LES, the accuracy of the turbulence model in the non-equilibrium (e.g., adverse pressure-gradient) boundary layer is likely to determine the accuracy of the overall simulation (for flow separation over a smooth surface, or a similar flow). In WMLES, however, approximately 80% of the boundary layer is treated by LES, which is perfectly capable of capturing any non-equilibrium effects. Provided that the outer layer LES is accurate, the wall-model is fed accurate instantaneous information, regardless of whether the wall-model itself accounts for non-equilibrium effects or not.

2.4.1.6. A mesoscopic approach: Lattice Boltzmann methods. Traditional CFD methods address macroscopic continuum fluid mechanics as represented by the Navier-Stokes equations. Unlike these methods, Lattice Boltzmann Methods (LBMs) adopt a mesoscopic approach based upon the Boltzmann equation. A hierarchy of fluid dynamic modelling scales is shown in Fig. 52 from Han and Ryozo [93]. With a LBM, the fluid is represented by fictive discrete particles at a mesoscopic scale, and such particles perform consecutive propagation and collision processes over a discrete lattice. Each node stands as a computational point with an associated distribution function that reflects the likelihood of particle groups moving in specific directions with specific velocities.

The fundamental idea of the LBM is to construct simplified kinetic models that incorporate the essential physics of microscopic processes at a mesoscopic scale. The microscopic process is small scale chaotic and needs spatial averaging to produce the mesoscopic quantities. The collisions operate on a mesoscopic scale that is based on the size of the grid, a size significantly larger than microscopic particle interaction length scales (i.e., a mean free path of ~70 nm). When averaged, the mesoscopic lattice Boltzman properties obey the macroscopic Navier-Stokes equations. The basic quantity of the LBM is the discrete-velocity distribution function, often called the particle populations, which represents the density of particles with velocity at a position and time. As in other numerical methods for solving the Navier-Stokes equations, a subgrid-scale (SGS) model is required in the LBM to simulate turbulent flows at very high Reynolds numbers. Due to its particulate nature and local dynamics, LBM is particularly amenable to parallelization of the solution algorithm. The lattice-Boltzman approach engenders its own hierarchy of formulations much as was shown in Fig. 41 for the Navier-Stokes equations. It is amenable to Cartesian grids and associated algorithmic acceleration techniques. Additional details have been given by Chen and Doolen [94], 1998.

The LBM is a newer approach to solving aerodynamic flows as compared to continuum CFD methods. Promising simulations have been shown for complex flows such as transport undercarriage flows (Tomac et al. [95], 2016) and high-lift flows. A high-lift application is included in Section 3.2.2.2.

2.4.2. Consequences for concentrated vortex flow modelling and simulation

In this section we first incapsulate predictive requirements for concentrated vortex flows and then discuss implications for the use of modelling and simulation technologies to meet these simulation requirements. There are competing needs to be balanced between the extent of vortex flow physics represented in a simulation and the scope of conditions needed for scenario coverage. For example, high angle-of-attack maneuver conditions for combat aircraft can push the desired simulation technology to higher-physics (and more expensive) methods but the number of conditions requiring analysis can push the desired simulation technology to lower-physics (and less expensive) methods. These competing needs present a due diligence challenge for concentrated vortex flow simulation campaigns.

2.4.2.1. Concentrated vortex flow predictive requirements. The flow physics for concentrated vortex flows (Subsection 2.3) introduce several considerations for modelling and simulation of these flows. Flow physics that affect concentrated vortex flows occurs over a broad range of length scales. Smooth-surface separation occurs at sub-boundary-layer scales for the initiation of secondary vortices and, in certain cases, primary vortices. Secondary vortices occur on the order of several boundary layer thicknesses, and primary vortices occur on the order of wing scales. Within the primary vortex, the vortex core flow includes a boundary-layer-like structure with viscous length scale flow physics.

Concentrated vortex flows also present phenomenological challenges for modelling and simulation. These vortices can undergo abrupt state changes. One example is vortex breakdown, an abrupt state change from coherent to incoherent vorticity. Other examples include vortex interactions such as abrupt convective merging of corotating vortices or abrupt asymmetry onset of counterrotating vortices. Other (non-abrupt)

[6] Removal of the SGS filtering would result in a DNS formulation resolving all three regions.

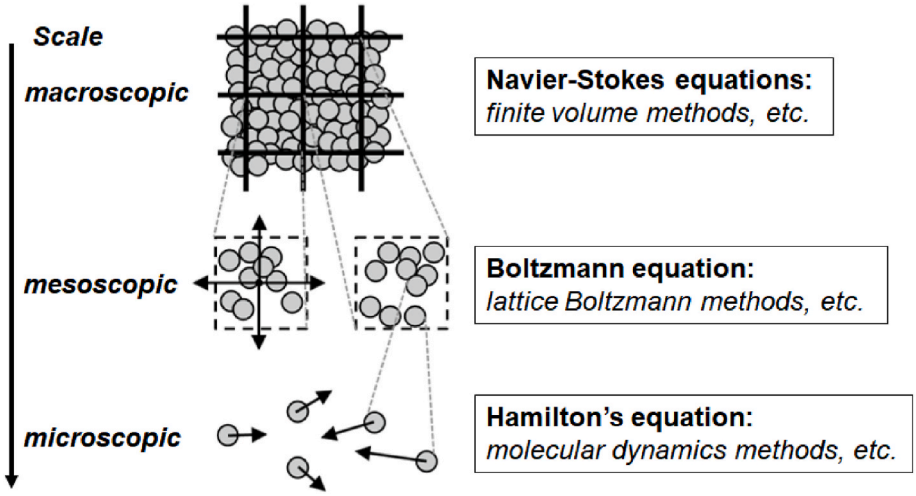

Fig. 52. Hierarchy of fluid dynamic modelling scales. Han and Ryozo [93], 2023.

phenomenological challenges include nonequilibrium boundary layer effects on smooth-surface separation for the formation of primary or secondary concentrated vortices. Vortex persistence application interests can invoke low-speed vortex-wake interactions as well as transonic vortex/shock/boundary-layer interactions.

Scenario considerations can result in significantly different Modelling and Simulation (M&S) requirements for concentrated vortex flow aerodynamic analysis. The nacelle strake application for commercial transports is basically designed for two scenarios, takeoff and landing. (See, Fig. 18.) This enables the application of the more advanced and expensive M&S technologies even when considering variations about the two target conditions that would be required for analysis.

Maneuvering aircraft, such as fighter aircraft and missiles, develop concentrated vortices for a broad portion of their overall flight envelope. This can result in tens to hundreds of thousands of conditions for which concentrated vortex flow aerodynamics contribute significantly to the vehicle performance. The requirement for such large numbers of analysis conditions is further discussed in Subsection 5.1. The more advanced and expensive M&S techniques can only be used sparingly withing this large flight envelope, and alternate strategies such as heterogenous formulaic computational databases or surrogate methods need to be employed.

2.4.2.2. Implications for the use of M&S technologies. Concepts and practices for physics-based M&S Verification and Validation (V&V) have become fairly well established (see Oberkampf and Roy [12]) and are continuing to mature. Concentrated vortex flows present several physics-based issues regarding M&S V&V. For example, the switch between the RANS and LES formulations of a hybrid RANS/LES method would need assessment as regards the scale of secondary vortices. Smooth-surface separation for primary and secondary vortices occurs in boundary layers that are three dimensional and may be in disequilibrium, and the modelling portion of WMLES methods would need focused assessments for these attributes. For LES, best practices are being developed for attached flows and are being explored for some separated flows such as occur near $C_{L,max}$ of a transport wing. Extension of these best practices to concentrated vortex flows has not been demonstrated yet.

Concentrated vortex flows also introduce additional considerations for the numerical model to converge to the physical model, i.e., grid convergence. As discussed in the physics subsections 2.3.1, the vortex core includes a region of inviscid but rotational flow as well as a viscous subcore with boundary-layer-like length scales. The primary vortex shear layer can exhibit vortical substructures related to Kelvin-Helmholtz instabilities. These vortex core and shear layer features introduce multiple length scales in the off-body flowfield that must be resolved as part of a solution verification process. One example is shown in Fig. 53 from Morton [96], originally published in 2003 [97]. Adaptive mesh refinement was used to resolve the concentrated leading-edge vortex flow physics, and a significant effect on the flow in the vortex core is shown. Concentrated vortex trajectories and flow details are determined as part of the solution process, and adaptive meshes, both in space and time, are necessary to capture them. Concentrated vortex flows increase the due diligence necessary for modelling and simulation verification and validation.

3. Presentation of survey findings

A summary of survey findings is presented in this section, first for fundamental vortical flow simulations, such as with delta wings, in Subsection 3.1 and then for more complex simulations motivated by configuration aerodynamics interests in Subsection 3.2. Results have been chosen to represent the present state of the art for the simulation of concentrated vortex flows; many other results can be found that are also of interest.

3.1. State of the art for fundamental vortical flow simulations

The presentation of survey findings for fundamental vortical flow simulations is organized into two parts based upon the degree of unsteadiness in the flow. As discussed in the flow physics manifestation Subsection 2.3.2, flows for which the unsteadiness is no larger than typical turbulence scales are referred to as steady flows and are summarized in Subsection 3.1.1. We consider these flows to have coherent vortices. Flows for which the unsteadiness is larger than typical turbulence scales are referred to as unsteady flows and are summarized in Subsection 3.1.2. We consider these flows to have semicoherent vortices and, in some cases, incoherent vorticity.

3.1.1. Steady flows

Fundamental manifestations of these vortical flows were reviewed in Subsection 2.3.2.1. Survey findings are first presented for sharp-edge separation studies. These are followed by smooth-surface separation studies.

3.1.1.1. Sharp-edge separation. The physics of sharp-edge separation for concentrated vortex flows that, for the most part, are steady (unsteadiness on the scale of turbulence) were reviewed in Subsection 2.3.1.1. This included primary leading-edge vortex separation and trailing-edge wake vortices. Basic manifestations of these vortex flows were

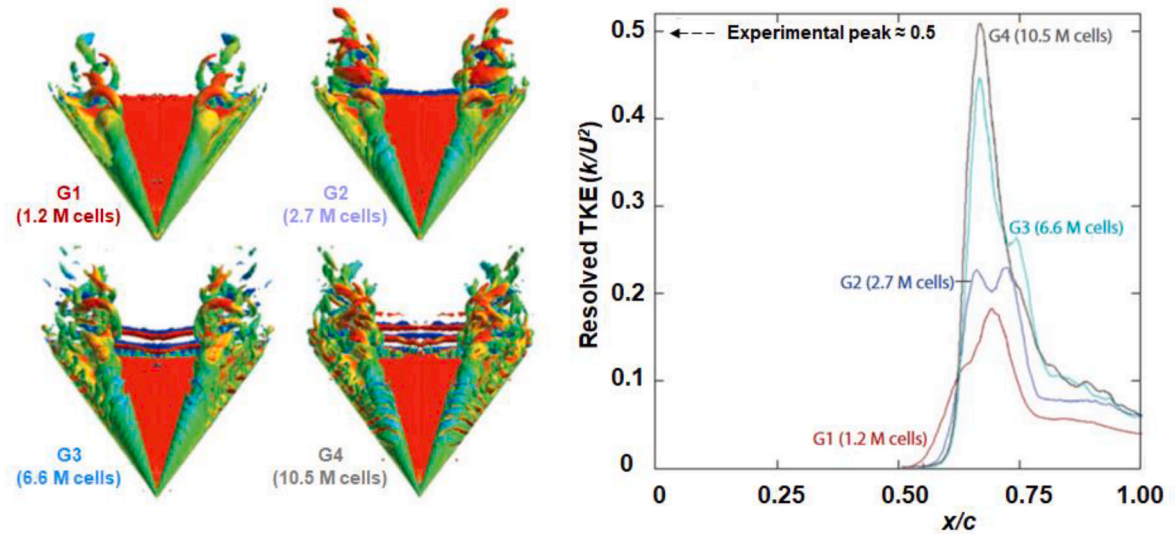

(a) Vortex resolution enhanced with AMR

(b) Resolved Turbulent Kinetic Energy (TKE)

Fig. 53. Grid resolution effect. Sharp-edged delta wing. Hybrid RANS/LES, Cobalt Solutions Cobalt code. $\Lambda_{le} = 70°$. $M = 0.07$, $Re_c = 1.56 \times 10^6$, $\alpha = 27°$. Morton [97], 2009.

summarized in Subsection 2.3.2.1. Recent findings for these topics follow.

Slender wings: Simulation of steady concentrated vortex flows from sharp leading edges was established in the mid-1980s with several emergent RANS formulations. As one example, Thomas et al. [99] demonstrated in 1987 good correlation with the Hummel $AR = 1$ delta wing data [4]. Simulations were for laminar flow using a thin-layer approximation, and good correlations between simulation and measurement were shown for surface pressures at one angle of attack as well as for lift coefficients over an angle-of-attack range up to high angles of attack. As such, only limited results were found in the present survey for what has become an established capability.

One recent example of this capability is shown in Fig. 54 from Schiavetta et al. [98]. At this condition, the concentrated leading-edge vortex is coherent; there is no vortex breakdown in the vicinity of the wing. All CFD simulations were performed with RANS methods that used different k-ω turbulence models. Experimental results came from NASA [40] and, overall, the correlations shown are quite good. Some degradation in the overall correlation with experiment is evidenced as the trailing edge is approached. The work served as a baseline for transonic research by Schiavetta as well as for a new research program on blunt leading-edge separation, Vortex Flow Experiment 2, to be described in Subsection 3.1.1.2.

We note that the experimental pressure distributions outboard of the primary vortex suction peak are relatively flat indicting a turbulent secondary vortex separation. The flow leading up to secondary separation likely has a nonequilibrium boundary layer, and the various two-equation k-ω turbulence models appear to have captured the secondary vortex flow well. Additional discussion of secondary vortex predictions is provided in Subsection 3.2.3.3 for simulations about the F-16XL aircraft.

Slender forebodies (chines): The authors found very few articles for concentrated vortex flow simulations from chined forebodies. Fundamental work, such as has been accomplished with the Hummel delta wing, seems warranted for chined forebody geometries that have become common for combat aircraft.

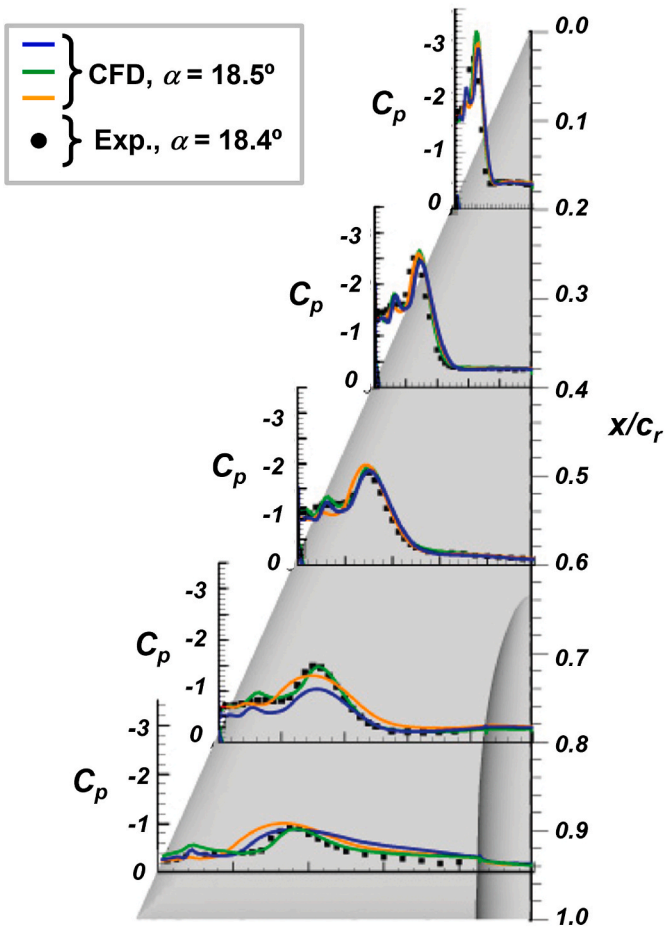

Fig. 54. Coherent leading-edge vortex, sharp-edged delta wing. RANS. $\Lambda_{le} = 65°$, $M = 0.4$, $Re_{mac} = 6 \times 10^6$. Schiavetta et al. [98], 2009.

3.1.1.2. Smooth-surface separation. The physics of smooth-surface separation for concentrated vortex flows that, for the most part, are steady

(unsteadiness on the scale of turbulence) were reviewed in Subsection 2.3.1.2 This included secondary vortex separation and blunt-leading-edge vortex separation. Basic manifestations of these vortex flows were summarized in Subsection 2.3.2.1. Recent findings for these two topics follow.

Secondary vortices: The secondary vortex is tightly coupled with the primary vortex, and details of secondary vortex separation can affect both the strength and the location of the primary vortex. One example has been given by Hummel for laminar vs turbulent secondary vortex separation as discussed in Subsection 2.3.1.2. Interactions between the secondary vortex and the primary vortex shear layer can also contribute to vortex shear layer instabilities, and an example is shown in Fig. 55 from Visbal and Gordnier [100] with contours of instantaneous axial vorticity. Simulations were performed with a high-order Navier-Stokes formulation for a semi-infinite delta wing with the Reynolds number based on the longitudinal distance L from the wing apex to the end of the simulation domain. This approach removed trailing-edge flow physics from the computational study. Results shown in Fig. 55 include the primary-vortex shear-layer interaction with the secondary vortex that contributes to the onset of shear-layer instability. Subsection 3.1.2.1 presents examples of concentrated vortex flows undergoing global unsteadiness.

The authors comment that, in the course of this review, little to no correlation between simulation and physical experiments was found for secondary vortex flow features. This seems to be a deficiency since the interaction effects between the primary and the secondary vortices can alter the primary vortex strength, location, and stability. Secondary separation can also be influenced by transition effects at wind tunnel Reynolds numbers that could be absent at flight Reynolds numbers.

Blunt-leading-edge separation: The NATO Research and Technology Organization (RTO) coordinated a research program in the 2000s, known as Vortex Flow Experiment 2 (VFE-2), to investigate blunt-leading-edge vortex separation [84]. The work focused on a 65° delta wing configuration that had been tested in the NASA Langley National Transonic Facility (NTF) in the 1990s as described by Luckring [101] to quantify Mach number, Reynolds number, and leading-edge bluntness effect on the leading-edge vortical separation, Fig. 56. The program objectives for VFE-2 have been described by Hummel [102] as part of a collective publication in 2013 of 8 articles in Aerospace Science and Technology [103]. Summary findings have been given by Luckring and Hummel [104].

One VFE-2 objective was to be able to predict with CFD the blunt-leading-edge vortex separation at select conditions. Early analysis (Luckring [105], Hummel [106]) led to the possibility of an additional inner primary vortex that occurred as part of the blunt-leading-edge vortex flow. Six experimental campaigns as well as extensive CFD studies were performed under VFE-2 to explore the properties of this newly identified inner vortex and to guide CFD assessments for the overall blunt-leading-edge vortical flow. The VFE-2 research confirmed the existence of the inner vortex and quantified features of this vortex. An example from Luckring and Hummel [104] is shown in Fig. 57. At these conditions, the origin of the leading-edge vortex is approximately halfway down the blunt leading edge. Data from new DLR experiments clearly show the inner primary vortex, and CFD simulations from the European Aeronautic Defense and Space Company (EADS) using the DLR TAU code indicate similar vortical structures. The EADS results demonstrated that the blunt-leading-edge vortex flowfield could be simulated with RANS technology, although correlation between the CFD predictions and experiment varied among the VFE-2 results. Little was established for the details of the incipient separation region that led to the blunt-leading-edge vortex flowfield.

A second fundamental research program on blunt-leading-edge vortical separation was conducted through the NATO Science and Technology Organization (STO) in the 2010s using a diamond wing [109]. The wing had 53° leading edge sweep with a NACA 64A0006 airfoil and was tested in the low-speed wind tunnel at the Technische Universität München (TUM), Fig. 58. The overall program has been described by Luckring et al. [107] as part of a collective publication in 2016 of 8 articles in Aerospace Science and Technology [110].

This wing was designed to isolate the onset and progression of blunt leading-edge vortical separation with angle of attack in such a way as to be relevant to a very complex suite of vortical flows that had been discovered on an Uninhabited Combat Air Vehicle (UCAV) configuration known as the Stability And Control CONfiguration, SACCON. In this regard, the diamond wing was considered as a unit problem for the more complex SACCON vortical flows. Some results from the SACCON research are included in Subsection 3.2.3.2. For the diamond wing, detailed experiments by Hövelmann first determined the effect of roughness on the blunt-leading-edge separation as part of his test technique [111], and then proceeded to quantify the onset and progression of turbulent blunt-leading-edge vortex separation with static and dynamic surface pressure measurements as well as mean and fluctuating off-body flowfield measurements, [112]. Extensive numerical studies were also performed covering a broad range of modelling and computational approaches.

Results from this diamond wing program successfully isolated the blunt-leading-edge vortex flow physics, and an example is shown in

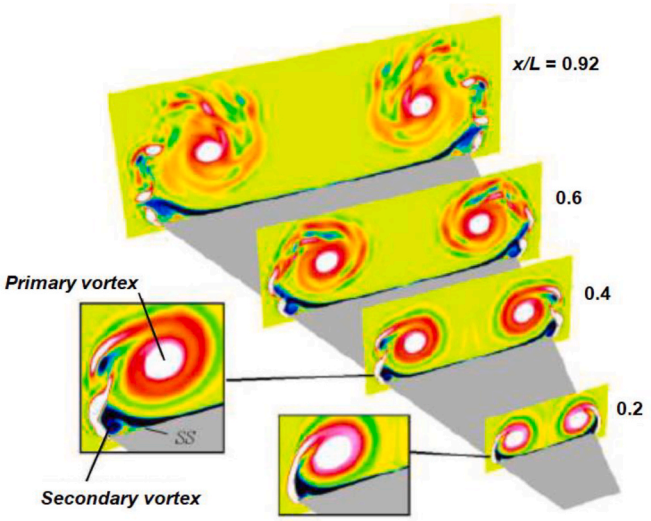

Fig. 55. Secondary vortex interactions. WRLES, AFRL FDL3DI code. $\Lambda_{le} = 75°$, $M = 0.1$, $Re_L = 25 \times 10^3$, $\alpha = 25°$. Visbal and Gordnier [100], 2003.

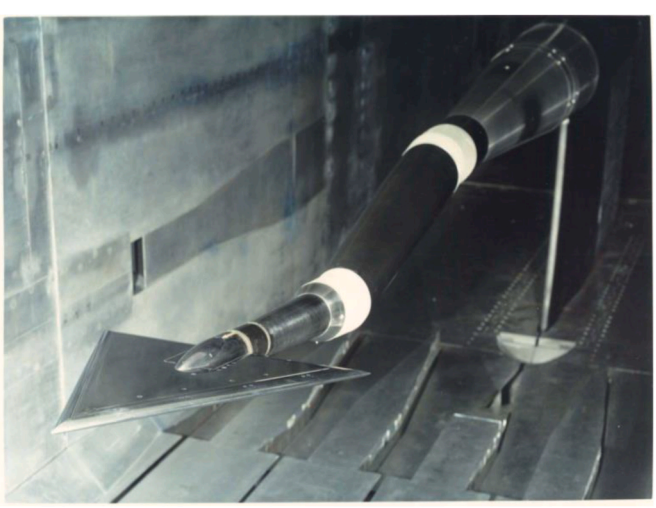

Fig. 56. NASA blunt-leading-edge delta wing model in NTF. $\Lambda_{le} = 65°$. [Photo: NASA, public domain].

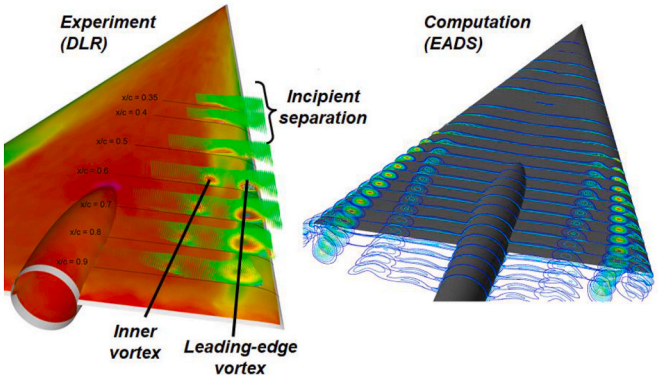

Fig. 57. Blunt-leading-edge vortex separation, delta wing. RANS, DLR TAU code. $\Lambda_{le} = 65°$, $M = 0.4$, $Re_{mac} = 6 \times 10^6$, $\alpha = 13.3°$. Luckring and Hummel [104], 2013.

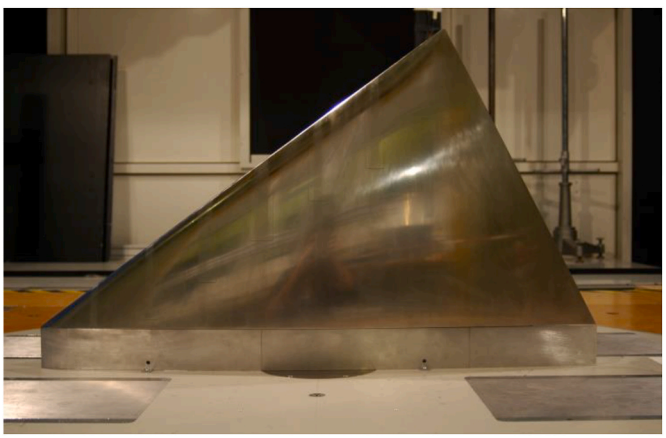

Fig. 58. Diamond wing model, $\Lambda_{le} = 53°$. Luckring et al. [107], 2016.

Fig. 59 from Frink et al. [108] using the NASA USM3D code. This simulation clearly shows the incipient separation region, the inner vortex, and the blunt-leading-edge vortex separation. Other simulations captured this same suite of vortical flow structures although the predicted location of the suite differed among the methods. The origin of the blunt-leading-edge vortex separation affects both the strength and the location of the vortices, and the overall flowfield was well predicted when this origin matched between experiment and simulation.

Although the diamond wing CFD results such as in Fig. 59 and Poll's wind tunnel investigations [44] are totally unconnected in time and the geometries are different, the overall flow patterns are remarkably similar and correlate nicely with the Polhamus phenomenological modelling [41] for the origin of the leading-edge vortex (Fig. 28).

Flowfield analysis for the diamond wing extended the understanding of the blunt leading-edge vortex separation. One example from Hitzel et al. [45] is shown in Fig. 60 as regards the formation of the inner vortex. Hitzel et al. observed that the upstream attached flow associated with the blunt leading edge would flow in the outboard direction over the inner portion of the wing, a common feature for slender wings, whereas the part-span blunt-leading-edge vortex would induce a reattached flow in the inboard direction. The collision of these two flows results in the inner primary vortex.

The origin of the inner vortex coincides closely with the origin of the blunt-leading-edge primary vortex. An example is shown in Fig. 61 from Deck and Luckring [113] using the ONERA ZDES code, a zonal hybrid RANS/LES formulation. In this figure, vortices are displayed by the Q criterion and are colored by the normalized streamwise velocity. A spanwise trace of total pressure loss is also shown downstream of the

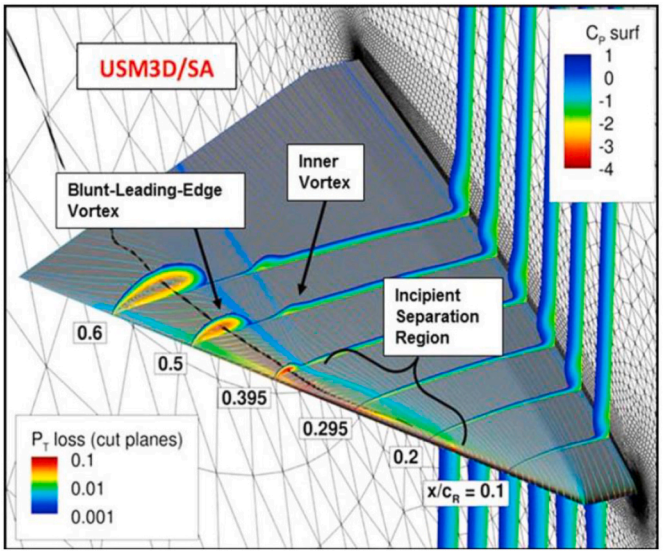

Fig. 59. Blunt-leading-edge vortex separation, diamond wing. RANS, NASA USM3D code. $\Lambda_{le} = 53°$, $M = 0.15$, $Re_{mac} = 2.7 \times 10^6$, $\alpha = 12°$. Frink et al. [108], 2016.

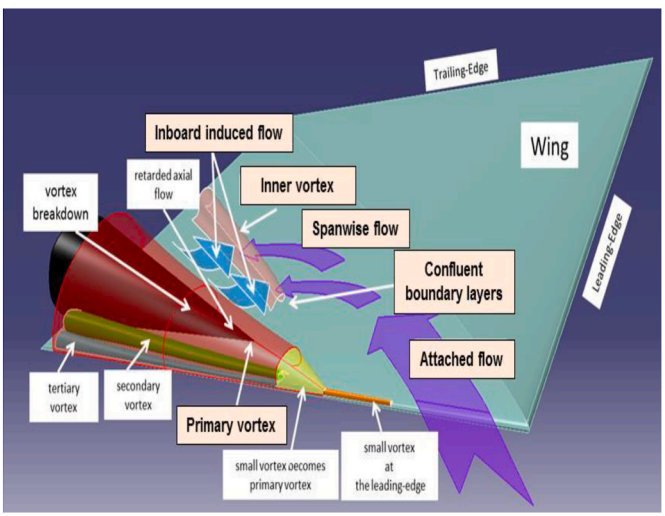

Fig. 60. Inner vortex separation. $\Lambda_{le} = 53°$, $M = 0.15$, $Re_{mac} = 2.7 \times 10^6$, $\alpha = 12°$. Modified from Hitzel et al. [45], 2016.

wing trailing edge. Compared to preceding RANS simulations, the unsteady content of the ZDES simulation did not fundamentally alter the overall vortex topology. Details of the primary and inner vortex origin become obscured where the incipient separation region would be anticipated.

Frink et al. [108] presented a detailed analysis of their simulation in the vicinity of the incipient separation region and the emergence of the blunt-leading-edge vortex, Fig. 62. This figure shows surface streamlines, static surface pressure distributions, and the pressure distribution along the leading edge. Extrapolation of the primary vortex reattachment line and the minimum suction pressure under the primary vortex coincides with the location of minimum leading-edge pressure coefficient, $C_{P,le}$, within the incipient separation region. The experimental minimum $C_{P,le}$ had been used by Luckring [39] as a criterion for approximating the location of the origin of blunt-leading-edge vortex separation, and the analysis from Frink et al. supports this approach. The blunt-leading-edge vortex separation initiates within the incipient separation region and downstream of the location for the beginning of the

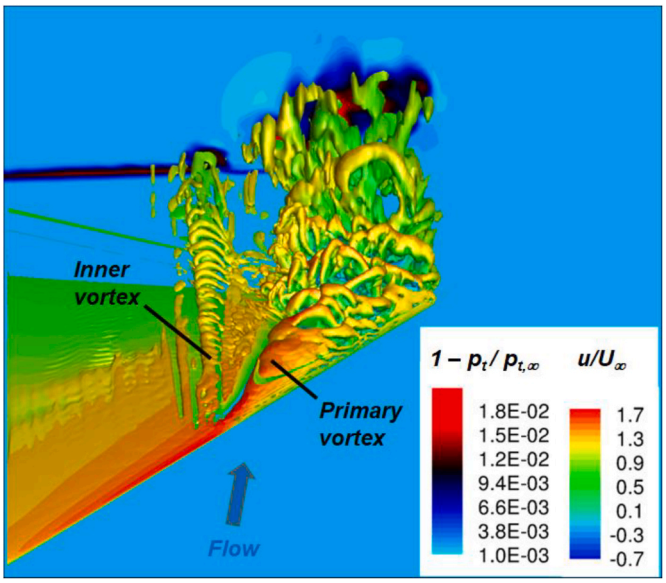

Fig. 61. Primary and inner vortices. Hybrid RANS/LES, ONERA ZDES code. $\Lambda_{le} = 53°$, $M = 0.15$, $Re_{mac} = 2.7 \times 10^6$, $\alpha = 12°$. Deck and Luckring [113], 2016.

incipient separation.

It can also be observed that the incipient separation region resembles the turbulent expanding long bubble separation discussed earlier from Polhamus with Fig. 28. The turbulent simulation shows a dividing streamline demarcating the recirculating incipient separation region from the adjacent attached flow, and all numerical results from the diamond wing project exhibited this general structure of the incipient separation region shown here. Although flowfield measurements were performed very close to the wing upper surface, few if any flow details could be measured within the incipient separation bubble.

The boundary layer state can affect the incipient leading-edge separation, and this was assessed by Buzica and Breitsamter [114] with new experiments and computations using the same 53° diamond wing. Experiments included fully turbulent leading-edge separation, using Hövelmann's test technique, as well as free transition leading-edge separation (i.e., testing without any forced transition). Computations were performed with the DLR TAU code for both fully turbulent and transitional flows. Results are shown in Fig. 63 for both fully turbulent

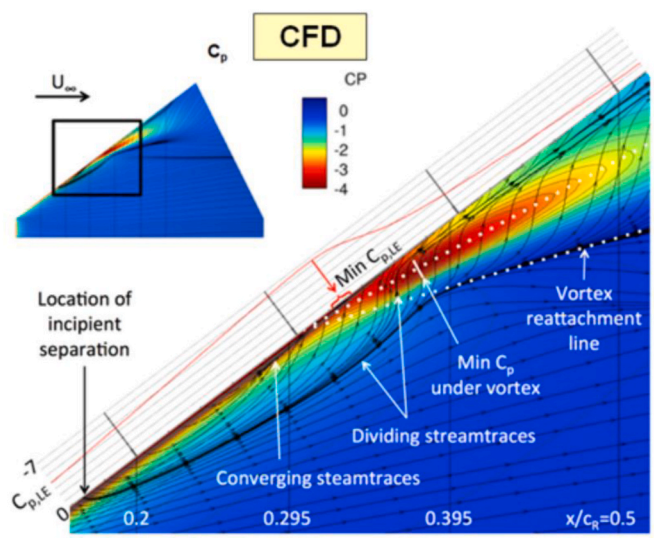

Fig. 62. Features of incipient separation region. RANS, NASA USM3D code. $\Lambda_{le} = 53°$, $M = 0.15$, $Re_{mac} = 2.7 \times 10^6$, $\alpha = 12°$. Frink et al. [108], 2016.

((a) and (b)) and transitional ((c) and (d)) flows. The fully turbulent results are very similar to those already discussed, showing the same suite of blunt-leading-edge vortex separation flow structures. The free transition results show further upstream leading-edge separation in association with laminar boundary-layer separation. It is noted that the same suite of blunt-leading-edge vortex separation phenomena (incipient separation, blunt-leading-edge primary and secondary vortices, inner vortex) have collectively shifted upstream. In addition, a laminar separation bubble was found upstream of the incipient separation. Correlations between experiment and CFD were reasonable.

Buzica and Breitsamter provided additional numerical analysis of the laminar separation near the leading edge, and an example of their work is shown in Fig. 64 for boundary layer intermittency and turbulent kinetic energy. The flow about the leading edge shows a laminar separation bubble followed by turbulent reattachment, one of the standard leading-edge separation classifications as discussed by Polhamus [41]. (See, Fig. 28.) These results demonstrate the importance of tripping the leading-edge flow to approximate fully turbulent separation at subscale Reynolds number conditions common to most wind tunnel testing.

A new structure of blunt-leading-edge vortex separation has been established from these research projects enabled by the NATO STO. This structure includes an incipient separation region leading to the onset of primary vortical separation and an inner corotating vortex. The findings have been achieved through multiple wind tunnel tests as well as numerous RANS and hybrid RANS/LES simulations.

Computational analysis is always constrained by the subset of physics represented within the method being used (e.g., a RANS formulation with a particular turbulence model). Advanced modelling can produce advanced physics simulation capability but at increased computational expense. Further blunt-leading-edge separation assessments were performed with the AFRL high-order wall-resolved LES code FDL3DI [66] for an aspect ratio $AR = 4$ constant-chord wing with an NACA 0012 section and with three sweep values, $\Lambda = 0°$, 15°, and 30°. Flow conditions were $M = 0.1$, $Re_c = 0.2 \times 10^6$, and included both sinusoidal pitch oscillations as well as stationary angle of attack simulations.

Fig. 65(a) shows an instantaneous image of the unsteady flow in terms of off-body vorticity magnitude isosurfaces and surface pressure coefficients for the 30° swept wing, at a stationary angle of attack $\alpha = 12°$. Examination of this flowfield indicated that there was a region of laminar flow near the wing centerline (denoted as '1' in Fig. 65). which increases in extent with sweep angle. For most of the span, however, the wing exhibited a well-defined laminar separation bubble followed by turbulent reattachment. Their simulations also captured laminar separation bubble bursting with subsequent dynamic wing stall effects. These high-fidelity physical modelling simulations indicated the role that transitional flow plays in these smooth-surface separated flows. The simulations also captured a smooth-surface side-edge concentrated vortex flow. Fig. 65(b) shows an instantaneous isosurface image of off-body streamwise reversed flow at an angle of attack $\alpha = 21.3°$. At this angle of attack, the separation has taken on a vortical structure. These wall-resolved LES simulations appear to be capturing a progression from laminar separation bubbles and transition flow physics at low angles of attack to a leading-edge vortical separation at higher angles of attack, consistent with the flow interpretations of Polhamus [41] as shown in Fig. 28.

Higher-order wall-resolved LES simulations have also contributed understanding for compressible flow physics effects for blunt-leading-edge separation. An example is shown in Fig. 66 from Benton and Visbal [116] using the AFRL FDL3DI code. Simulations were performed for an NACA 0012 airfoil at a chord Reynolds number $Re_c = 1 \times 10^6$ for a range of Mach numbers and angles of attack. The research addressed dynamic stall effects for the airfoil, and the simulations required 267 $\times$ 10^6 nodes.

The results are shown for $M = 0.4$ and a fixed angle of attack $\alpha = 13.1°$ in Fig. 66. A sonic surface forms near the leading edge resulting in a

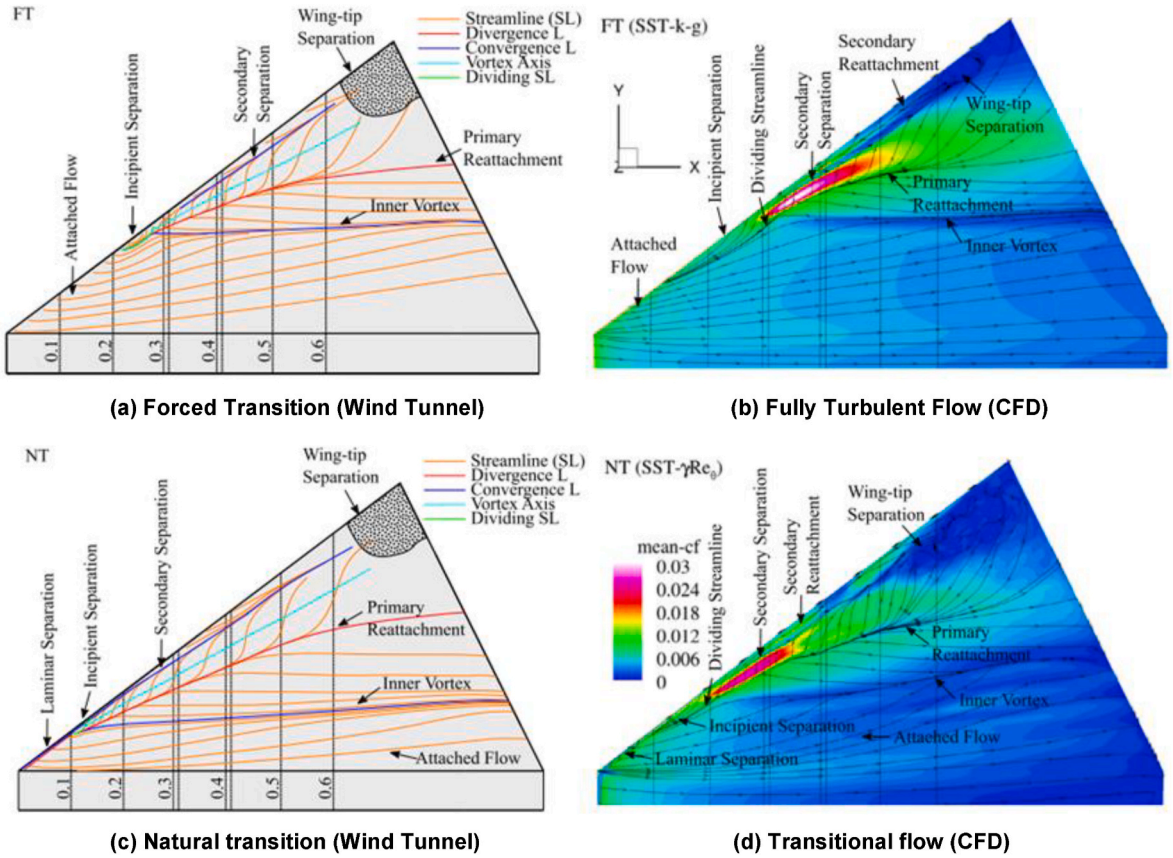

Fig. 63. Laminar vs. turbulent blunt-leading-edge vortex separation. TUM wind tunnel, RANS DLR TAU code. $\Lambda_{le} = 53°$, $M = 0.15$, $Re_{mac} = 2.7 \times 10^6$, $\alpha = 12°$. Buzica and Breitsamter [114], 2019.

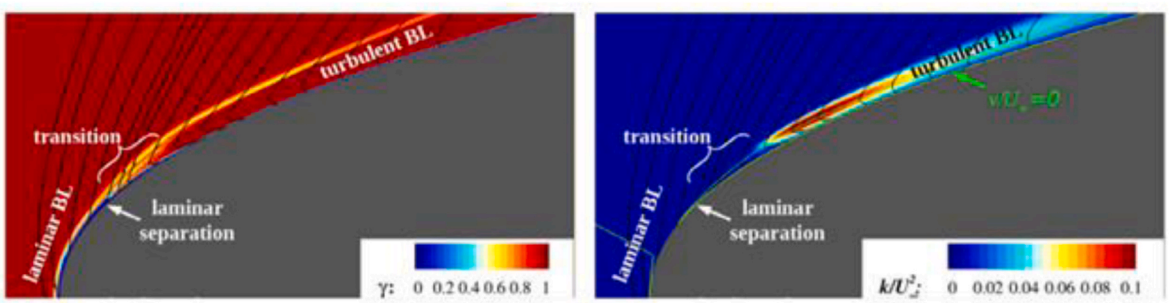

Fig. 64. Spanwise variation of intermittency and relative turbulent kinetic energy, $x/c_R = 0.1$. RANS, SST-γ Re_θ, DLR TAU code. $\Lambda_{le} = 53°$, $M = 0.15$, $Re_{mac} = 2.7 \times 10^6$, $\alpha = 12°$. Buzica and Breitsamter [114], 2019.

shock-induced separation as indicated by the q-criterion images in Fig. 66 (a). Details of the leading-edge flow structure within the sonic surface are shown in Fig. 66(b) using the pressure gradient magnitude. For this image, flow properties have been averaged in the spanwise direction. The simulation has captured a succession of shocks and expansions leading to the terminal shock and shock-induced boundary-layer separation. The full succession of shocks would be affecting the boundary layer leading up to the terminal shock boundary-layer interaction. An increase in freestream Mach number would strengthen this shock train and most likely promote separation. It would be instructive to know how well these flow details could be captured with less costly reduced physics methods.

These high-order wall-resolved LES results appear to capture a suite of plausible flow physics for blunt leading edge vortex separation that are not modeled, or have not been reported, in the current RANS and hybrid RANS/LES simulations found in this review.

An assessment of compressibility effects on blunt-leading-edge vortical separation for a swept constant-chord $AR = 4.8$ wing was included in the studies by Schütte [117] in 2017, and one result is shown in Fig. 67 for $\Lambda = 53°$ and $\alpha = 11°$ using off-body streamlines and upper surface isobar contours. The wing has no twist or camber and a constant NACA 64A-005 airfoil section. An increase in Mach number from 0.3 to 0.4 changed the wing flow from attached to a separation-induced vortex flow, and further increases in Mach number promoted this leading-edge separation (i.e., it occurs closer to the wing apex). This trend is consistent with simple sweep theory in association with the spanwise variation of upwash. Similar trends were shown in Luckring's analysis [39] of the 65° delta wing. Schütte's work was performed at a high Reynolds number $Re_c = 52.6 \times 10^6$ and included systematic assessments for

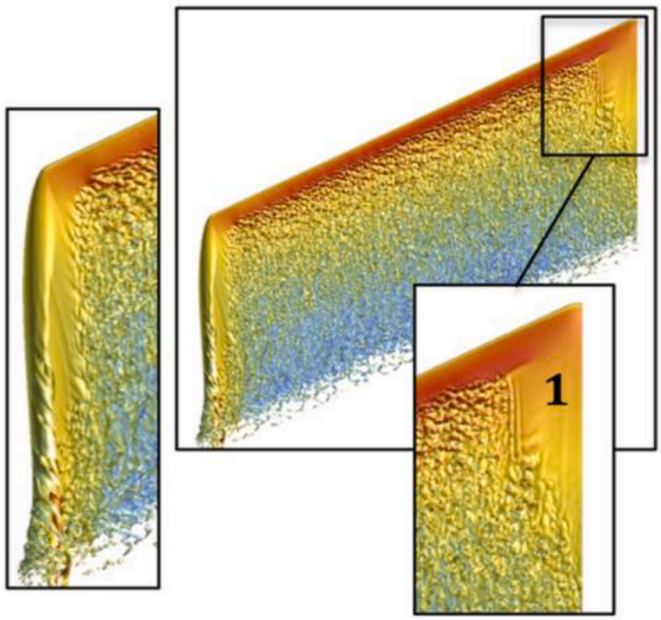

a) $\alpha = 12°$

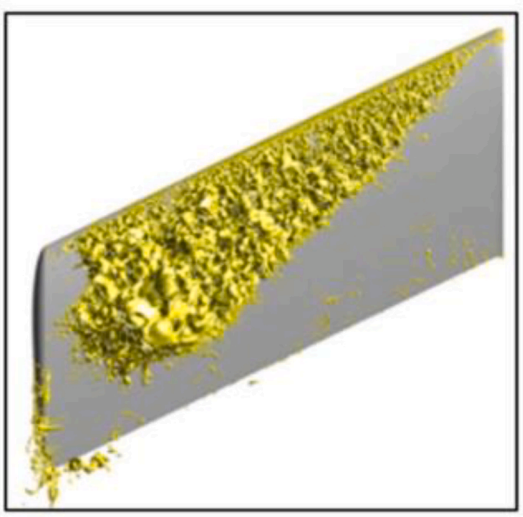

b) $\alpha = 21.3°$

Fig. 65. High-fidelity wall-resolved LES simulation, AFRL FDL3DI code. $AR = 4$, $\Lambda_{le} = 30°$, $r_{le}/c = 1.58\%$, $M = 0.1$, $Re_c = 0.2 \times 10^6$. Visbal and Garmann [115], 2019.

leading-edge sweep and leading-edge bluntness effects.

Blunt-body separation: Blunt-body separation can be important for both fore-body and aft-body flows. Although combat aircraft have adopted chined forebodies, many missiles still have smooth forebodies for which smooth surface separation is important both as regards fore-body forces and moments as well as regards interaction effects of the forebody separated flows with downstream components. Aft-body smooth-surface separation is important for transport drag and for cargo deployment.

One example of aft-body concentrated vortex flow simulation has been given by Garmann and Visball [118] in 2019. Simulations were performed on a simplified configuration representative of a C-130 aft body geometry. Computations were performed with the AFRL high-order LES solver FDL3DI at $M = 0.1$, $Re_D = 0.2 \times 10^6$, and $\alpha = 0°$, and results are shown in Fig. 68 for contours of nondimensional entropy.

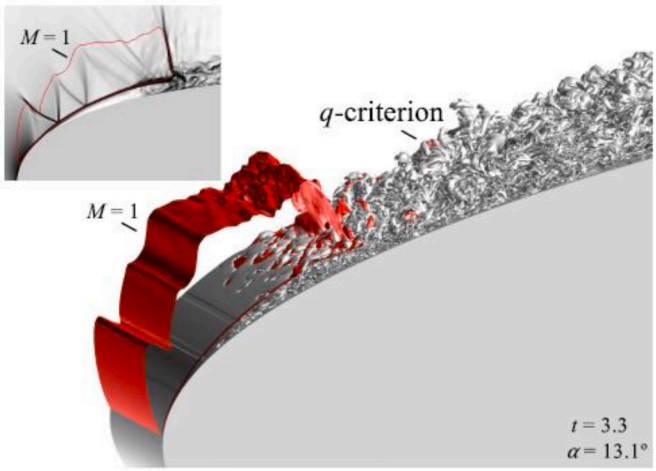

a) Leading-edge flow structure

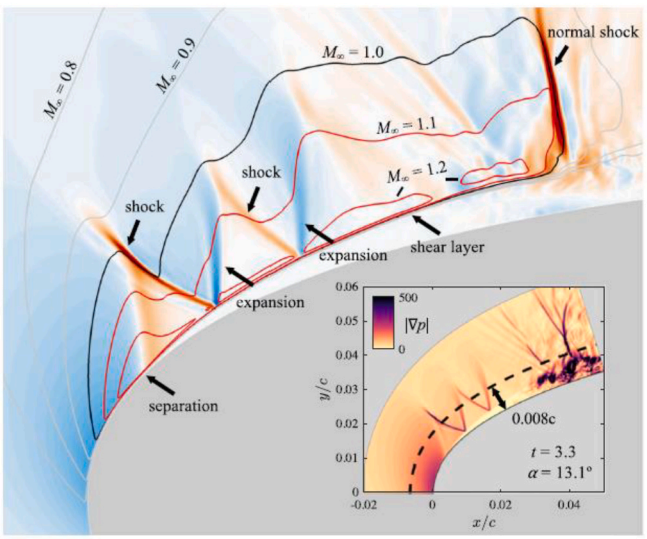

b) Span-averaged flowfield details near leading edge

Fig. 66. Compressibility effect on leading-edge separation. WRLES, AFRL FDL3DI code. NACA 0012 airfoil, $M = 0.4$, $Re_c = 1 \times 10^6$. $\alpha = 13.1°$. Benton and Visbal [116], 2020.

Two grids were examined, 77×10^6 and 210×10^6 nodes, and the results of Fig. 68 are for the finer grid. Simulations are time accurate, but, in this case, the instantaneous flowfield is very similar to the time-averaged flowfield. The body vortices are well resolved including downstream persistence. The effects of these concentrated body vortices could be important to cargo deployment since they induce a flow toward the body. The conditions for this study matched a fundamental experiment by Bulathsinghala et al. [119], and correlations with the available measurements was reported to be extremely good.

We can consider the resource requirements for this simulation to be performed at full-scale Reynolds number using the LES study of Larsson et al. [87] that was summarized in Table 1. At an altitude of 10×10^3 feet and $M = 0.1$, the full-scale Reynolds number based on fuselage diameter[7] for the C-130 is estimated to be $Re_D = 7.4 \times 10^6$ and the simulations of Fig. 68 at this Reynolds number would require approximately 143 billion nodes. Refinements to this estimate could account for

[7] The corresponding Reynolds number based upon fuselage length would be approximately $Re_L = 52.3 \times 10^6$.

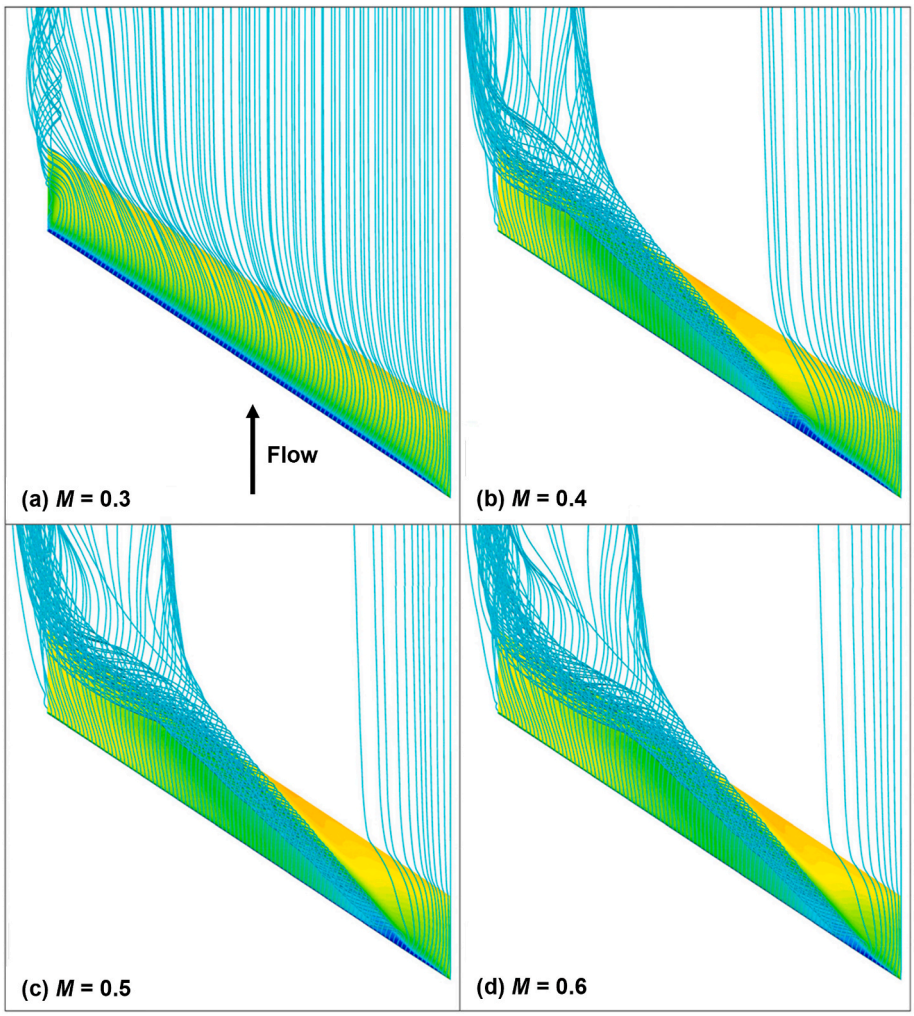

Fig. 67. Mach effect on blunt-leading-edge vortex separation. RANS, DLR TAU code. $\Lambda_{le} = 53°$, $r_N = 0.003$, $Re_{cref\infty} = 52.6 \times 10^6$, $\alpha = 11°$. Schütte [117], 2017.

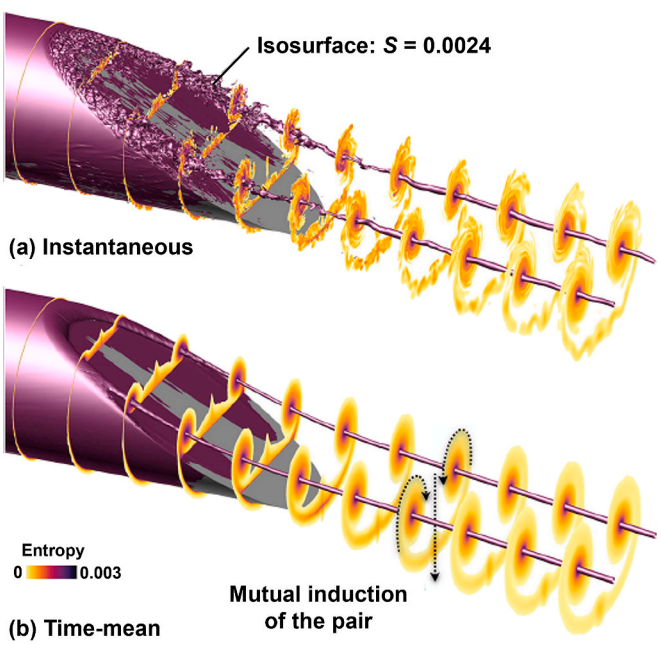

Fig. 68. Blunt-surface after body vortex flow. WRLES, AFRL FDL3DI code. $M = 0.1$, $Re_D = 0.2 \times 10^6$, $\alpha = 0°$. Garmann and Visbal [118], 2019.

scaling effects unique to the concentrated vortices shown in the Garmann and Visbal work. Inclusion of the vehicle empennage, at least the horizontal tail plane, could be important to characterizing the cargo deployment flowfield and would significantly increase this problem size.

3.1.2. *Unsteady flows*

Fundamental components of concentrated vortex flows from Subsection 2.3.1 can also have unsteady flow manifestations where, for the most part, the unsteadiness occurs on a scales that are greater than that of turbulence. These manifestations were reviewed in Subsection 2.3.2.2. In some cases, the unsteadiness can be manifested locally, such as for vortex breakdown or vortex hysteresis. In other cases, the unsteadiness can be manifested globally, such as for the entire primary vortex. Recent findings for these topics follow.

3.1.2.1. Steady configuration. Summary findings are presented first for local unsteadiness, such as vortex breakdown, and then for global unsteadiness, such as shear-layer instabilities, over not-so-slender wings.

Local unsteadiness: Studies of vortex breakdown in tubes has continued to provide detailed insights of these flowfields. The experimental apparatus enables detailed measurements within the bursting vortex, and this simplified bounding geometry also enables complex simulations of high resolution in the bursting vortex. A comprehensive review article was given in 2001 by Lucca-Negro and O'Doherty [121] that covers 45 years of experimental, computational, and theoretical vortex breakdown research in tubes. Multiple modes of vortex

breakdown continue to be identified experimentally (Sorensen et al. [122]) and an example of detailed flow measurement through the core of a vortex is shown in Fig. 69 from Novak and Sarpkaya [120]. Such detailed measurements are difficult at best to accomplish for wing vortex flows.

In 2009 Zhang et al. [123] studied the topological structure of shock-induced vortex breakdown. The study focused on cylindrical geometry but allowed for three-dimensional flow. Solutions were obtained from Direct Numerical Simulation of the full Navier-Stokes equations. One example solution is shown in Fig. 70. DNS captures many complexities of the flow within the breakdown bubble.

Complex flow simulations as well as detailed flowfield measurements are tractable for the vortex breakdown flows in tubes. This seems to be a useful forum to perform validation testing campaigns pertinent to vortex breakdown.

Many vortex breakdown studies are motivated by wing aerodynamics, and here we summarize select results, often for delta wings, for subsonic flows and then for compressible flows. Fundamental theory and studies such as those just discussed can relate to delta wing vortex flows, and one example has been given by Rusak and Lamb [124] in 1999. An axisymmetric vortex model from vortex tube research by Wang and Ruzak [125] was coupled with vortex flowfield measurements at unburst conditions and was shown to predict the onset of vortex breakdown at higher angles of attack. In a 2009 study, Jones et al. [126] used vortex breakdown criteria derived from vortex tube research to analyze and predict vortex breakdown over a 76° delta wing. This work demonstrates a connectivity of vortex flow physics studies, such those mentioned immediately above, with delta wing vortex flows. It is possible that other advancements in vortex breakdown modelling and simulation could benefit from coupled studies. For example, modelling and simulation validation studies could be performed in the vortex tube

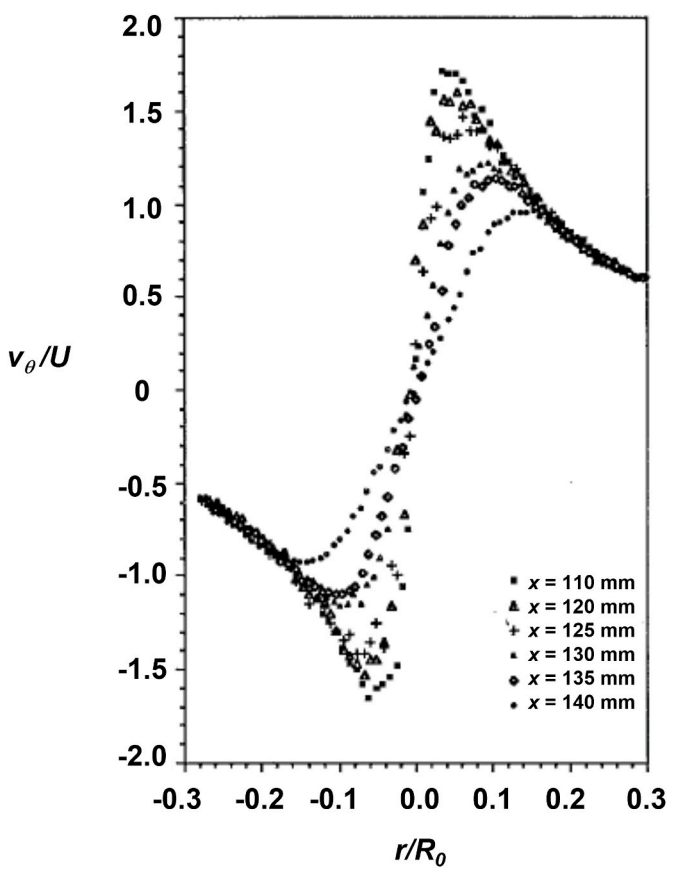

Fig. 69. Swirl velocity measurements through a vortex core. Novak and Sarpkaya [120], 2000.

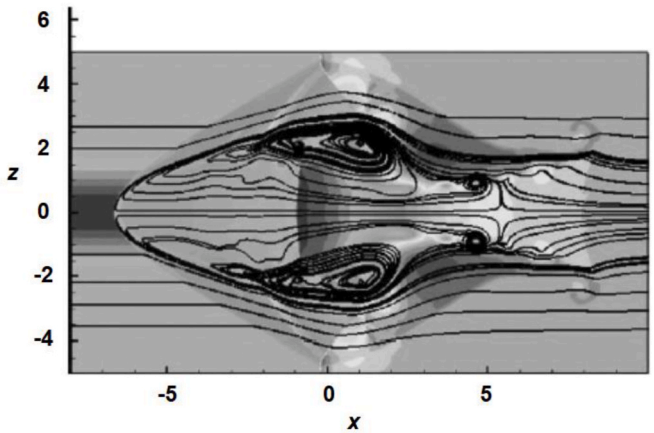

Fig. 70. Vortex breakdown bubble. DNS simulation. Zhang et al. [123], 2009.

with a view to transference of the results to delta wing applications.

With regard to wing studies, an extensive vortex breakdown project for the 70° delta wing was performed in the NATO Task Group AVT-080 in the early 2000s and reported in 2009 [127]. Physical data came from recent detailed experiments by Mitchell that have been summarized in 2000 [128] and in 2003 [129]. Many codes were used to simulate these data, and the most promising vortex breakdown predictions came from hybrid RANS-LES formulations. One example was given by Morton [96]. in 2009. The simulations used a Detached Eddy Simulation (DES) approach coupled with the SA turbulence model. Morton quantified the importance of grid resolution for the offbody vortical flows and demonstrated good correlation with experiment by using adaptive mesh refinement (AMR) for vortex breakdown. This NATO Task Group accomplished a significant body of work, and this has resulted in further assessments beyond the NATO project. One example was given by Son et al. [130] in 2015 for DDES assessments and others can be found.

Before advancing to higher-speed flows with vortex breakdown, it is important to recall that vortex breakdown can exhibit asymmetry between left and right semispans as well as a dynamic antisymmetry as the breakdown locations oscillate out of phase between the semispans. These features have been demonstrated experimentally by Lambourne and Bryer [53] (1962) and Shen and Wen [131] (2018) among others. Computational vortex breakdown assessments could thus require full-span simulations to allow for these asymmetric effects. One example has been given by Nonomura et al. [132] in 2013 with hybrid RANS/LES simulations for the NATO 70° delta wing. The results of Fig. 71 show the time evolution of asymmetric vortex breakdown at a compressible freestream Mach number $M = 0.6$.

At low speeds, the axial flow in the vortex care can achieve three times freestream value, and compressibility can have significant effects on the vortex core flow and influence vortex breakdown, even at freestream conditions considered to be incompressible. Compressibility assessments are included in the Nonomura study [132]. At higher speeds shocks can form and introduce a new mechanism, shock-vortex interaction, to induce vortex breakdown. Schiavetta et al. [98] assessed transonic shock-vortex interactions including shock-induced vortex breakdown for the 65° delta wing used for Vortex Flow Experiment 2. Unsteady RANS simulations showed reasonable correlation with earlier measurements with this wing (Luckring [101]). A review of supersonic shock-vortex interactions regarding vortex breakdown has been given by Kalkhoran and Smart [133] in 2000, and a family of supersonic shock-vortex interaction topologies were established by Miller and Wood [49] in 1984. These reports identify many classes of shock-vortex interactions and present a challenge for computational technology not only to simulate the shock-vortex interaction flows within each domain but also for predicting state changes across the domains.

Global unsteadiness: Globally unsteady vortex flow physics was

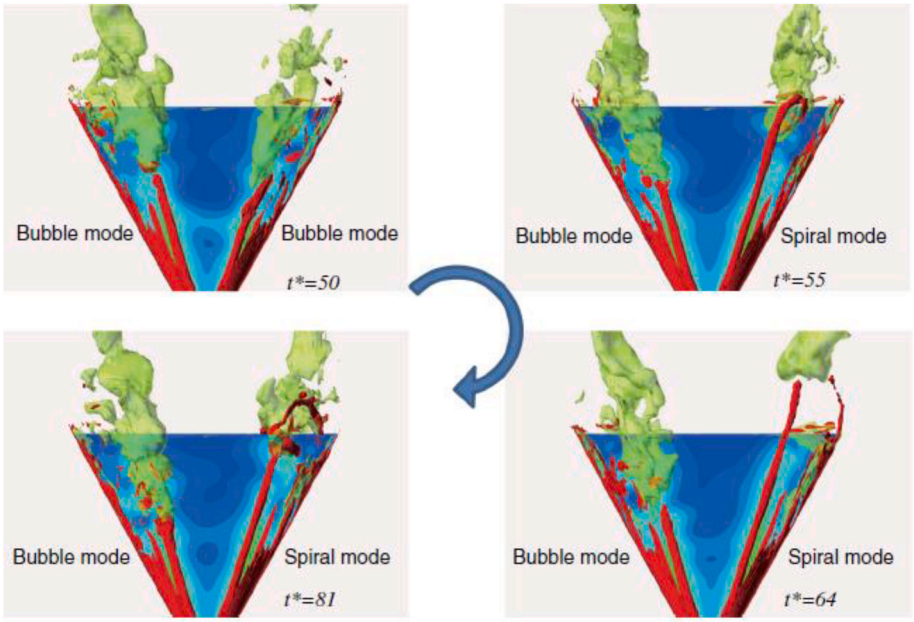

Fig. 71. Transient asymmetric vortex breakdown. Hybrid RANS/LES. $\Lambda_{le} = 70°$, $M = 0.6$, $Re_{cr} = 1.56 \times 10^6$, $\alpha = 30°$. Nonomura et al. [132], 2013.

included in Subsection 2.3.2.2 discussions. Sources for these phenomena include vortex wandering, vortex breakdown, and shear layer instabilities among others. Usually, these flow phenomena will interact with each other in a complex unsteady fashion. With respect to nonslender delta wings, even at moderate angles of attack, the leeward side can be dominated by separated and vortical flows that can be unsteady. The following paragraphs discuss the effects that sweep and Reynolds number play on global unsteadiness. Highly swept wings are discussed first, followed by moderately swept (nonslender) wings.

Gursul [70] reviewed unsteady flow phenomena over slender (i.e., highly swept) delta wings at high incidence in 1994. The shear layer shed from the leading edge of a delta wing is subject to the unsteady Kelvin–Helmholtz instability that is a generic contributor to the unsteadiness of concentrated vortex flow.

Visbal and Gordnier [100] have studied the vortex dynamics in the flow over a 75° semi-infinite sharp swept leading edge at an angle of attach of 25° and a range of Reynolds numbers using a high-order implicit Large Eddy Simulation (ILES) code. They selected this configuration to isolate the shear-layer dynamics from disturbances from trailing-edge separation or vortex breakdown, which can take place on a finite wing. As shown by the computed instantaneous isosurfaces of axial vorticity in Fig. 72, beyond a critical value of Reynolds number, unsteady substructures appear in the shear layer above the wing, and their origin moves closer to the apex with increasing Reynolds number.

They attribute the onset of these unsteady phenomena to unsteady separation of the boundary layer over the upper wing surface with subsequent vorticity infusion. Fig. 73(a) distinguishes three separate regions in the streamwise evolution of the feeding sheet with instantaneous axial vorticity isosurfaces. In Region I the shear layer is smooth, without substructure, and steady. Near their onset, the shear-layer substructures are very coherent, Region II, but further downstream, Region III, they undergo a process of secondary instability along their axes and breakup into discrete concentrations of vorticity, stretched and convected in helical paths around the primary vortex. We would refer to Region III as a semicoherent concentrated vortex.

Fig. 73(b) shows instantaneous vorticity magnitude contours in crossflow planes and a longitudinal plane through the vortex core. For $x/L > 0.4$, the boundary-layer separation is unsteady with secondary vorticity interacting with it, similar to the case described earlier regarding secondary vortices (see Fig. 55). Characterized by discrete and fairly organized substructures, the feeding sheet in Region II rotates around the core. The shear-layer structure becomes progressively more complex in Region III as the substructures shed from the leading edge become susceptible to further instabilities along their axes. Visbal and Gordnier [100] state that the vortex core remains distinct at all times but exhibits significant unsteadiness in the form of lateral vortex wandering

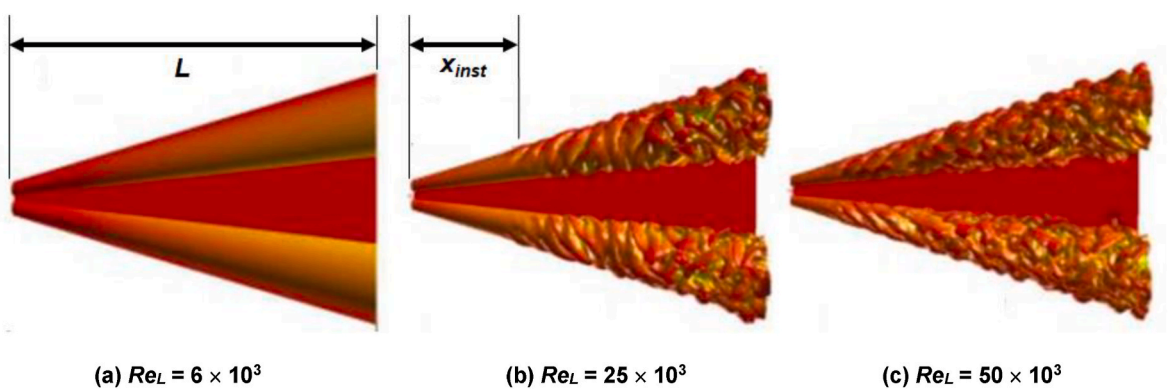

Fig. 72. Evolution of shear-layer structures with increasing Reynolds number. WRLES, AFRL FDL3DI code. $\Lambda_{le} = 75°$, $M = 0.1$, $\alpha = 25°$, Visbal and Gordnier [100], 2003.

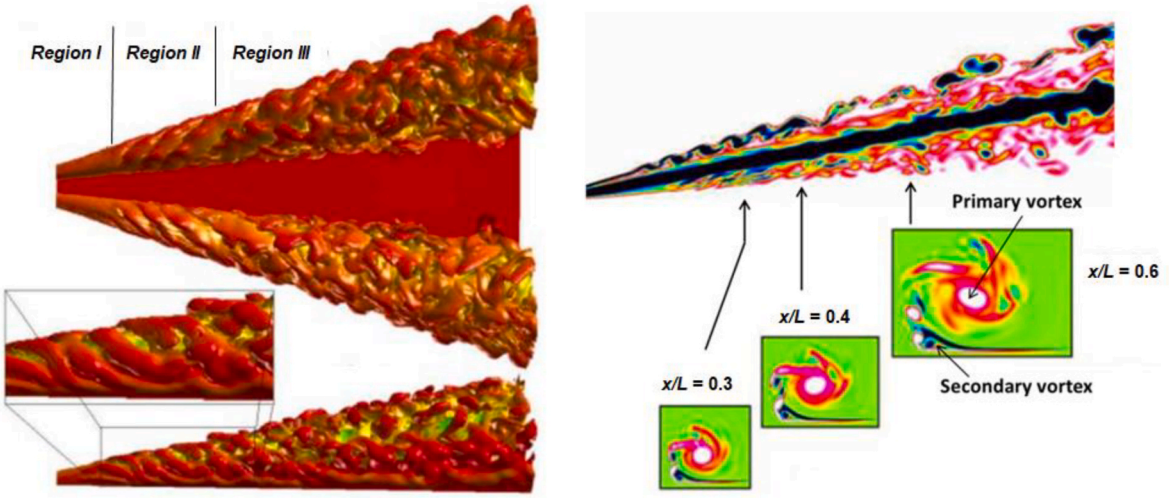

(a) Instantaneous axial vorticity isosurfaces (b) Instantaneous vorticity magnitude contours

Fig. 73. Shear-layer dynamics and substructure growth. WRLES, AFRL FDL3DI code. $\Lambda_{le} = 75°$, $M = 0.1$, $Re_L = 50 \times 10^3$, $\alpha = 25°$. Visbal and Gordnier [100], 2003.

as well as undulations that propagate downstream along its axis.

Gursul et al. [65] and Gordnier and Visbal [134] studied moderate-sweep delta wings (e.g., $\Lambda_{le} = 50°$) and found that even though the maximum lift coefficient and stall angle of nonslender deltas are lower than those with higher sweep, their aerodynamic performance is preferable at low to moderate angles of attack. Furthermore, the Reynolds number has strong influence on the vortical flows developing over moderately swept wings (Gordnier and Visbal [134], Gursul [135]) and promotes vortex breakdown followed by the disappearance of an organized primary vortex. Another distinct feature is that there exists a weaker second vortex which has the same sign of vorticity as the primary vortex and emerges in the separated shear layer outboard of the primary vortex, leading to a so-called dual primary vortex system at low angles of attack ([64,134–137]).

Visbal and Gordnier [100] have studied the effect that sweep plays in the vortex dynamics over a 50° sharp delta wing for angle of attack $\alpha = 15°$ and Reynolds number $Re_L = 26 \times 10^3$ using a high-order implicit (ILES) code. With vortex breakdown occurring over the wing, the unsteady vortical flow exhibited several distinct phenomena. The flow upstream of vortex breakdown is characterized by the formation and shedding of vortical substructures in the shear layer that emanates from the leading edge. Accompanying this shear-layer instability is an eruptive response of the secondary flow resulting from the interaction of the primary vortex with the surface boundary layer.

Instantaneous isosurfaces of axial vorticity colored by the level of the stagnation pressure visualize this unsteady flow in Fig. 74(a). These shear-layer features surround a distinct vortex core visible interior to the shear layer at upstream locations (Fig. 74(a)). Downstream, this distinct vortex system breaks up into a collection of very fine-scale structures. But for this low sweep angle, the vortex core does not exhibit the distinct spiral winding normally present in vortex breakdown for higher sweep angles.

The onset of breakdown is less abrupt than that observed over slender delta wings, with the breakdown region having a more conical shape, Fig. 74(b). These breakdown features make it more difficult to define a specific location for the vortex breakdown point. A transition from jet-like to wake-like flow does occur in the vortex core with the corresponding switch in sign of azimuthal vorticity. No actual flow

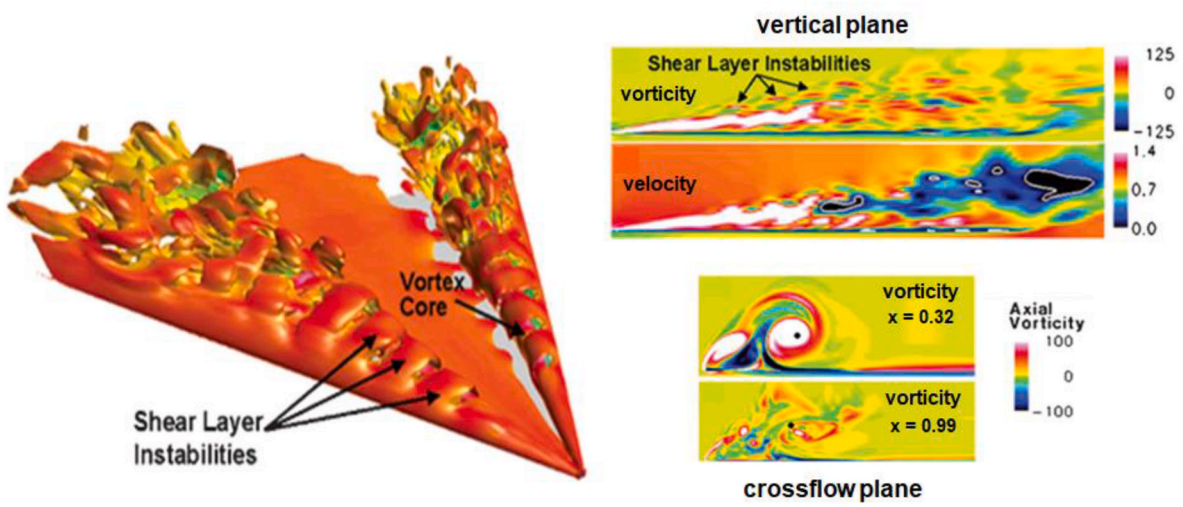

(a) Instantaneous axial vorticity isosurfaces (b) Instantaneous axial contours

Fig. 74. Instantaneous vortex structure. WRLES, AFRL FDL3DI code. $\Lambda_{le} = 50°$ (sharp), $M = 0.1$, $Re_L = 26 \times 10^3$, $\alpha = 15°$. Visbal and Gordnier [100], 2005.

reversal is observed in the mean flow, despite isolated pockets of reversed axial flow being present in the instantaneous flow.

Upstream of breakdown, Gordnier and Visbal [134] observed a periodic wandering of the vortex core around a mean location, which results from the formation and shedding of vortical structures in the shear layer emanating from the leading edge of the delta wing and from the eruptive response of the secondary flow resulting from the interaction of the primary vortex with the surface boundary layer.

Downstream of vortex breakdown, the coherent vortex core disintegrates into many finer-scale, unsteady flow features. The typical spiral winding observed for higher sweep wings is absent. The breakdown of the coherent vortex core into finer scales is also evident in the plane normal to the vortex core $x = 0.99$ (Fig. 74(b), crossflow plane). At this location, the whole vortex system has broken down into many small, highly unsteady flow features.

3.1.2.2. Unsteady configuration. Summary findings are presented for unsteady flows in association with configuration motions. All these survey findings are for delta wings in ramp-up and pitch oscillations. The physics of unsteady vortex flows from unsteady boundary conditions was included in Subsection 2.3.2.2.

The effect of a ramp increase in angle of attack from 25° to 50° on transient vortex breakdown for a sharp-edged 75° delta wing was reported by Visbal [138] in 1994. Simulations were performed with a compressible RANS formulation at $M = 0.2$ and $Re_{cr} = 9.2 \times 10^3$. The low Reynolds number was chosen to match experimental findings and to enable laminar-flow simulations. Laminar flow modelling reduced grid requirements, and for this study grids varied between 1.2×10^6 and 2.3×10^6 points. Results captured the lag in breakdown location during the ramp increase in angle of attack as compared to a fixed angle of attack. Simulated onset and progression of breakdown over the wing correlated well with experiment as did some flowfield details through the burst vortex. Topological analyses within the vortex breakdown bubble were also included. Visbal also showed that the breakdown bubble topology for his delta wing analysis resembled a vortex breakdown bubble topology from the experimental vortex tube research of Faler and Leibovich [59], Fig. 75. Progression of breakdown with a ramp increase in angle of attack was also studied numerically by Jones et al. [126] in 2009 for a 70° delta wing. Critical helix angle theory correlated with other vortex breakdown flow features, but no correlations with experiment were included. Visbal's analysis would be of interest for turbulent flow simulations with current techniques such as Hybrid RANS/LES, WMLES, or wall-resolved LES.

Supersonic analysis was reported by Hadidoolabi and Ansarian [139] in 2018 for a 60° delta wing with ramp changes in angle of attack between 12° and 20° as well as between 30° and 44°. The study included pitch rate effects, and limited subsonic results studies were also performed. Conditions were chosen to transect supersonic shock-vortex interaction domains shown by Miller and Wood [49]. During the pitch up, flow patterns known from prior stationary analysis were observed but with a time delay. Simulated flow patterns were confirmed by comparison with experimental data. Time lags in vortex breakdown were also observed, but no data were available to assess these predictions.

Finally, we comment that hysteresis effects are common for dynamic motions of slender wings with concentrated vortex flows, especially as regards near-field vortex breakdown effects. One experimental study for longitudinal pressure gradient effects for a 70° delta wing was given by Gursul and Yang [140] in 1995 to guide interpretation of experimental findings – essentially a test technique finding. Hysteresis occurs both in angle of attack and sideslip motions and contributes longitudinal and lateral effects for maneuvering configurations. Prediction of these effects with CFD will be another important capability to establish.

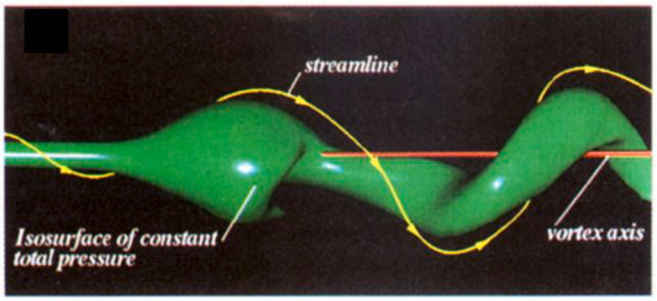

(a) RANS, Λ_{le} = 75° delta wing, M = 0.2, Re_{cr} = 9.2 × 10³, α = 25°

(b) Experiment, tube vortex

Fig. 75. Vortex breakdown bubbles. Visbal [118], 1994.

3.2. State of the art for configuration application capabilities

The presentation of survey findings for vortical flow simulations motivated by configuration aerodynamics is organized into three parts based upon the vehicular scale of the vortical simulations. Applications are first shown in Subsection 3.2.1 for concentrated vortex flow simulations motivated by configuration subcomponents such as vortex generators. Applications are then shown in Subsection 3.2.2 for component-scale concentrated vortex flows such as from body or nacelle strakes. Applications are finally shown in Subsection 3.2.3 for concentrated vortex flow simulations motivated by subsystem and system representations of a configuration.

3.2.1. Subcomponent-scale vortices

Vortex generators create subcomponent-scale vortices for flow-control purposes, as described in Subsection 2.2.2.1, and their deployment to resolve flow deficiencies has been accomplished through now established wind-tunnel tests techniques. To perform this deployment computationally requires accurate representation of vortex persistence through the simulated flowfield, either at the edge of a boundary layer (VG) or within a boundary layer (μVG), to capture the correct physical effects of the vortex generator concentrated vortex on downstream flow properties. The authors only found limited computational investigations, and several are reviewed in the following subsections.

3.2.1.1. Low-speed applications. In 2014, Förster and White [141] implemented a computational methodology to predict the flow patterns around a vortex generator and observed the progression of the vortex structure along the wing as incidence angle increased from zero to 30° for $M = 0.2$ and $Re_{mac} = 1 \times 10^6$. Their methodology was based on the ANSYS CFX finite-volume code solving the steady RANS equations with the SST turbulence model. They found that flow separation occurred when the vortex structure produced by the generators broke down. This caused a localized flow separation that, at higher angles, extended to cause global separation and generator engulfment. The results for computed lift and drag showed an excellent correlation with wind-tunnel testing at low angles of attack, a reasonable correlation at moderate angles of attack, but almost no correlation at high incidence due to the inability of steady RANS methodology to simulate massively separated flows at deep-stall conditions.

In 2008, Meunier and Brunet [142] placed μVGs near the leading

edge of a slotted flap mounted on a realistic three-element wing and assessed the prediction accuracy of steady RANS simulations for flow-control problems by comparison with wind-tunnel measurements of chordwise pressure distribution over the flap. The flow conditions were $M = 0.22$, $Re_{mac} = 6.27 \times 10^6$, and $\alpha = 12°$. The correlations were found to be qualitatively good enough to establish confidence that the VGs produced beneficial flow control. In a similar application from 2016, Moen and Dandoi [143] used RANS/SA simulations from the ONERA elsA code to study the DLR-F15 two-element wing configuration at design point conditions, $M = 0.15$, $Re_{mac} = 2 \times 10^6$, $\alpha = 0°$ (nominal high lift) and 6° (elevated high lift), and a flap deflection $\delta_f = 35°$. They coupled their CFD with an optimization technique to vary flap setting and VG characteristics (location, length, height, incidence, and spacing) to maximize the $\alpha = 6°$ lift coefficient while sustaining the $\alpha = 0°$ lift coefficient as a constraint. An increase in C_L at 6° angle of attack was realized from the optimization, but no comparison with experimental data was given.

3.2.1.2. High-speed applications. Small increments in angle of attack and Mach number during transonic flight can cause shock-induced separation that reduces lift and markedly increases drag and pitching moment. With RANS simulations in 2016, Ito et al. [144] examined how arrays of corotating blade-type vortex generators on transonic sweptback wings can alleviate shock-induced boundary layer separation and its detrimental effects. In simulations at $M = 0.85$, $Re_{mac} = 2.3 \times 10^6$, and incidence from 2° to 6°, their computed C_f distributions correlated qualitatively with oil-flow images from experiment and indicated that the VGs helped to maintain attached flow. The simulations showed about a 10% increase in lift at 6° incidence but no comparison with experimental lift values were made. In a related RANS numerical investigation from 2019, Namura et al. [145] applied multipoint design optimization at freestream cruise conditions ($M = 0.85$, $Re_{mac} = 5.86 \times 10^6$) to optimize the shape of vane-type VGs and their placement on the wing at two angles of attack, 1° (cruise) and 5° (critical loading). The shape optimization revealed that VG height and incidence angle control the aerodynamic performance under the cruise and critical conditions, and VGs with higher length-to-height ratios showed better performance. Using one of the shape-optimized VGs found in this study, Namura et al. [145] then optimized the arrangement of those VGs over the wing at cruise conditions to ensure static stability of the pitching moment with minimally increased drag, but no comparisons with experiment were given.

To better understand current RANS capabilities to simulate transonic VG flows, Zastawny [146] analyzed VG simulation approaches in 2016 for either resolved or modeled VG vortices. Vortices were resolved with both blocked and overset (Chimera) grids, and the study was performed at $M = 0.85$, $Re_{mac} = 5.3 \times 10^6$ and incidences from 0° to 3.5°. The modeled VG vortices indirectly simulates the impact that the VGs have on the flow that is otherwise resolved in the RANS grid. All computations were performed with the DLR TAU code.

Results from the three simulation approaches are shown in Fig. 76 with spanwise planes of vorticity magnitude at two distances downstream of a vortex generator trailing edge. At one VG height downstream of the VG, both resolved approaches show a concentrated vortex flow whereas the modeled vortex has already dissipated. At five VG heights downstream, the VG vortex has dissipated for all three approaches. This rapid dissipation was considered to be numerically induced and not representative of anticipated vortex persistence. Zastawny [146] concluded that these approaches were not yet mature and required further study to develop best practices for industrial applications.

During this review, the authors found no evidence of an anchored simulation capability for concentrated vortex flows from vortex generators. This applies to both conventional VGs as well as μVGs; it also applies to low-speed and transonic applications. Critical physics for these applications include vortex persistence and vortex-boundary-layer interactions as well as vortex-shock-boundary-layer interactions at high speeds.

3.2.2. *Component-scale vortices*

Component-scale concentrated vortices include those generated by fuselage strakes (see Fig. 5) and nacelle strakes (see Fig. 2(b)). Survey results found few papers for fuselage strakes and several papers for nacelle strakes. Both applications are reviewed below.

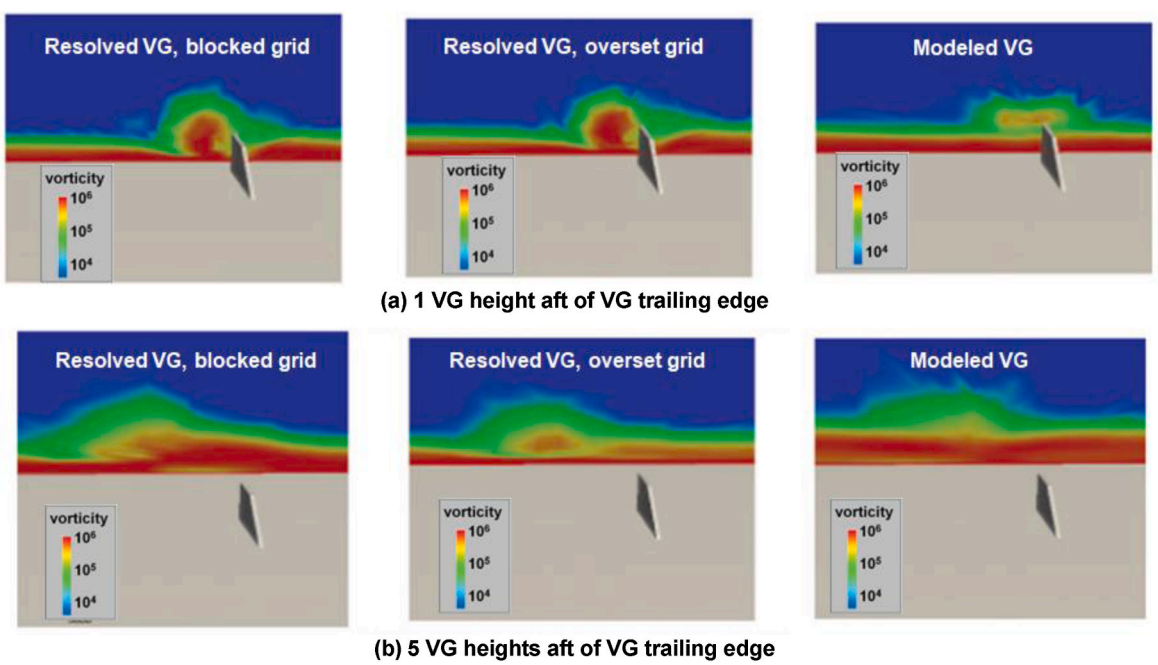

Fig. 76. Vorticity magnitude contours computed with different VG methodologies. RANS, DLR TAU code. $M = 0.85$, $Re_{mac} = 5.3 \times 10^6$, $\alpha = 3.5°$. Zastawny [146], 2016.

3.2.2.1. Fuselage strakes. A significant advancement to high angle-of-attack aerodynamic performance of the Eurofighter EF2000 was reported by Hitzel and Osterhuber [9] in 2018. In this work, enhanced high-angle-of-attack maneuverability of the combat aircraft was achieved through vortex flow control, chiefly from a fuselage strake, and the work included significant URANS CFD analysis. A summary of this accomplishment for subsonic speeds is shown in Fig. 77. Fig. 77(a) shows 3 geometric modifications for the EF2000 Enhanced Maneuverability (EFEM) configuration: a fuselage strake, a Leading-Edge Root Extension (LERX), and a somewhat extended trailing-edge flap. Component testing, both physical and numerical, demonstrated that the concentrated vortex from the fuselage strake was chiefly responsible for energizing the windward wing flow (Fig. 77(b)) such that favorable lateral stability was achieved throughout the angle-of-attack range of interest (Fig. 77(c)). Concentrated vortex flow physics for this application included vortex persistence, vortex interactions, vortex breakdown, and vortex unsteadiness. Additional discussion has been given by Hirschel et al. [147], p373-376.

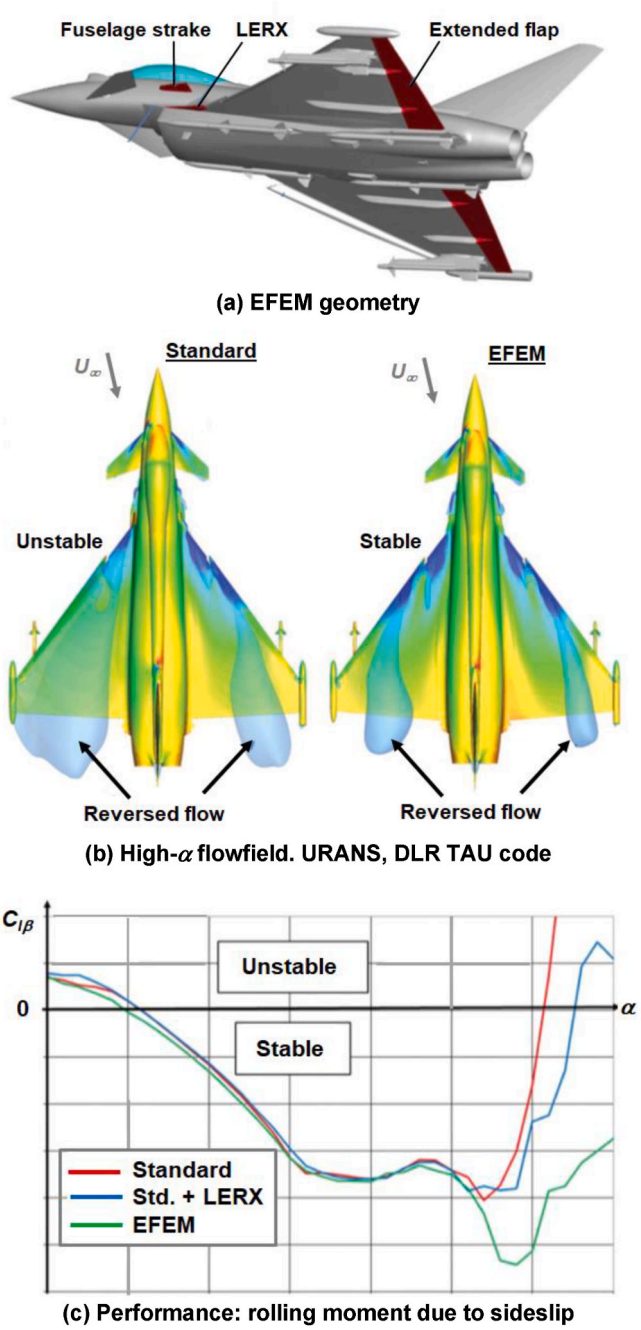

Fig. 77. Fuselage strake application. Subsonic. Hitzel and Osterhuber [9], 2018.

Such a development program requires a very large number of conditions to be analyzed. These would include:

- angle of attack polars, with and without sideslip, up to very high values;
- subsonic, transonic, and supersonic speeds;
- configuration modification parametrics (multiple fuselage strake geometries and locations, multiple LERX geometries, multiple flap extensions);
- independent and coupled effects of configuration modifications;
- control surface settings appropriate to the various flow conditions.

For CFD analysis, grid and modelling effects must also be assessed, and the work must be performed with complex aircraft geometry at wind tunnel and flight Reynolds numbers. The large number of conditions with an aircraft geometry at high Reynolds numbers can often necessitate significant use of lower-physics methods, such as URANS, to provide the necessary analysis in support of the program objectives.

This development program included wind tunnel testing, CFD simulations, and flight testing. This integrated approach was leveraged to reduce the extent of physical testing and CFD simulations from what would have been needed without integration. The scope of this project is not uncommon for industry development programs; further analysis of simulation needs for combat aircraft development is included in Section 5.1.

The authors found it noteworthy that so few studies for fuselage strake applications were found in the literature survey. Fuselage strake vortex analysis demonstrated significant effects for configuration aerodynamics, but no evidence was found for anchoring the simulation methods against concentrated vortex flow fundamentals such as vortex strength, trajectory, and persistence.

3.2.2.2. Nacelle strakes. As discussed in Subsection 2.2.2.3, nacelle strakes create a concentrated vortex that persists downstream over the wing to reduce or even eliminate localized adverse flow separation on the wing at high-lift conditions. This application of a concentrated vortex flow occurs in a very complex flow environment due to the many leading- and trailing-edge devices that are deployed at the high-lift conditions. Other concentrated vortices form from the exposed edges of high-lift devices as well as from the nacelle pylon. An overview of CFD predictive capability for high-lift flows was given by Rumsey and Ying [148] in 2002.

Two activities have focused on computing this complex flowfield for realistically configured high-lift wings. The first activity was comprised of the EUROLIFT I project [149] in 2004 followed by the EUROLIFT II project [150] in 2007. Both these projects used the DLR F11 configuration. (See, Hirschel et al. [147], p248-253, for further discussion.) The second activity is comprised of the High Lift Prediction Workshop (HLPW) series. Four workshops spanning 2011 [151] to 2022 [91] have been held to date. The focus of the HLPW research is the high-lift version of the Common Research Model (CRM-HL). Several results that included a focus on the strake vortex effect in numerical simulations follow.

Koklu et al. [152] used a compressible unsteady Lattice-Bolztmann Method in 2021 to show the vortical structures generated by the various parts of the CRM-HL model for the near-stall condition ($\alpha = 16°$), Fig. 78. The flow was displayed using λ_2 isosurfaces colored by streamwise vorticity to show the vorticity direction, and the results include both the nacelle strake off and nacelle strake on configurations. A complex suite of concentrated vortices is observed in the vicinity of the wing-pylon juncture, and these include both sharp-edge separation vortices from the slat side edges as well as smooth-surface separation

vortices from the pylon. The nacelle strake generates a strong vortex that is shown to persist downstream but only part way over the wing in terms of the λ_2 isosurface visualization, Fig. 78(b). This implies the vortex has dissipated. No correlations with experiment for the strake vortex strength, trajectory, or persistence were reported.

Von Geyr et al. [153] used a RANS formulation in 2007 to simulate the nacelle/pylon vortex system over the DLR F11 configuration also for a near stall condition ($\alpha = 17.5°$). Fig. 79 shows the vortical structures visualized by isosurfaces of vorticity magnitude colored by streamwise vorticity to show the rotation. Once again, a pylon/slat-edge vortex system is observed, but for these conditions the nacelle strake was visualized beyond the wing trailing edge, Fig. 79(b). Once again, no correlations of the strake vortex strength, trajectory, or persistence were reported.

Further analysis from von Geyr et al. [153] is shown in Fig. 80 to assess the nacelle strake effect on supressing wing flow separation. The surface flow is visualized with streamlines and contours of the streamwise skin-friction coefficient, C_{fx}. When C_{fx} nears zero the flow begins to separate, and for the displays shown C_{fx} is bounded as: red $= 0 < C_{fx} <$ 0.011 $=$ blue. Fig. 80(a) shows that there are significant red areas of converging skin-friction lines indicating separation over the leading-edge flap and main wing for the model without the nacelle strake. With the nacelle strake added in Fig. 80(b) we see a virtual elimination of these red areas showing attached flow over most of the leading-edge flap and main wing.

Simulation of transport high-lift flows is still a very challenging task due to both geometric and flowfield complexities. It is this environment for which nacelle strake concentrated vortices must contribute to high-lift performance. The current state of the art now allows these complex simulations to be performed. However, the analysis of nacelle strake vortices appears to have been limited to strake-on vs strake-off overall effects. Basic quantification of the strake vortex strength, trajectory, and persistence will be needed for comparison with experiment to realize an accurate and reliable simulation capability. From the authors' perspective, leading-edge devices and the pylon would each be components for their respective subsystems, and thus the high-lift flow regards many component-scale concentrated vortices and their interactions. An anchored simulation capability for one of the concentrated vortices from one component (e.g., the sharp-edged nacelle strake) could also improve simulation capability for related component vortices (e.g., from the sharp edges of a deployed slat). See Fig. 81, modified from Slotnik [154]. The hierarchical perspective to concentrated vortex flows could provide a means to associate simulation improvements from one targeted activity with other configuration interests.

3.2.3. *Subsystem- and system-scale vortices*

Survey findings of concentrated vortex flow simulations at the subsystem and system scales for configuration vortex-flow aerodynamics are summarized. For the purposes of this review, distinctions between subsystem and system scale analyses were unnecessary. Configuration aerodynamics results are presented for a UCAV configuration (1303) in Section 3.2.3.1, a UCAV concept (SACCON) in Subsection 3.2.3.2, the F-16XL aircraft in Subsection 3.2.3.3, the X-31 configuration in Subsection 3.2.3.4, and a missile concept as well as a combat aircraft concept in Subsection 3.2.3.5.

3.2.3.1. Configuration 1303. Interest in a UCAV concept known as 1303 was established by the Air Force Research Laboratory (AFRL) in collaboration with Boeing as reported by Billman and Osborne [156] in 1998. A subsequent multinational collaborative research program focused on the 1303 configuration was undertaken in the early 2000s by The Technical Cooperation Program (TTCP) under the auspices of the Aerospace Systems Group Technical Panel 5 (AER TP-5). Some basic design principles for this configuration were given by Woolvin [157] as part of a six-paper special session at the 2006 AIAA 24th Applied Aerodynamics Conference. The special session also included computational and experimental findings from the TTCP program.

Several studies were performed following the TTCP program, and one example is shown in Fig. 82 from Sherer et al. [155] in 2011. In this work, simulations were performed with the AFRL high-order wall-resolved LES code FDL3DI to compare with flowfield measurements from a water tunnel investigation at Lehigh University. This approach allowed the Reynolds number to be matched between simulation and experiment. For this work, the leading edge of the 1303 configuration was sharp. The flowfield in Fig. 82(a) shows instantaneous vorticity isosurfaces that are colored by velocity. Fig. 82(b) shows u-component velocity comparisons at the 80-percent semispan station. The comparisons are quite good, and representative of many other results of this study. The high-order wall-resolved LES simulations appear to be very promising for capturing these complex and unsteady vortex flows but become prohibitively expensive at typical wind tunnel and flight Reynolds numbers with current computer technology.

3.2.3.2. SACCON. The NATO/STO Task Group AVT-161 coordinated a research program in the 2000s that included static and dynamic stability

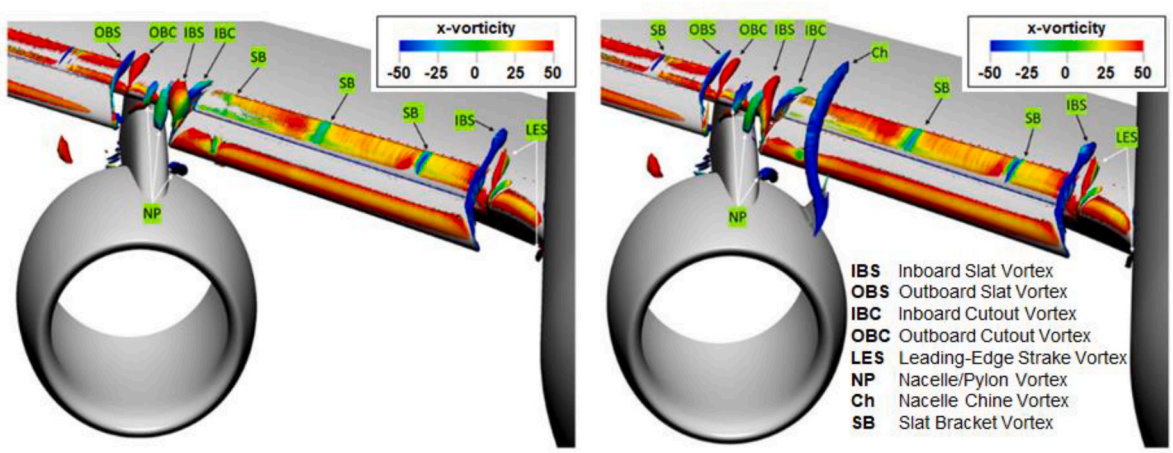

(a) Nacelle strake off **(b) Nacelle strake on**

Fig. 78. Nacelle strake effect on vortices in the pylon/wing region, CRM-HL model. Lattice Boltzmann, commercial code. $M = 0.2$, $Re_{mac} = 3.27 \times 10^6$, $\alpha = 16°$. Koklu et al. [152], 2021.

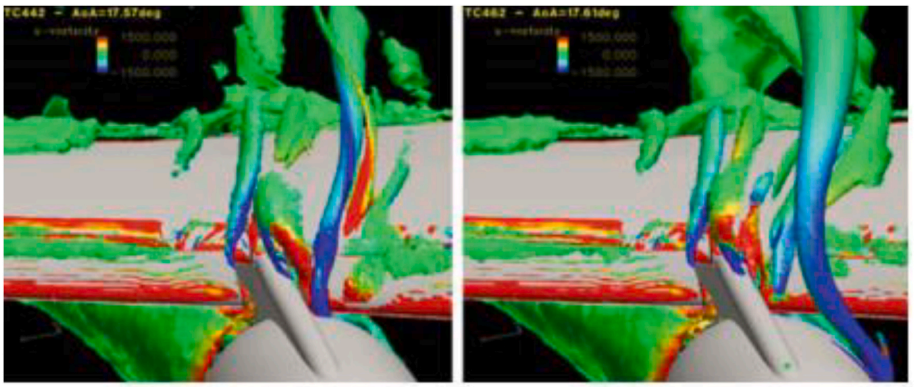

Fig. 79. Effect of nacelle strake on vortices in the pylon/wing region, DLR F11 model. RANS, DLR TAU code. $M = 0.2$, $Re_{mac} = 25 \times 10^6$, $\alpha = 17.5°$. von Geyr et al. [153], 2007.

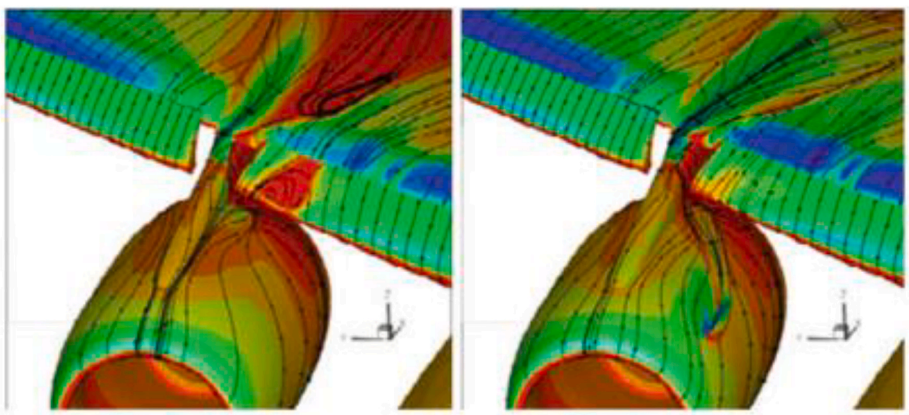

Fig. 80. Effect of nacelle-strake vortex on flow separation over the nacelle and wing, DLR F11 model. RANS, DLR TAU code. $M = 0.2$, $Re_{mac} = 25 \times 10^6$, $\alpha = 17.5°$. von Geyr et al. [153], 2007.

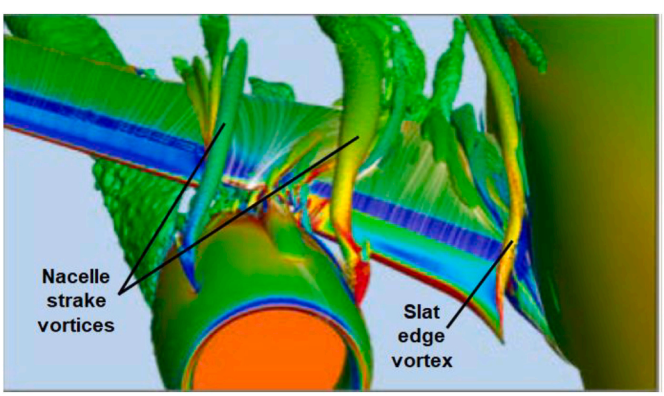

Fig. 81. Concentrated vortices from sharp-edged components. Modified from Slotnik [154], 2021.

assessments of a UCAV configuration known as SACCON. The SACCON configuration incorporated many design features representative of UCAVs in such a way that configuration assessments could be performed within the NATO AVT-161 Task Group. The program included computational and experimental studies with an emphasis on forced oscillation unsteady conditions. Fig. 83 shows the SACCON configuration in the closed test section of the Braunschweig low-speed wind tunnel DNW-NWB. This overall program has been summarized by Cummings and Schütte [158] as part of a collective publication of 8 articles in the AIAA Journal of Aircraft [159] in 2012. Additional details can be found in the NATO AVT-161 final technical report [160].

One interest in the SACCON research regarded the static aerodynamics of the vehicle through wing stall, and a main finding of this research was the lack of agreement of CFD predictions at high angle of attack maneuver conditions where rapid changes in pitch stability occurred prior to approaching the maximum lift coefficient $C_{L,max}$. An example of the static lift and pitching moment variation with angle of attack is shown in Fig. 84 and includes RANS CFD predictions from the NASA USM3D code using a range of turbulence models.

The spanwise variations in leading-edge radius and thickness contributed to multiple interacting vortices at these conditions. An example of the wing vortex flowfield through the nonlinear ptching moment range is shown in Fig. 85 with superimposed surface C_p contours and surface flow traces. The wing flow analysis by Schütte et al. [162] identified an apex vortex associated with the sharp leading edge in that region, a midspan thickness vortex due to spanwise variation in thickness, and a blunt-leading-edge vortex. From the AVT-183 diamond wing research, the leading-edge vortex system seems to evidence incipient separation as well as the inner vortex, Fig. 85(a). The multiple concentrated vortices and their vortex interactions result in rapidly changing flow patterns shown in Fig. 85 and probably contribute to the abrupt changes in pitching moment coefficient shown in Fig. 84.

Examples of the effect of turbulence model and equation formulation on the off-body concentrated vortex flowfield are shown in Fig. 86 for

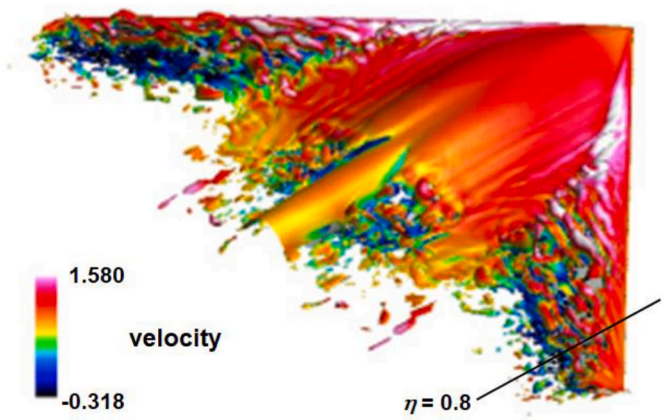

(a) Instantaneous vorticity isosurface

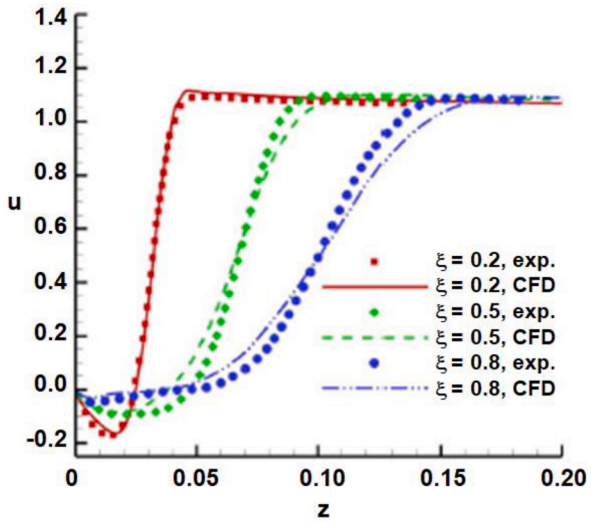

(b) Normal variation of streamwise velocity, $\eta = 0.8$

Fig. 82. 1303 UCAV configuration. WRLES, AFRL FDL3DI code. $\Lambda_{le} = 47°$, $M \approx 0$, $Re_{mac} = 29.9 \times 10^3$, $\alpha = 12°$. Sherer et al. [155], 2011.

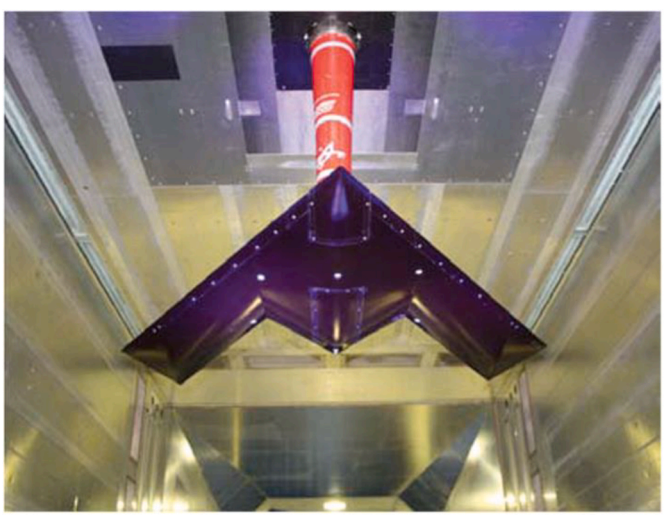

Fig. 83. SACCON low-speed wind-tunnel model. Cummings and Schütte [158], 2012.

USM3D RANS simulations and in Fig. 87 for simulations from the Swedish Defense Research Agency (FOI) Edge code with RANS and hybrid RANS/LES formulations at conditions corresponding to the rapid changes in pitching moment stability from Fig. 84. These results demonstrate significantly different vortex flowfields in association with the different turbulence models and formulations. It is noted that these results are from well-established codes using well-established turbulence models with well-established formulations. They indicate a deficiency in the current state of the art for predicting the complex vortical flows associated with rapid pitch stability changes on a UCAV configuration at static conditions.

The AVT-161 SACCON program emphasized dynamic stability, and CFD assessments were compared with forced oscillation wind tunnel measurements. One example is shown in Fig. 88 from Frink et al. [161] for the effect of turbulence model on the dynamic pitching moment coefficients at two forcing frequencies. Neither turbulence model provides a good correlation with the data although the SA turbulence model results appear to be closer to the experimental data than are the SST turbulence model results. UCAV configurations can take advantage of more extreme dynamic maneuvers as compared to inhabited vehicles, and improved predictive capability for concentrated vortex effects on dynamic maneuver properties are warranted for this vehicle class.

The authors note that two follow-on studies of the SACCON configuration were performed through the STO, one on an enhanced design of the vehicle (AVT-201 [163]) and the other regarding multidisciplinary design considerations (AVT-251 [164]).

3.2.3.3. F-16XL. NASA conducted a research program in the 1990s, the Cranked Arrow Wing Aerodynamics Program (CAWAP), to obtain flight data regarding concentrated vortex flows with an F-16XL aircraft, Fig. 89. The F-16XL had a cranked wing, $\Lambda_{le} = 70°/50°$, with a leading-edge s-blend to interface the wing to the fuselage. The CAWAP data included static surface pressures, skin friction, boundary layer profiles, and surface as well as off-body flowfield images. Flow conditions spanned subsonic, transonic, and supersonic speeds for a broad angle-of-attack range. Preliminary CFD assessments by Lamar [165] at a NATO vortex flow symposium [166] identified a number of deficiencies in the predictions, and a new program, CAWAP International (CAWAPI), was initiated in the early 2000s to address these shortcomings. (See, Obara and Lamar [167], 2009.) Two subsequent programs were performed, CAWAPI-2 and CAWAPI-3, to address challenges identified from the CAWAPI research. Collective findings have been given in the AIAA Journal of Aircraft with 7 articles for CAWAPI [168] in 2009, 8 articles for CAWAPI-2 [169] in 2017, and 7 articles for CAWAPI-3 [170] in 2017. All the F-16XL CFD was performed after the F-16XL flight test program was complete so there was no opportunity for the computations to guide new measurements.

For the CAWAPI program, analysis flight conditions were established that included low-speed high-angle-of-attack ($C_L \approx 0.78$), moderate-speed moderate-angle-of-attack ($C_L \approx 0.44$), and high-transonic-speed low-angle-of-attack flows ($C_L \approx 0.12$). Aircraft surface modelling was improved, and the effects of refined grids, flow solver formulations, and turbulence models were determined. Summary findings were given by Rizzi et al. [86] and significantly improved predictions for the moderate-speed moderate-angle-of-attack conditions were accomplished. (See, Figs. 46 and 47 of Subsection 2.4.1.3.) Correlations for both the low-speed high-angle-of-attack and the high-transonic-speed low--angle-of-attack conditions did not improve. For example, the standard deviation among CAWAPI CFD solutions for the high-angle-of-attack case was three times that of the moderate-angle-of-attack case. These conditions served as the focus for the CAWAPI-2 and CAWAPI-3 studies.

For the CAWAPI-2 program, additional flight conditions were identified to support analysis of concentrated vortex flow structures (secondary vortices, vortex breakdown), airframe effects (control surface and aeroelastic deflections), and flight test conditions. The effects of

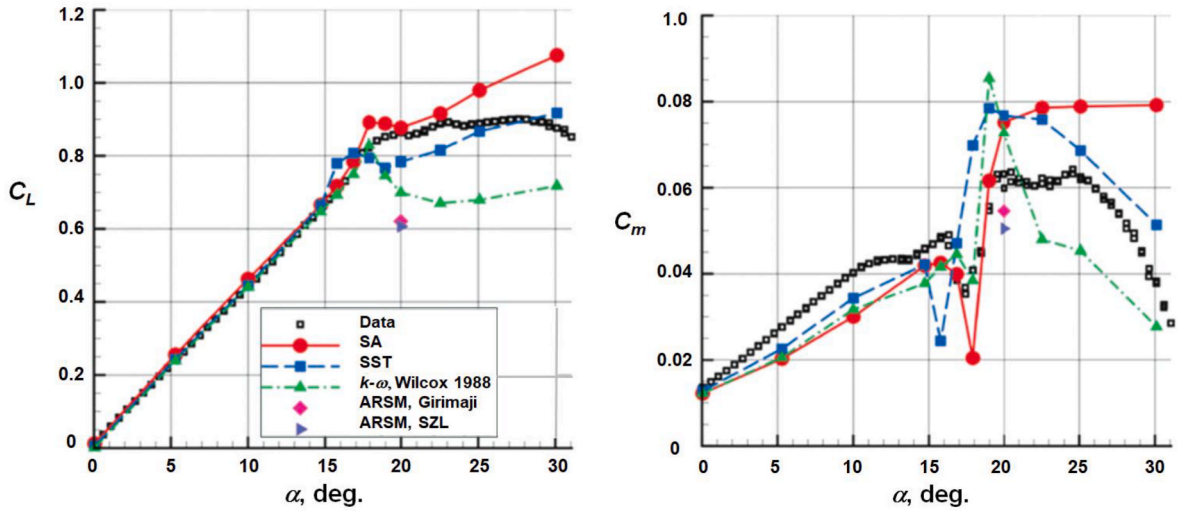

Fig. 84. Effect of turbulence model on SACCON static lift and pitching moment coefficient. RANS, NASA USM3D code. $\Lambda_{le} = 53°$, $M = 0.144$, $Re_{cref} = 1.6 \times 10^6$. Frink et al. [161], 2012.

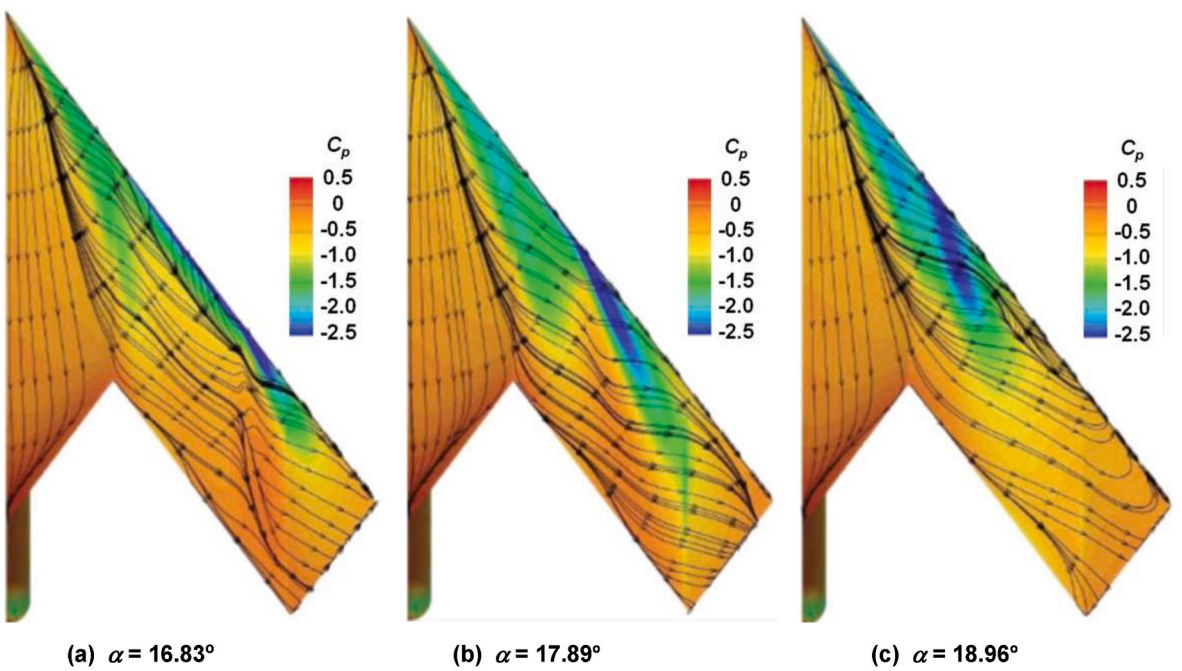

Fig. 85. SACCON surface C_p contours and flow traces. RANS, NASA USM3D code, SA. $\Lambda_{le} = 53°$, $M = 0.144$, $Re_{cref} = 1.6 \times 10^6$. Frink et al. [161], 2012.

significantly finer grids were included with further flow modelling assessments. One accomplishment from CAWAPI-2 was improved secondary vortex predictions for the low-speed, high-angle-of-attack flight condition, and an example is shown in Fig. 90 from a due diligence assessment by Elmiligui et al. [171] for physical modelling and numerical resolution effects. The primary vortex induces a significant adverse pressure gradient in the spanwise direction of the upper wing surface that causes the boundary layer to separate from a smooth surface and form the secondary vortex, Fig. 90(a). Near separation and in the presence of strong pressure gradients, the boundary layer is expected to be in nonequilibrium with conditions of production, transport and dissipation of turbulent kinetic energy changing rapidly and far from the state on which turbulence models are based. If we consider the two turbulence models in question, SA and k-ε, we realize major differences in the treatment of turbulent kinetic energy. The two-equation k-ε model solves for the transport of turbulent kinetic energy and its dissipation rate, whereas the one-equation SA model solves only for the transport of turbulent kinetic viscosity coefficient, substantially different from the energy transport equation in k-ε. There are more *ad hoc* terms in the SA transport equation than in k-ε, which suggest that SA fails to predict secondary separation because it does not transport the right quantities. Through a combination of grid resolution and turbulence model assessments, Elmiligui achieved the improved secondary vortex resolution with correspondingly improved correlations with the flight test data. Summary findings from CAWAPI-2 were given by Rizzi and Luckring [172].

The CAWAPI-3 program was focused on the low-speed high-angle-of-attack condition and, in particular, on surface pressure correlations for the wing outboard panel. It was anticipated that unsteady vortical effects, such as associated with vortex interactions and vortex breakdown, were contributing to the lack of correlation between previous steady RANS simulations and flight test data. All CAWAP flight-test data were

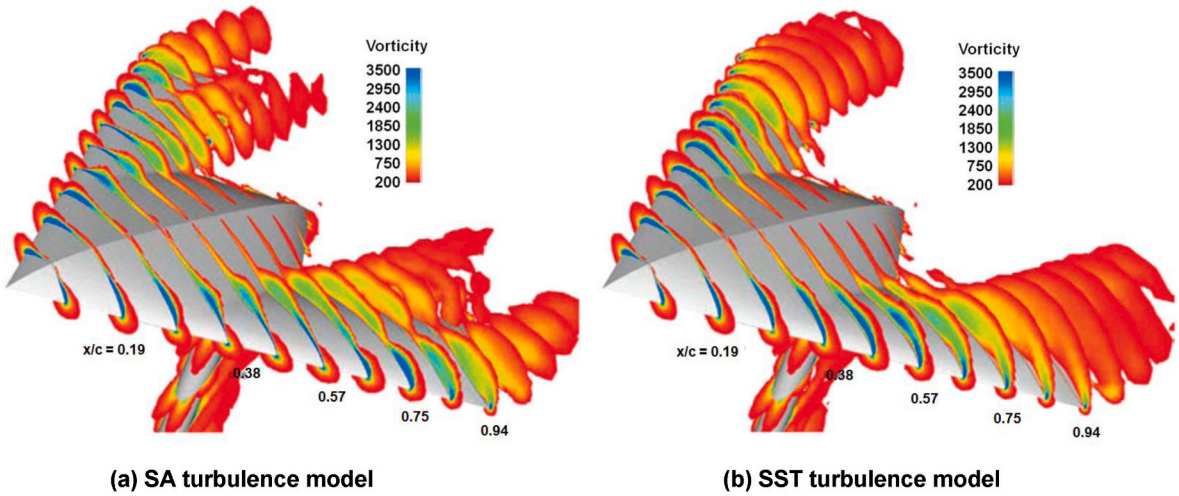

Fig. 86. Effect of turbulence model on SACCON vortex flows. RANS, NASA USM3D code. $\Lambda_{le} = 53°$, $M = 0.144$, $Re_{cref} = 1.6 \times 10^6$, $\alpha = 16.83°$. Frink et al. [161], 2012.

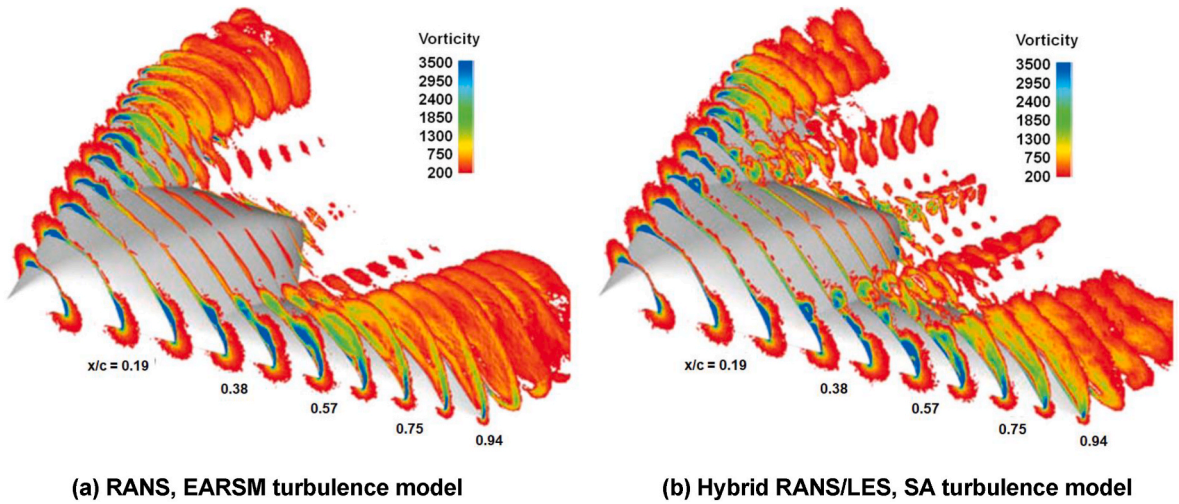

Fig. 87. Effect of turbulence model on SACCON vortex flows. FOI EDGE code, adapted grid. $\Lambda_{le} = 53°$, $M = 0.149$, $Re_{cref} = 1.6 \times 10^6$, $\alpha = 17.39°$. Frink et al. [161], 2012.

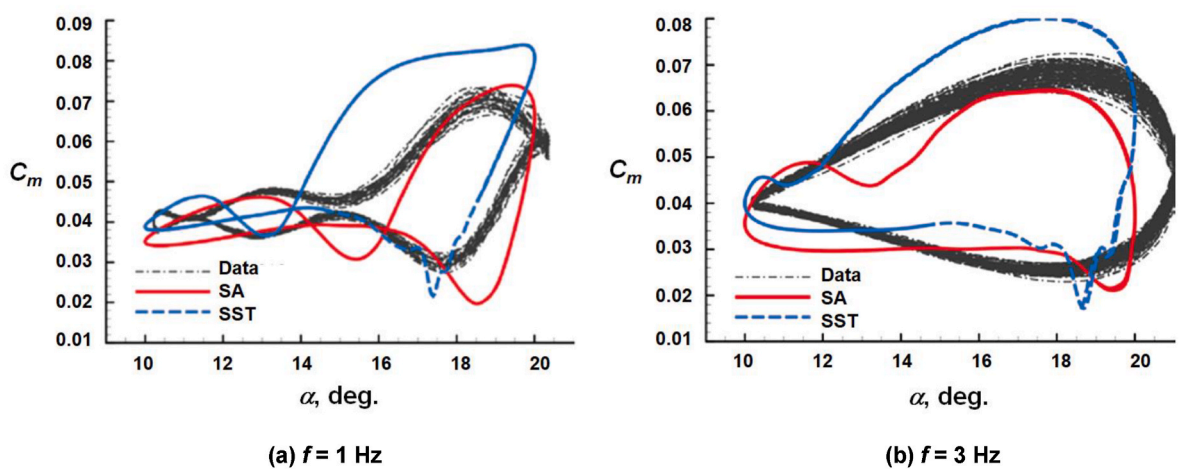

Fig. 88. SACCON forced oscillation pitching moment. URANS, NASA USM3D code. $\Lambda_{le} = 53°$, $M = 0.144$, $Re_{cref} = 1.6 \times 10^6$, $\alpha_0 = 15°$, $\Delta\alpha = \pm 5°$. Frink et al. [161], 2012.

Fig. 89. CAWAP program. F-16XL-1 aircraft, $\Lambda_{le} = 70°/50°$. Lamar et al. [83], 2001.

measured assuming steady flow, and the steady RANS simulations were appropriate for many of the prior analysis conditions.

All CAWAPI-3 simulations were performed with hybrid RANS/LES formulations to represent the unsteady concentrated vortex effects. One sample result is shown in Fig. 91 from Lofthouse and Cummings [173]. Unsteadiness in the solution is represented by one standard deviation about mean pressures as well as by the maximum and minimum pressure excursions. This simulation, and others from CAWAPI-3, indicate significant unsteady effects on the surface pressures. The one-standard-deviation bounds bracket the measurements and at least imply that unsteadiness could be a source affecting the measurements as well as lack of correlation with prior steady-flow simulations. New measurements to quantify such an unsteady vortical flow would be useful. Summary findings from CAWAPI-3 were given by Luckring et al. [174].

3.2.3.4. X-31. Detailed numerical and experimental studies were performed for the X-31 configuration as part of the NATO RTO Task Group AVT-161. An emphasis for this work was assessment of the static and dynamic stability and control features of the X-31 and how these properties were affected by concentrated vortex flows. An overall program description has been given by Schütte et al. [175] as part of a collective publication in 2012 of 6 articles in Aerospace Science and Technology [176]. A photograph of the X-31 wind tunnel model is shown in Fig. 92. Two low-speed results follow.

The complex concentrated vortex flowfield for the X-31 configuration at maneuver conditions is shown in Fig. 93 with RANS simulations from Boelens [177] using the blocked structured-grid solver ENSOLV from NLR. The computation used a relatively modest grid for an aircraft configuration of approximately 25 million cells and the solution shows numerous vortices associated with the canard, fuselage, inlet, and wing. Boelens also modeled the flow through the gaps between the leading-edge flap segments, and the gap flow produced a succession of concentrated vortices. Flap gaps are a practical attribute of aircraft geometries but are rarely modeled in CFD simulations. The succession of flap gap vortices fundamentally altered the wing outboard flow as compared to Boelens' simulations without the flap gaps. In this later case, the simulations had a single leading-edge vortex. Improved pitching moment correlations with experiment were also achieved with the solutions that included the flap gap effects. Boelens' work was performed at wind tunnel test conditions, and it seems likely that this gap effect could become more pronounced at the high Reynolds numbers associated with full-scale aircraft.

The AVT-161 research program enabled comparisons among numerous codes for the X-31 configuration at maneuver conditions that included concentrated vortex flows. One comparison between simulations from the DLR TAU code and the NLR ENSOLV code is shown in Fig. 94 for a low-speed maneuver condition at an angle of attack $\alpha = 16°$. Computations were performed following established practices with each code and in such a manner as to facilitate comparisons between the codes. The DLR TAU simulations used approximately 50×10^6 cells and

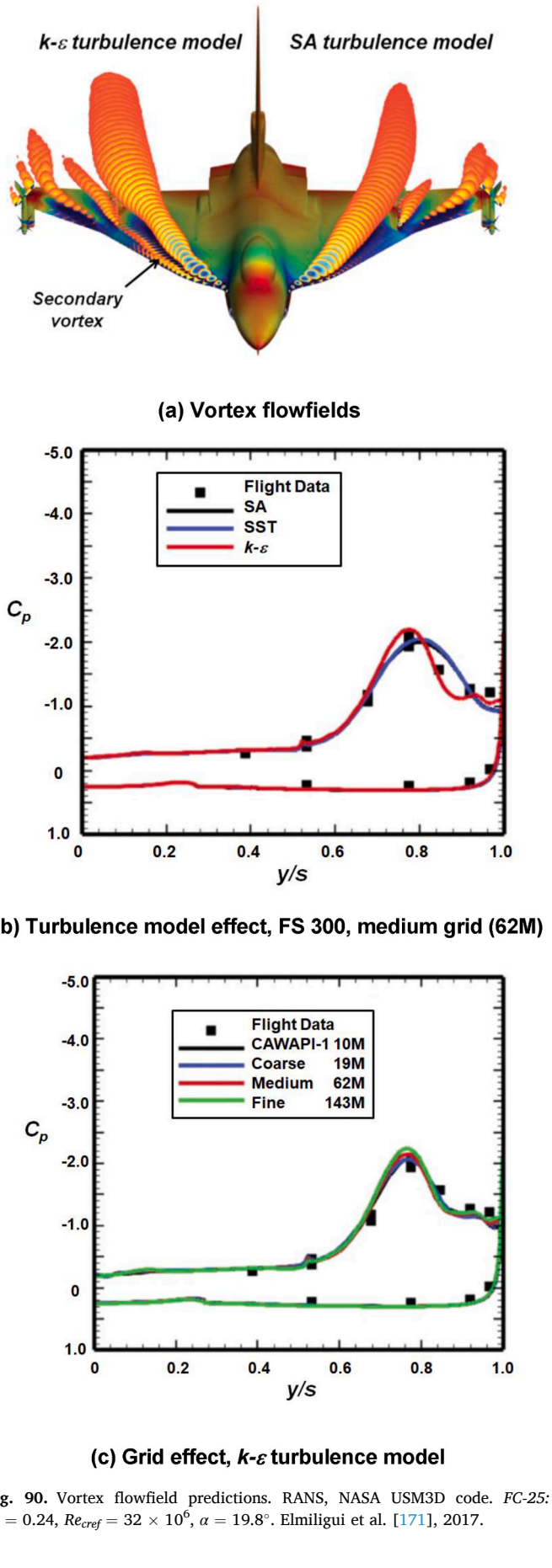

Fig. 90. Vortex flowfield predictions. RANS, NASA USM3D code. *FC-25:* $M = 0.24$, $Re_{cref} = 32 \times 10^6$, $\alpha = 19.8°$. Elmiligui et al. [171], 2017.

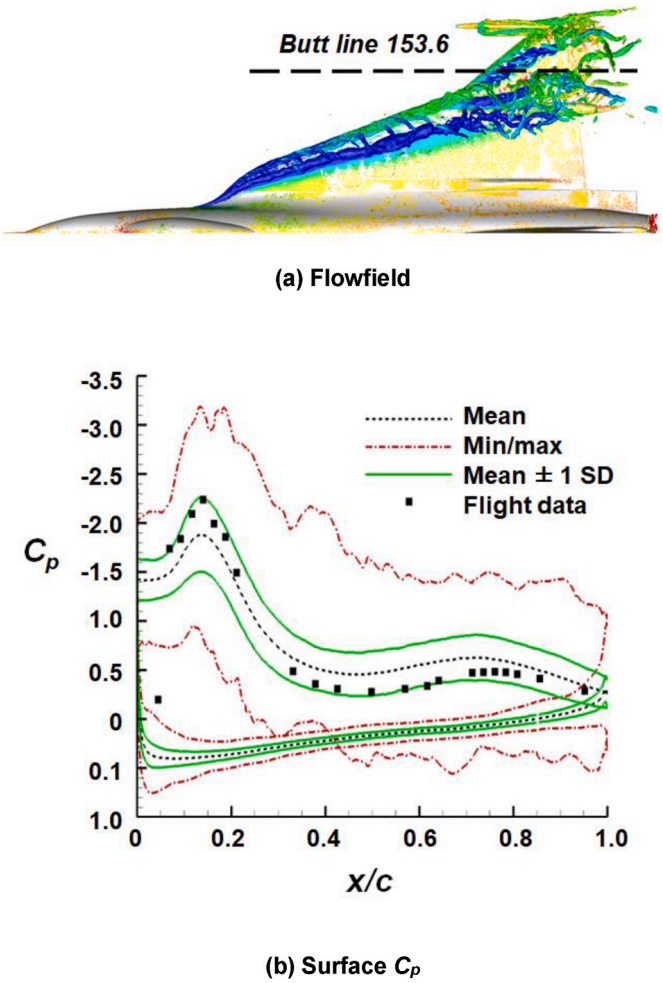

Fig. 91. Outboard panel pressure analysis. Hybrid RANS/LES, DoD Kestrel code. *FC-25:* $M = 0.24$, $Re_{cref} = 32 \times 10^6$, $\alpha = 19.8°$. Lofthouse and Cummings [173], 2017.

Fig. 92. X-31 model. $\Lambda_{le} = 57°/45°$. Schütte et al. [175], 2012.

the SA turbulence model. The NLR ENSOLV simulations used approximately 31×10^6 cells and the TNT k-ω turbulence model. Both simulations included the streamwise gaps between the wing leading-edge flaps.

Both simulations showed some promising correlations with experiment. However, it is also notable from the comparison of surface flow

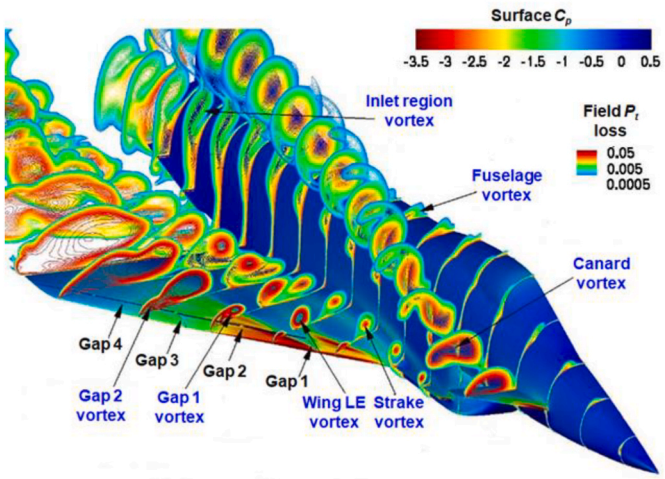

Fig. 93. Flap-gap effect. RANS, NLR ENSOLV code. $M = 0.18$, $Re_{cref} = 2.07 \times 10^6$, $\alpha = 20.08°$. Boelens [177], 2012.

patterns that the two simulations produce significantly different concentrated vortex flows on the wing. A similar result was also shown at an angle of attack $\alpha = 18°$. Both solutions represent state-of-the-art research performed by expert practitioners with well-established codes. Further work is needed to achieve reliable and consistent concentrated vortex flow simulations on complex configurations.

3.2.3.5. Vortex interactions. The SACCON, F-16XL, and X-31 examples have demonstrated that complex vortex interactions occur on practical configurations. Although not shown, vortex interactions also occurred for the 1303 configuration. A recent NATO STO Task Group, AVT-316, was formed to study vortex interactions relevant to military vehicles. The Task Group was organized into two facets, one to focus on missile aerodynamics and the other to focus on combat aircraft aerodynamics. Both facets used configurations that reflected industry interests in a way that could be shared among the NATO participants. Both facets studied conditions for which configuration forces and moments were changing rapidly with vehicle orientation, and both facets included computational and experimental studies. The Missile Facet focused on a configuration, Open Test Case one (OTC1), at a supersonic maneuver condition shown in Fig. 95. The configuration was used to perform blind CFD modelling assessments, and the outcomes from those studies were applied to a second configuration at transonic speeds. The solution shown was computed with a higher-order DES formulation, FLUSEPA, at MBDA France. The Aircraft Facet focused on double and triple delta wings at subsonic and transonic speeds and used a concurrent experimental program to guide their CFD assessments. An example of the triple delta wing flowfield at transonic speeds is shown in Fig. 96 with URANS simulations from the DLR TAU code. Both research configurations demonstrate complex interactions among the concentrated vortex flows as well as interactions with shock waves and surface components. Findings from this research were first reported in six special sessions comprised of 22 papers at the AIAA SCITECH 2022 Forum. A final NATO/STO technical report is in press [181] that includes the program overview by Luckring et al. [182], detailed facet research findings, and facet summary findings by Taylor et al. [179] and Hitzel [180].

Both facets demonstrated the benefits of using adaptive grid technology to capture the complex interacting vortex flows. An example from the Missile facet is shown in Fig. 97 for the OTC1 case study. In this figure, the crossflow plane is situated at the half-root-chord station of the aft control surfaces. The NASA FUN3D simulations were performed with the SA-RC-QCR turbulence model while the LEMMA Niceflow simulations were performed with the SA-RC turbulence model. Grid sizes are expressed as Degrees of Freedom (DoF). Both solutions

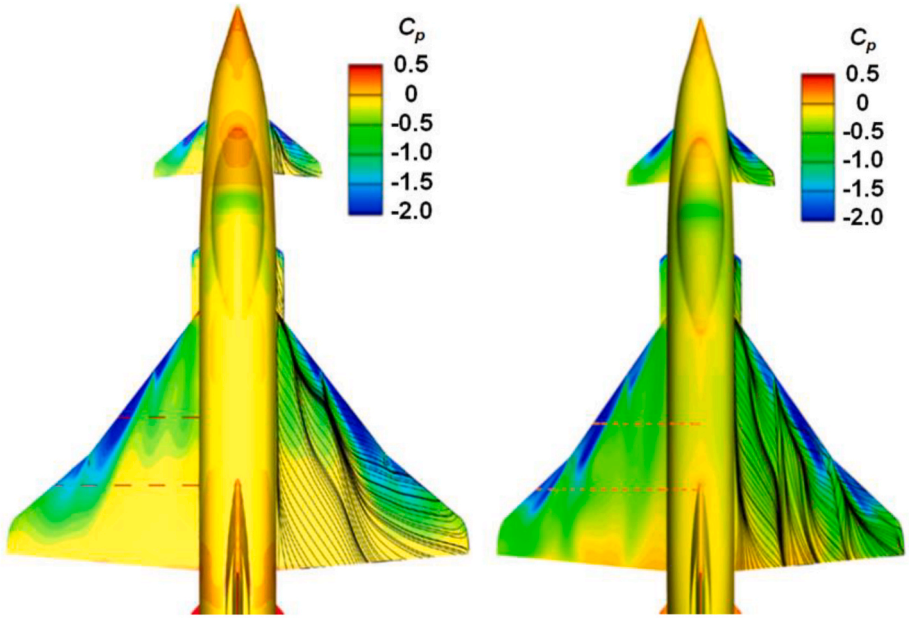

Fig. 94. Surface C_p and flow patterns. RANS. $M = 0.18$, $Re_{cref} = 2.07 \times 10^6$, $\alpha = 16°$. Schütte et al. [178], 2012.

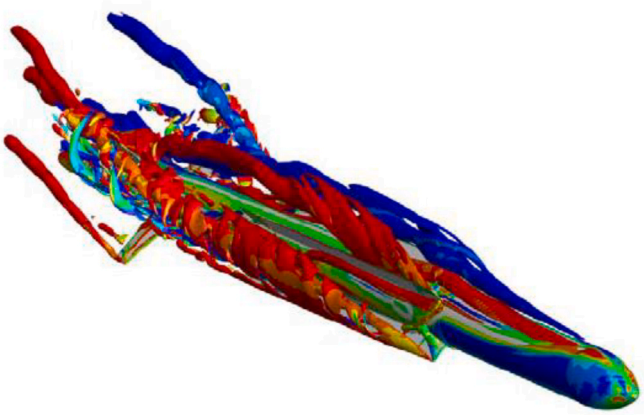

Fig. 95. Vortex interaction research, missile aerodynamics. Hybrid RANS/LES, FLUSEPA code. $M = 1.4$, $Re_D = 4.89 \times 10^6$, $\sigma = 15°$, $\lambda = 2.5°$. Taylor [179] 2024.

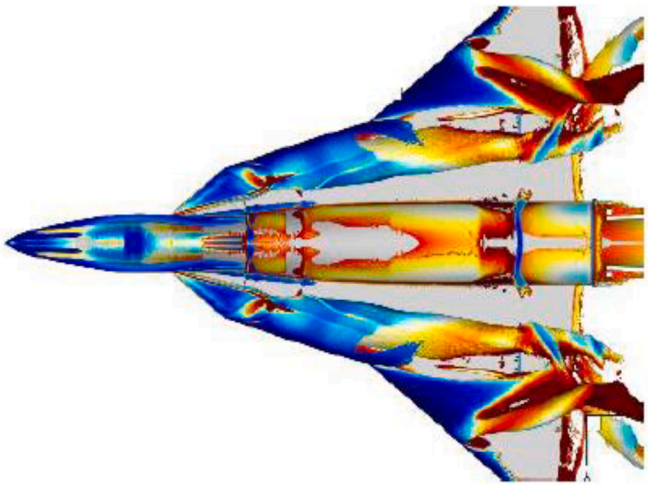

Fig. 96. Vortex interaction research, aircraft aerodynamics. URANS, DLR TAU code. $M = 0.85$, $Re_{cref} = 12.53 \times 10^6$, $\alpha = 20°$. Hitzel [180], 2024.

demonstrate highly complex and interacting flowfields that would be challenging to resolve without adaptive grids. Differences between the solutions demonstrate that work remains to develop a reliable adaptive gridding technology (along with other numerical modelling considerations) for the concentrated vortex predictions.

An example from the Aircraft facet is shown in Fig. 98 for the triple delta wing case study from Vissoneau and Guilmineau [183] using the National Center for Scientific Research (CNRS) ISIS-CFD code. In this figure, the crossflow plane is situated at $x/c_r = 0.592$. In this work, AMR is considered an essential element for complex flow simulations. Simulations were time accurate, and anisotropic grid adaptation was accomplished with a flux-component Hessian based on second derivatives of the velocity fluxes and pressure. Adaptive grid results showed better correlation with wind tunnel test, and the results demonstrated that the complex and interacting aircraft vortex flowfields would be challenging to resolve without AMR. Hybrid RANS/LES produced more reliable results than did URANS, because with LES the turbulent scales are resolved whereas with URANS they are not. The grid size limits the scales that are resolved with LES, and AMR is a very effective means to expand the spectrum of scales for a given number of grid cells in the simulation of interacting concentrated vortex flows.

Vortex interactions also occur between the forebody chine vortex and downstream wing vortices. One article by Jeans et al. [184] from 2009 showed promising force and moment correlations between DDES simulations and wind tunnel data for a generic NASA configuration with a chined forebody known as the Modular Transonic Vortex Interaction (MTVI) configuration, Fig. 99. Their analysis included sideslip effects with rapid breaks in moment properties that were attributed to asymmetric vortex breakdown. Vortex interactions between the chine and wing vortices were also demonstrated. However, no correlations for surface pressure distributions or flowfield properties were shown. More in depth work, both experimental and numerical, seems warranted for chined forebody geometries that have become common for combat aircraft.

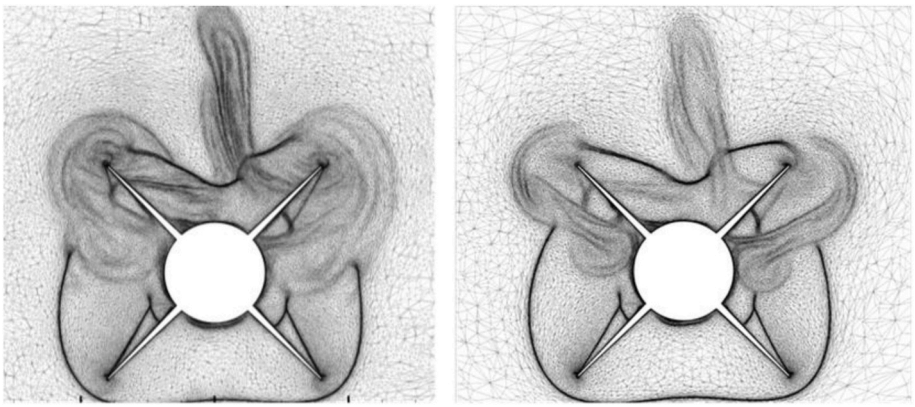

(a) NASA FUN3D code, SA-RC QCR, 51 × 10^6 DoF (b) LEMMA Niceflow code, SA-RC, 41.2 × 10^6 DoF

Fig. 97. Adaptive grid solutions, Missile Facet. RANS. OTC1, $M = 1.4$, $Re_D = 4.89 \times 10^6$, $\sigma = 15°$, $\lambda = 2.5°$. Taylor [179] 2024.

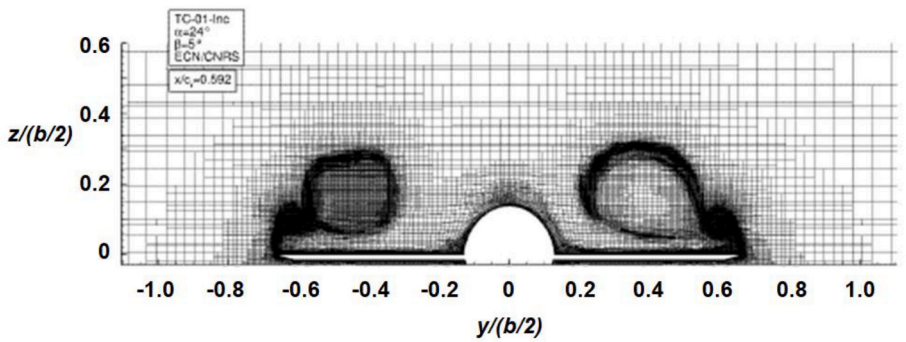

(a) URANS, *k-ω* SST. 89.6 × 10^6 cells, 1.71 × 10^6 surface faces.

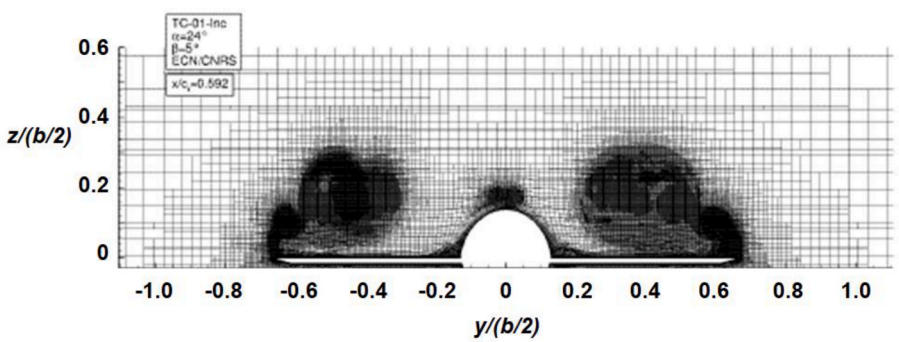

(b) Hybrid RANS/LES, DDES-SST. 97.9 × 10^6 cells, 2.84 × 10^6 surface faces.

Fig. 98. Adaptive grid solution, Aircraft Facet. CNRS ISIS-CFD code. Triple delta wing, $x/c_r = 0.592$, $M \sim 0$, $Re_{cref} = 2.36 \times 10^6$, $\alpha = 24°$, $\beta = 5°$. Visonneau and Guilmineau [183], 2024.

4. Key findings

A summary of the key findings from the present survey is provided below. The summary is organized along the same lines as was used for presentation of findings (Section 3). Key findings for fundamental vortex flow simulations, such as for a delta wing, are first presented in Subsection 4.1, followed by the key findings for aircraft configuration applications, Subsection 4.2. The key findings address both the capabilities for simulating various classes of concentrated vortex flows as well as limitations that have been found from this survey. Limitations are further addressed in Section 5, Path Forward.

4.1. Fundamentals

Fundamental studies can be targeted toward a particular physics-based attribute of concentrated vortex flows that is relevant to configuration-based interests. Subsection 4.1.1 first summarizes the capabilities and limitations for simulating steady concentrated vortex flows, followed by Subsection 4.1.2 that summarizes the capabilities and limitations for simulating unsteady concentrated vortex flows. The distinction between steady and unsteady concentrated vortex flow was given earlier in this article (Subsection 2.3.2, Flow Physics Manifestation).

4.1.1. Steady flows

Details for this summary were presented in Subsection 3.1.1. Steady

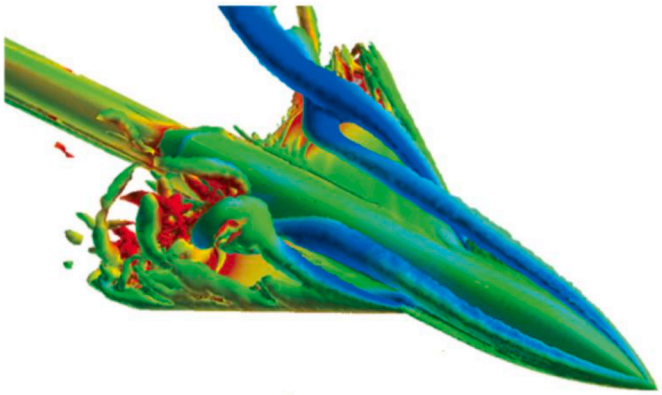

Fig. 99. Chine/wing simulation. DDES, Cobalt Solutions Cobalt code. NASA MTVI, $\Lambda_{le} = 60^\circ$, $M = 0.4$, $Re_c = 2.68 \times 10^6$, $\alpha = 30^\circ$, $\beta = 2^\circ$. Jeans et al. [184], 2009.

concentrated vortex flows that are generated from highly-swept simple wings (e.g., a delta wing) with sharp leading edges can be simulated well with current computational techniques and often with RANS-based formulations. The vortices are coherent; there is no nearfield vortex breakdown. A counterrotating vortex can form in the sharp trailing-edge wake from these wings, and the authors found no evidence of a predictive capability for this vortex. This wake vortex could affect the trajectory of the wing primary vortex and thus influence flows where vortex persistence is of interest.

The authors found very few articles for concentrated vortex flow simulations from chined forebodies. Chined forebodies are common on combat aircraft, and this lack of demonstrated simulation capability is a limitation. Fundamental work to quantify surface and flowfield properties for these concentrated vortex flows seems warranted to anchor simulation capability.

Secondary vortices form from a smooth surface separation and survey findings are mixed for these predictions. Some predictions for simple sharp-edged delta wings compared well with experimental surface pressures; other cases for more complex configurations were more questionable. The boundary layer leading to secondary separation is likely in nonequilibrium, and two-equation turbulence models appear to capture the secondary vortex properties better than simpler models. The survey did not find definitive data for detailed secondary vortex properties. The secondary vortex can affect the position and strength of the primary vortex, and present simulations are not anchored against secondary vortex flow physics.

Primary vortices that separate from blunt leading edges are fundamentally more complex than the sharp-leading-edge case. The survey found that a new structure of blunt-leading-edge vortex separation was established from several research projects enabled by the NATO STO. This structure includes an incipient separation region leading to the onset of primary vortical separation and an inner corotating vortex. The findings have been achieved through multiple wind tunnel tests as well as numerous RANS and hybrid RANS/LES simulations. CFD predictions of this flow demonstrated that most of the wing flowfield is well predicted when the onset of vortical separation matches experimental value. Hybrid RANS/LES methods appear to have done better than RANS methods, but the prediction of this onset location is not well established. CFD is not reliable for predicting blunt-leading-edge vortex flows, and further work is warranted to resolve this deficiency. Fundamental analyses by Polhamus [41] and Poll [44] indicate that classical leading edge separation flow physics (e.g., laminar separation bubbles, turbulent reattachment, turbulent reseparation) could contribute to this phenomenon. Care must also be exercised as regards transition flow physics for blunt-leading-edge studies at typical wind tunnel Reynolds numbers. Hövelmann [111] documented test techniques to assure turbulent blunt-leading-edge flows, and Buzica and Breitsamter [114] documented large effects of allowing this flow to be laminar.

Higher-order wall-resolved LES methods appear to capture a suite of plausible flow physics for blunt-leading-edge vortex separation that are not modeled, or have not been reported, in the current RANS and hybrid RANS/LES simulations found in this review. However, the high-order WRLES methods are currently restricted to low Reynolds numbers (on the order of 10^4) due to grid resolution requirements and computer capacity restrictions. Validation experiments for the WRLES predictions would be of interest as well as research to determine means to approximate the WRLES capabilities in hybrid RANS/LES or even RANS methods.

Finally, Adaptive Mesh Refinement (AMR) appears to be an important technology to grid resolve the key physics for many of these phenomena. Work would be needed to determine that the adaptation process was germane for the relevant concentrated vortex flow physics.

4.1.2. *Unsteady flows*

Details for this summary were presented in Subsection 3.1.2. One of the most critical unsteady flow features for concentrated vortex flows is vortex breakdown. Vortex breakdown is one source of adverse stability and control features such as pitch up or adverse lateral stability. At the time of this review, there is no reliable prediction technique for vortex breakdown. Vortex breakdown involves flow details of the vortex core, and the vortex core has boundary-layer like flow scales. Vortex core properties (including its physical location) are unknown *a priori*, and physics-based AMR appears to be a requirement for vortex breakdown simulations. The AMR needs to be time accurate since vortex breakdown is an unsteady phenomenon on several time scales. Vortex breakdown studies in tubes demonstrated similarities to wing vortex breakdown, and it seems that physics-based validation campaigns could be conducted with these tube studies that would benefit wing interests.

For nonslender wings, global unsteadiness becomes a dominant feature due to vortex bursting properties, vortex shear layer instabilities, and enhanced interactions between the secondary vortex and the primary vortex shear layer. These phenomena are established, but this survey found little evidence of validated simulation capability for the phenomena. Nonslender wings include UCAVs, and reliable simulation capability for unsteady concentrated vortex flows will be important to this vehicle class.

UCAVs also exploit dynamic maneuverability, and concentrated vortex flows exhibit hysteresis effects with dynamic motion. This survey found no demonstrated capability for CFD to simulate hysteresis effects associated with the dynamic motion of slender or nonslender wings with concentrated vortex flows.

4.2. *Configuration applications*

Configuration-based simulations of concentrated vortex flows are challenged by the need for very large grids to model aircraft geometry along with the associated flow details in boundary layers, wakes, and vortices. Subsection 4.2.1 first summarizes the capabilities and limitations for simulating concentrated vortex flows for subcomponent scale applications (e.g., vortex generators). Subsection 4.2.2 summarizes the capabilities and limitations for simulating concentrated vortex flows at the component scale (e.g., nacelle strakes), and Subsection 4.2.3 summarized these capabilities and limitations for subsystem and system scales.

4.2.1. *Subcomponent scales*

Details for this summary were presented in Subsection 3.2.1 and focused on concentrated vortex flows from vortex generators. For these applications, downstream flow control is accomplished through vortex persistence. Results were found for both low-speed and transonic applications and included sub-boundary-layer and conventional VGs. Optimization was used to manipulate VG details toward an integrated

objective such as increased lift coefficient at a given condition. Grid and modelling effects were also assessed. However, the authors found no evidence of an anchored simulation capability for concentrated vortex flows from vortex generators. Critical physics for these applications include vortex persistence and vortex-boundary-layer interactions as well as vortex-shock-boundary-layer interactions at high speeds. The lack of concentrated vortex flow validation for VG applications is a limitation for the current state of the art.

4.2.2. Component scales

Details for this summary were presented in Subsection 3.2.2 and focused on fuselage and nacelle strakes. As with VGs, downstream flow control is accomplished through vortex persistence from these strakes. Practical applications of fuselage and nacelle strakes involve highly complex configuration geometries and flowfields, and results are now being generated for these complex cases. The survey indicated a lack of validation of the concentrated vortex flows even for basic flowfield properties such as the vortex strength, trajectory, and persistence. In many cases, the analysis was limited to strake-on versus strake-off effects. CFD validation campaigns are warranted for this application.

4.2.3. Subsystem and system scales

Details for this summary were presented in Subsection 3.2.3 and addressed several configurations. Excellent flowfield predictions of the semicoherent leading-edge vortex from a sharp-edged UCAV configuration known as 1303 was demonstrated from a high-order wall-resolved LES (WRLES) method at a water-tunnel Reynolds number of approximately 30×10^3. High-order WRLES becomes prohibitively expensive at wind tunnel and flight Reynolds numbers, and this limitation is highly desirable to resolve through faster algorithms and faster computers.

Analysis of a second UCAV configuration, SACCON, demonstrated highly complex and interacting concentrated vortex flows associated with practical spanwise variations of thickness and leading-edge radius. RANS-based CFD provided useful predictions of attached flow (low angle of attack) and initial vortex flows (moderate angles of attack). RANS was unreliable for higher angles of attack with nonlinear breaks in lift and pitching moment; maximum lift coefficient was not well predicted. Considerable variability was demonstrated among well-established codes for the concentrated vortex flowfields at these conditions. Dynamic forced oscillation aerodynamics were also not well predicted and exhibited grid and turbulence model sensitivities.

Analysis of the concentrated vortex flows for an F-16XL aircraft through several programs known as CAWAPI demonstrated progress in RANS and hybrid RANS/LES predictions of the flight measurements, Moderate maneuver conditions with coherent concentrated vortex flows (mild vortex separation) showed good correlation among CFD results (including RANS) and with flight measurements. High angle-of-attack maneuver was more difficult and indicated the possible need of (i) two-equation turbulence models for capturing inboard secondary vortex separation with RANS methods and (ii) hybrid RANS/LES methods with AMR for capturing unsteady vortex interactions on the wing outboard panel. New data for both these vortical flows would be needed for validation and further advancement of the concentrated vortex flow simulation capability.

Simulations for the X-31 demonstrated that details such as flap gaps between leading-edge flap segments can significantly alter the concentrated vortex flows on the wing. The simulations accounting for this effect had better correlation with wind tunnel measurements. Simulations with established CFD codes also demonstrated different vortical flow pattens on the X-31 wing upper surface at maneuver conditions. CFD cannot be considered as reliable at the time of this writing for these vortical flow details. Focused experiments would be needed to resolve this limitation.

Vortex interactions were studied with missile and combat aircraft configurations relevant to industry interests. These studies demonstrated the importance of AMR to resolving the concentrated vortex flow physics for these complex flows. Hybrid RANS/LES simulations of a basic research configuration with a chine forebody and cropped delta wing seem to have captured nonlinear force and moment breaks associated with vortex interaction and vortex breakdown. Inferences were limited due to a lack of surface pressure and flowfield data comparisons. New measurements would be needed to resolve this limitation.

5. Path forward

Based on this review, several opportunities for simulation capability advancement of concentrated vortex flows are identified that balance configuration-based interests and physics-based modelling. First, we consider the context for simulation advancements of concentrated vortex flows, Subsection 5.1. This includes an assessment of computer simulation capacity with projected capacity growth for the following decades. Next, new physical experiments are discussed that could add to our insight and modelling capability for concentrated vortex flows, Subsection 5.2. Finally, we discuss modelling and simulation improvements that would be desirable for advancing our capability to simulate concentrated vortex flows, Subsection 5.3.

These discussions will retain a physics-based perspective to the modelling and simulation of concentrated vortex flows that are important for current and anticipated aircraft needs. In this regard, the authors feel the future work can contribute to the digital engineering and digital transformation interests for the evolution of aircraft design and development. Similar thinking can be found in the technology development roadmap from the CFD Vision 2020 study by Slotnick et al., of 2014 [185].

5.1. Context for simulation advancements

From the findings of this review it seems clear that concentrated vortex flows will continue be an important flow phenomenon to exploit or tolerate for both military and commercial aircraft. The current trend toward digital engineering for vehicle design (e.g., Zimmerman et al. [6], Bone et al. [7], Hale et al. [8]) will increase a need for reliable modelling and simulation capabilities for concentrated vortex flows, and achievement of reliable M&S will, in turn, establish needs for new physical experimentation to guide the M&S development.

CFD has become useful for cruise attached flow analysis and design (i.e., cruise aerodynamics plus slight parametric excursions). Optimization techniques can be employed so long as the problem space stays within the domain of simulation reliability. However, to realize digital engineering goals will require penetration of CFD into the more comprehensive aircraft operating envelope, Fig. 100. In this figure, load factor is shown as a function of equivalent air speed (EAS). It appears to the authors that this penetration has begun for coherent concentrated vortex flows at moderate maneuver conditions (i.e., mild maneuver with

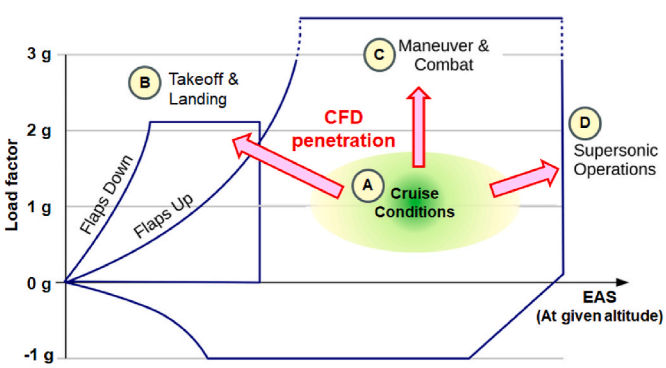

Fig. 100. CFD penetration into performance envelope.

coherent vortices) and this is indicated by the shaded ellipse in Fig. 100. With further departures from this mild maneuvering condition, the flows become complex due to a range of vortical flow physics (e.g., vortex interactions, vortex breakdown, unsteady vortex flows). With these complex vortical flows the confidence in simulation capability diminishes due to a lack of validation or other means to anchor the simulation with physical measurements of the relevant vortical flow physics. In addition, the cost of simulation technology generally increases with departures from cruise conditions. The concept of all-envelope CFD is straightforward, but its realization is a daunting task.

Several instances for the beginning of CFD penetration into the broader flight envelope were found in this survey. The succession of high-lift prediction workshops is beginning to show progress for simulation of concentrated vortex flows in association with transport takeoff and landing conditions. The CAWAPI program has demonstrated that RANS methods can provide useful simulations of coherent and steady concentrated vortices for mild maneuver conditions (Fig. 46). For more aggressive high-angle-of-attack maneuver conditions, CAWAPI demonstrated useful RANS simulations of coherent steady concentrated vortices (Fig. 90) and promising hybrid RANS/LES simulations of semicoherent unsteady concentrated vortices (Fig. 91). The CAWAPI program made less progress for simulating concentrated vortices at high transonic maneuver conditions. The present survey did not find work for simulating concentrated vortex flows at supersonic maneuver conditions. Coherent steady concentrated vortex flows (RANS) and semicoherent unsteady leading-edge vortex flows (hybrid RANS/LES) appear to be two instances of CFD penetration away from cruise conditions.

Both coherent and semicoherent concentrated vortex flows occur in the broader flight envelope (i.e., the white space in Fig. 100), and military aircraft operational requirements can extensively populate this region. An STO meeting in 2022 addressed some needs for the use of CFD in industrial design and analysis of platforms with military relevance [186]. Many of the papers addressed the vortex flows that occur on maneuvering vehicles. Industry interests for the evolution to digital engineering were presented for Airbus Defense and Space (Winkler and Heller [187]), BAE Systems (Leppard [188]), and Lockheed Martin (Smith and McWaters [189]).

Smith and McWaters [189] presented an enlightening contrast of computational and experimental development costs for a fighter aircraft based on requirements from the F-35 development program. Estimates were developed for the compressible flow portion of the full design space for a single-version, non-STOVL (Short Takeoff and Vertical Landing) vehicle to contrast the needed central processing unit (CPU) core hours (i.e., computational user occupancy hours) with the needed wind tunnel user occupancy hours to develop the required data sets of comparable utility. Three levels of CFD complexity, spanning RANS and hybrid RANS/LES techniques, were used to cover the development test matrix. All estimates were based on current technology and methodology and the required computational resources were estimated to be 526 thousand solutions using 17.1 billion core hours at an approximate cost of $596 million dollars. The corresponding wind tunnel test program would have generated about 1.1 million data points and consumed about 2500 user occupancy hours. Using data in the Smith and McWaters report, the cost of this wind tunnel test program could be estimated to be $30 million dollars. The computational program costs about 20 times more than the wind tunnel program, and this presents a significant challenge for the digital transformation interests. A hybrid program that exploits the strengths of supercomputing M&S and wind tunnel data generation appears to be a rational path forward toward realizing portions of the digital engineering vision in the foreseeable future.

This challenge will not be quickly resolved through the growth of supercomputer performance based upon current technology. Moore's law has provided a good estimate of supercomputer performance from the first developments of CFD in the mid-1970s until about 2015 (roughly 40 years). The current growth in supercomputer speed is only about half the nominal performance growth from this CFD development era, Fig. 101, due to fundamental chip restrictions. (See, Spalart and Venkatakrishnan [190].) It now takes twice as long to realize a particular speedup from computer technology compared to the CFD development era, and this has significant consequences for contemporary growth in CFD capability from computer capacity. For example, Table 2 shows that the current speedup over the next 40 years will only be about 2×10^{-6} the speedup realized during the 40 years of CFD development. This results in a 16-year delay to achieve Zflop/s performance and a 26-year delay to achieve Yflop/s performance compared to the conventional Moore's law growth, Table 3.

The digital engineering transformation will not be achievable in a brute force sense but will require careful investment in how it is achieved. A 10-times speedup through advanced numerics (e.g., algorithms, AMR) and advanced computing hardware (e.g., Graphical Processing Units (GPUs)) will help, and should be pursued, but this will still not enable a capability for rapid simulations with advanced computational formulations (e.g., high-order WRLES) to meet prediction needs. Additional techniques (e.g., heterogeneous simulation spaces, surrogate modelling, smart testing) could also help to meet digital engineering goals with the suite of computational formulations available for the present and projected M&S computing environment.

Concentrated vortex flows offer one path for advancement in simulation capability to support digital transformation interests. This vortical flow contributes crucial performance capabilities for both civil and military aircraft at elevated loading conditions. They are exploited over a range of scales from vortex generators through strakes and up to composite airframes. The findings from this survey could contribute to a framework for advancing this simulation capability to meet industry priorities among these many applications. Some of the opportunities for advancement from this survey are summarized in the following sections.

5.2. *Insights from new physical and numerical experiments*

From the survey findings, several gaps can be identified that are candidates for new physical and numerical experimentation. Insights from such studies would be sought to improve modelling and simulation capabilities for concentrated vortex flows and, thus, provide focused advancements toward digital transformation interests.

New physical and numerical campaigns could look to the successful Drag Prediction Workshop (DPW) and High-Lift Prediction Workshop

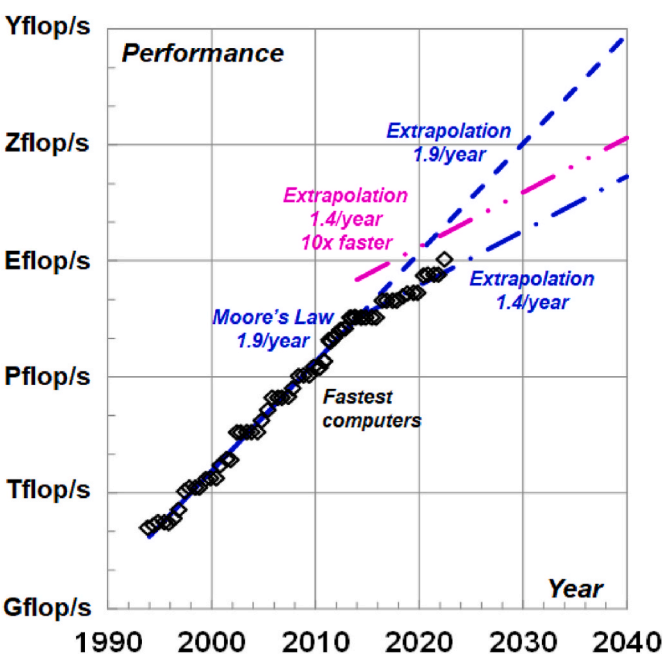

Fig. 101. Computer performance growth.

Table 2
Computer speedup, 40 years.

40 years	rate	Speedup
Moore	1.9	0.20×10^{12}
Moore/2	1.4	0.44×10^{6}
Ratio		2.25×10^{-6}

Table 3
Year to achieve performance.

Performance growth rate	Zflop/s	Yflop/s
Moore	2030	2041
Moore/2	2046	2067
Moore/2 + 10x	2039	2060

(HLPW) series (among others) for organizational and execution guidance. This would include integrated numerical and physical test planning as well as balanced participation from industry, government laboratories, and academia. We also recommend that new campaigns follow as many validation testing practices as is practical. Many of these fall within current testing practices (e.g., model geometry verification, uncertainty quantification) while others entail additional resource investment (e.g., test section flow characterization). Guidance for validation testing can be found in Oberkampf and Roy [12]. The findings are grouped into configuration-based studies, Subsection 5.2.1, and physics-based studies, Subsection 5.2.2.

5.2.1. *Configuration-based studies*

Results from the survey demonstrated a need for unsteady vortex interaction data from the outboard wing panel of the F-16XL aircraft. Unsteady vortex interactions likely contributed to less-than-acceptable prediction of dynamic stability derivatives on the SACCON configuration. Vortex interactions presented challenges also for the configurations studied in the NATO/STO AVT-316 project. Some of these included unsteady flow effects, like vortex breakdown.

It is the authors' observation that there could be a benefit to establishing an open configuration, like the Common Research Model (CRM), targeted toward military combat aircraft interests for concentrated vortex flows. The approach for such an effort could follow the DPW and HLPW examples to arrive at a program to address and prioritize industry interests in a manner to enable the open configuration workshop approach. The authors also observe that a similar argument could be made for an open-forum missile configuration.

It appears that the low-speed concentrated vortex flow application for commercial transports is being addressed by the High-Lift Common Research Model (CRM-HL) configuration within the HLPW activity. Studies thus far have focused on configuration aerodynamics and new studies to measure the nacelle strake vortex strength, trajectory, and persistence would be beneficial toward simulating this important feature.

5.2.2. *Physics-based studies*

Configuration-based studies also play a role in spawning and prioritizing carefully designed physics-based studies. Physics-based studies often enable more detailed computational assessments as well as more detailed flowfield measurements than are practical with a full configuration. When properly designed, these more fundamental studies can be cross-cutting and leveraged to multiple configuration interests. As such, they can play a foundational role to realizing digital engineering interests.

Physics-based studies often take on a unit-problem characterization and are amenable to validation testing principles. We recommend a suite of unit-problem studies that follow from our findings, and several such investigations could include contributions from academia.

5.2.2.1. Primary vortices. Primary vortices are considered here for sharp-edge separation without the onset of vortex breakdown. Blunt-edge vortex separation and vortex breakdown are addressed separately in the subsequent subsections.

Coherent concentrated primary vortices contribute vortex lift to vortex-flow aerodynamics, and these effects have been successfully estimated with modelling and simulation techniques now for many decades and for a variety of slender lifting-surface geometries. However, some of the physics of these coherent vortices merit more detailed assessments. Flow in the core of concentrated vortices can be jet-like or wake-like and serve as conditions leading to vortex breakdown. Instabilities in the vortex sheet can be affected by wing geometry and Reynolds number and can further influence the vortex core flow. Physical tests to quantify these effects could provide data for assessment against M&S techniques to assure that the simulations represent the primary vortex flow prior to the onset of more complex phenomena (e.g., vortex breakdown). The use of AMR to resolve the detailed vortex core flow physics and shear layer instabilities should be explored.

Semicoherent concentrated vortex flows contain greater unsteady content than coherent vortices. The semicoherent vortices are prominent for not-so-slender wings such as UCAV concepts. Several formulations have been used to simulate these unsteady flows, but the survey found only limited evidence that the unsteady simulations are anchored against unsteady experimental findings. Detailed physical experiments could be performed in conjunction with M&S simulations to close this gap for predicting the unsteady content of semicoherent concentrated vortices. The use of AMR to capture this unsteady content should be explored.

5.2.2.2. Secondary vortices. Secondary vortices can affect the strength and position of the primary vortex. The survey found indications that two-equation turbulence models showed better correlation with outboard wing surface pressures, but it also found no evidence of flow details in the boundary layer approaching secondary separation or in the secondary vortex itself. Physical tests with a sharp-edged slender delta wing could provide these data for assessment against M&S simulation techniques. The use of AMR to capture secondary vortex flow physics should be explored.

5.2.2.3. Vortex breakdown. Vortex breakdown limits vortex lift, can cause pitch up and lateral instability, can induce buffet loads on downstream components, and can inhibit vortex persistence flow control. No reliable method for predicting vortex breakdown has been established. The survey results included vortex breakdown in pipe flows that resembled vortex breakdown over a lifting surface. Prior examples can also be found. Detailed physical tests of vortex breakdown in pipe flows that are designed to be relevant to slender-wing aerodynamics and that follow validation testing principles could aid in developing a reliable simulation of vortex breakdown flow physics. The survey also found one example of DNS simulations of vortex breakdown for a pipe flow. Numerical experimentation could be performed to simulate vortex breakdown with reduced order techniques, and resultant improvements could be assessed against new sharp-edged delta wing data, also following validation testing guidelines. The use of AMR to capture vortex breakdown flow physics should be included in these investigations.

5.2.2.4. Vortex persistence. Vortex persistence is used for flow control at two scales of flow physics. One scale has the concentrated vortex flows generated by subcomponents (VGs, μVGs) that interact at the edge or within a boundary layer. The other scale has the concentrated vortex being generated by a component (nacelle strake, fuselage strake) for interaction with downstream portions of the airframe. The survey findings were limited to device-on/device-off effects on aggregate configuration aerodynamics.

Detailed physical experiments could be performed to document the concentrated vortex strength, trajectory, and persistence for these application interests on simplified but representative geometries. The studies could include (i) low-speed VG and μVG vortex flows, (ii) transonic VG vortex flows, (iii) low-speed nacelle strake vortex flows, (iv) low-speed body strake vortex flows, and (v) transonic body strake vortex flows. Low-speed nacelle strake vortex studies should include quantification of the trailing-wake counterrotating vortex and its effects on the primary strake vortex persistence. Physical testing would follow validation testing practices. The use of AMR to capture vortex persistence flow physics should be included in these investigations.

5.2.2.5. Incipient separation, blunt-leading-edge vortex separation onset. Incipient separation occurs directly upstream of concentrated vortex separation onset from a blunt leading edge. This flow topology is thin and occurs near the curved leading region such that it defies measurement for detailed flow properties with current technology. Survey results also showed detailed compressible flow physics about a blunt leading edge from a WRLES simulation. It is recommended that incipient separation flow physics be studied with numerical experimentation based upon higher-order WRLES techniques, much as was done with the blunt-leading-edge compressible flow physics study. Higher-order WRLES techniques are expensive and Reynolds number limited, but they could be used as a baseline to explore modelling improvements from more affordable lower-order numerical techniques.

5.2.2.6. Inner vortex. The inner vortex is a new vortical structure that occurs in association with blunt-leading-edge and blunt-side-edge vortex separation. It initiates from the incipient separation region and persists downstream over the wing. It was found experimentally in the AVT-113 Vortex Flow Experiment II tests including the precursor NASA NTF tests and has been simulated with WRLES, hybrid RANS/LES, and RANS formulations. However, there has been no validation between physical experiment and simulation for the inner vortex. Detailed physical experiments could be performed in conjunction with M&S assessments to add understanding of how well the M&S formulations are predicting the inner vortex properties. The inner vortex can be small, and the use of AMR to capture inner vortex flow physics should be explored.

5.2.2.7. Vortex hysteresis. Vortex hysteresis affects dynamic maneuver in terms of forces, moments, and stability and control. The survey did not find results quantifying CFD predictive capability for concentrated vortex flow hysteresis. Dynamic physical experiments with simple configurations, such as a sharp-edge delta wing, could be performed to quantify the hysteretic concentrated vortex flow properties. Conditions of the studies should include concentrated vortex flows without and with vortex breakdown.

5.3. Modelling and simulation process improvements

We have chosen three categories for discussion of modelling and simulation process improvements. First, we will discuss hardware improvements for the computing infrastructure, Subsection 5.3.1. Next, we discuss several classes of software improvements in Subsection 5.3.2. Finally, we discuss other techniques to realize advanced M&S capability within current hardware and software capabilities, Subsection 5.3.3.

5.3.1. Hardware

The computing environment with conventional processor technology was summarized in Fig. 101 with several projections based upon variants of Moore's law. Growth in computer speed has slowed, and one alternate approach to this restriction is to exploit GPUs for general CFD applications. Extension of CFD solvers from CPU to GPU processing is a significant task, and this has slowed migration of established solvers to this computing domain. None the less, a sustained effort has established GPU processing capability with the NASA research and application code FUN3D. Assessments have shown speedups from four to thirty times that of CPU processing and demonstrated that these speeds can be achieved for practical applications with an advanced Navier-Stokes code that supports an external user community [191]. Development is also underway to provide GPU processing within the established CREATE-AV software system to include both fixed-wing (Kestrel) and rotary-wing (Helios) application domains. Plans are also in place to include GPU processing capability in the new CODA (CFD for ONERA, DLR, and Airbus) software system being developed in Europe. (CPU processing from this new system has recently been published by Volpiani et al. [192] in 2023 for a CRM DPW transonic application.) GPU processing availability will help offset the reduced growth in CPU processing shown in Fig. 101. The survey did not find any applications of GPU-based solvers for concentrated vortex flows, and we recommend this be undertaken to quantify the performance speed up for this application.

5.3.2. Software

5.3.2.1. Numerical modelling. Both the resolution of flow scales and long compute times will remain challenges for the foreseeable future. Concentrated vortex flows are one application focus that would benefit from numerical modelling advancements. Higher-order discretization in space and time can help and should be pursued in codes suitable to industry-scale problems. CODA may serve as one example of what can be achieved from a fresh start, and initial assessments have demonstrated a factor of three or more in speedup [193]. Findings from this survey imply that AMR may effectively be a requirement for resolving concentrated vortex flows. Effective use of AMR for resolving unsteady concentrated vortex flows can be traced back at least to 2003 (Morton [97]) with the Cobalt code, Fig. 53. This capability was carried forward into the CREATE-AV software system for both Kestrel and Helios codes. Other examples in this report were shown from the NASA FUN3D code, the LEMMA Niceflow code, and the CNRS ISIS-CFD code. These methods, as well as others, are showing promise for concentrated vortex flow simulations. Comparisons among AMR methods for targeted concentrated vortex flow topics could help advance the AMR technology for effective use of grids to resolve vortical flow physics while containing overall problem size. The targeted concentrated vortex flows could include primary and secondary vortices, burst and unburst vortices, coherent and semicoherent vortex states, various vortex interactions, and so forth. Several of these were mentioned in the preceding sections.

5.3.2.2. Physical modelling. Turbulence models have been developed for decades, often with a view toward wall-bounded flows or toward free-shear-layer flows. Concentrated vortex flows have both these features tightly coupled as well as off-body viscous boundary-layer scale flows in the vortex core. Smooth-surface separation from nonequilibrium boundary layers contribute to blunt-leading-edge primary vortex separation as well as secondary vortex separation. Modelling and simulation of concentrated vortex flows could benefit from a reassessment of established turbulence modelling techniques for the physics of these vortical flows. One example has been shown by Subbian and Radespiel et al. [194] in 2018, and more could be done. New approaches such as machine learning (Singh et al. [195], 2017, Duraisamy et al. [196], 2019) are being explored to advance turbulence modelling. However, the work does not include concentrated vortex flow assessments and could be leveraged toward this purpose. Advanced formulations such as WRLES could also be explored for training reduced-physics methods that are capable of simulating conditions relevant to industry interests to approximate the advanced formulation physics. Finally, higher-fidelity scale-resolving methods (e.g., WMLES) are beginning to make inroads for complex flow analysis such as in HLPW-4. Findings from these activities could be leveraged for focused assessments of

concentrated vortex flow topics.

5.3.3. Other techniques

Several additional techniques can be exploited to help realize digital engineering objectives while hardware and software improvements are under development. Surrogate methods offer an approach to populating a design space using a restricted number of high-fidelity (and expensive) simulations. One approach has been given by Morton [197] in 2022 for the surrogate modelling being incorporated into the CREATE-AV simulation system. Heterogeneous database management can also contribute to this approach to account for different fidelity simulations within a particular design space. Smart testing can also focus method development work for targeted system design requirements. One approach based on a model validation hierarchy has recently been given by Luckring et al. [198] in conjunction with Shaw et al. [199]. These techniques are general, and they could be applied to concentrated vortex flow interests.

5.4. Summary comments

The path forward recommendations identify specific opportunities from various research specializations (physical testing, numerical developments, etc.) that could lead to enhanced modelling and simulation of concentrated vortex flows. It is the authors' position that any prioritization among these research activities would be informed by configuration-based aerodynamic needs. These findings also present opportunities to advance digital engineering capabilities as regards concentrated vortex flows. A recent treatment of digital engineering opportunities and challenges from a digital twin perspective has been given by Wilcox et al. [200] in 2023. It appears to the authors that the path forward recommendations are consistent with these digital twin findings and could provide targeted opportunities to exercise some of the digital twin thinking.

6. Concluding remarks

Concentrated vortex flows are exploited for both civil and military aircraft aerodynamics. These uses span a wide fluid dynamic range from sub-boundary-layer flows to integrated airframe flows. The uses also cover a variety of vehicle performance conditions including takeoff and landing, cruise, and high angle-of-attack maneuver. The concentrated vortex applications address both flow control and manuever lift effects. It is desirable to have reliable CFD predictive capabilities to address these interests.

This article focused first on the airframe motivations for use of concentrated vortex flows, and a historical perspective was adopted for this discussion. Fundamental fluid mechanics of concentrated vortex flows were reviewed. These are the underpinning features that are stressed in different ways depending on a particular application interest. The hierarchy of CFD formulations spanning DNS to RANS methods was also reviewed with a view toward concentrated vortex flow applications.

Findings from a literature survey demonstrated both capabilities and gaps in prediction of concentrated vortex flow effects. Significant contributions were found from research codes as well as from production software systems and predictions spanned RANS to DNS methods. Many results demonstrated encouraging predictions of integrated effects and trends. There was, in general, a lack of evidence for predicting the concentrated vortex flow features critical to these application interests. The literature database was extensive, and the authors feel the findings are representative of the present state of the art for concentrated vortex flow aerodynamic predictions.

Some recommendations for future work were provided to improve the confidence in simulation of the concentrated vortex flows of interest for airframe applications. These improvements could contribute to digital transformation interests for expanding the digital engineering capability to a broader portion of aircraft operating envelopes.

CRediT authorship contribution statement

James M. Luckring: Writing – original draft. **Arthur Rizzi:** Writing – original draft.

Declaration of competing interest

I declare that there are no financial and personal relationships with other people or organizations that could inappropriately influence (bias) this work.

Data availability

No data was used for the research described in the article.

Acknowledgements

Dr. Luckring appreciates the support for participation in this work from the Configuration Aerodynamics Branch at the NASA Langley Research Center. Prof. Rizzi appreciates the support the Royal Institute of Technology has given him as emeritus professor. Both authors wish to thank Ms. Dorothy Notarnicola, Ms. Sarah Schwaner, and Ms. Melissa Kondysar at the NASA Langley Technical Library for sustained literature research support, and the KTH library for access to its online search facilities and digital archives.

References

[1] J.M. Luckring, The discovery and prediction of vortex flow aerodynamics, Aeronaut. J. 123 (1264) (2019 June) 729–804.
[2] A. Rizzi, Separated and vortical flow in aircraft aerodynamics: a CFD perspective, Aeronaut. J. 127 (2023) 1065–1103.
[3] AGARD. Vortex Flow Aerodynamics, AGARD CP-494. NATO, AGARD, 1991.
[4] D. Hummel, On the vortex formation over a slender wing at large angles of incidence, AGARD CP-247, Paper 15. NATO (1978).
[5] D. Lovell, Military Vortices. RTO-MP-069(I), 2003. Paper KN1. NATO.
[6] P. Zimmerman, T. Gilbert, F. Salvatore, Digital engineering transformation across the department of Defense, Journal of Defense Modeling and Simulation 16 (4) (2019) 325–338.
[7] M.A. Bone, M.R. Blackburn, D.H. Rhodes, D.N. Cohen, J.A. Guerrero, Transforming systems engineering through digital engineering, Journal of Defense Modeling and Simulation 16 (4) (2019) 339–355.
[8] J.P. Hale, P. Zimmerman, G. Kukkala, J. Guerrero, P. Kobryn, B. Puchek, et al., Digital Model-Based Engineering: Expectations, Prerequisites, and Challenges of Infusion, NASA, 2017. NASA/TM 2017-219633.
[9] S.M. Hitzel, R. Osterhuber, Enhanced maneuverability of a delta-canard combat aircraft by vortex flow control, AIAA Journal of Aircraft 55 (3) (2018) 1090–1102.
[10] AIAA, Guide for the Verification and Validation of Computational Fluid Dynamics Simulations, American Institute of Aeronautics and Astronautics, 1998. Report No.: AIAA-G-077-1998.
[11] ASME, Guide for Verification and Validation in Computational Solid Mechanics, ASME, 2006. Report No.: ASME V&vols. 10-2006.
[12] W.L. Oberkampf, C.J. Roy, Verification and Validation in Scientific Computing, Cambridge University Press, 2010.
[13] E.C. Polhamus, Private Communication, 1974.
[14] D. Küchemann, Report on the I.U.T.A.M. symposium on concentrated vortex motions in fluids, J. Fluid Mech. 21 (1) (1965) 1–20.
[15] L.K. Loftin, Quest for Performance: the Evolution of the Modern Aircraft, NASA, 1985. NASA SP-468.
[16] W.H. Cook, The Road to the 707, TYC Publishing Co, 1991.
[17] C. Furlong, J.G. McHugh, Analysis of the Low-Speed Longitudinal Characteristics of Swept Wings at High Reynolds Number, NACA, 1952. NACA Report 1339.
[18] J. Weil, W.H. Gray, Recent design studies directed toward elimination of pitch-up. NACA RM L53123c, NACA, 1953.
[19] J.C. Lin, Review of research on low-profile vortex generators to control boundary-layer separation, Prog. Aero. Sci. 38 (4) (2002) 389–420.
[20] A. Jirásek, Vortex Generator Modeling and its Application to Optimal Control of Airflow in Inlet. TRITA-AVE 2006:66, KTH Royal Institute of Technology, 2006.
[21] H.D. Taylor, The Elimination of Diffuser Separation by Vortex Generators. Report R-4012-3, United Aircraft Corporatrion, 1947.
[22] V.M. Ganzer, Aerodynamic Development of the XB-47 Airplane. Part II - Development of Model 450 up to June 1947, D-7824A. Boeing, 1947.
[23] H.H. Pearcey, Shock induced separation and its prevention by design and boundary-layer control, in: Boundary Layer and Flow Control, vol. 2, Pergamon Press, New York, 1961, pp. 1166–1344.

[24] ESDU. Vortex generators for control of shock-induced separation, Part 1: Introduction and aerodynamics. Transonic Data Memorandum 93024.
[25] K.S. Bohannon, Passive Flow Control on Civil Aircraft Flaps Using Sub-boundary Layer Vortex Generators in the AWIATOR Programme. AIAA 2006-2858, AIAA, 2006.
[26] M.J. Abzug, E.E. Larrabee, Airplane Stability and Control: A History of the Technologies that Made Aviation Possible, Cambridge University Press, 1997.
[27] R.S. Shevell, R.D. Schaufele, R.L. Roensch, Stall control device for swept wings, US Patent 3 (1968), 370,810.
[28] R. Kerker, D. Wells, Inventors; Liftvanes. USA Patent 3,744,745, 1973 Jul.
[29] R.S. Shevell, Aerodynamic anomalies: can CFD prevent or correct them? AIAA Journal of Aircraft 23 (8) (1986) 641–649.
[30] J.F. Campbell, J.R. Chambers, Patterns in the sky. NASA SP-514, NASA, 1994.
[31] D. Küchemann, The Aerodynamic Design of Aircraft, Pergamon Press, 1978.
[32] M.G. Hall, On the vortex associated with flow separation from a leading edge of a slender wing, RAE TN Aero 2629 (1959).
[33] R.C. Nelson, A. Pelletier, The unsteady aerodynamics of slender wings and aircraft undergoing large amplitude maneuvers, Prog. Aero. Sci. 39 (2003) 185–248.
[34] M.G. Hall, A theory for the core of a leading-edge vortex, J. Fluid Mech. 11 (2) (1961) 209–228.
[35] K. Stewartson, M.G. Hall, The inner viscous solution for the core of a leading-edge, J. Fluid Mech. 15 (1963) 306–318.
[36] S.N. Brown, The compressible inviscid leading-edge vortex, J. Fluid Mech. 22 (1) (1965) 17–32.
[37] Y. Le Moigne, Adaptive Mesh Refinement and Simulations of Unsteady Delta-Wing Aerodynamics, PhD dissertation, KTH Royal Institute of Technology, 2004. Report No.: TRITA-AVE 2004:17.
[38] D.I. Greenwell, Pitfalls in the Interpretation of Delta Wing Flow Visualisation, NATO, RTO, 2003. RTO-MP-069(I).
[39] J.M. Luckring, Reynolds Number, Compressibility, and Leading-Edge Bluntness Effects on Delta-Wing Aerodynamics, ICAS, 2004. Paper 2004–0414.
[40] J. Chu, J.M. Luckring, Experimental Surface Pressure Data Obtained on 65° Delta Wing across Reynolds Number and Mach Number Ranges, 1996. NASA TM-4647, vols. 1-4.
[41] E.C. Polhamus, A Survey of Reynolds Number and Wing Geometry Effects on Lift Characteristics in the Low Speed Stall Region. NASA CR-4745, 1996.
[42] M.R. Visbal, D.J. Garmann, Dynamic stall of a finite-aspect-ratio wing, AIAA J. 57 (3) (2019) 962–977.
[43] A. Rizzi, J. Oppelstrup, Aircraft Aerodynamic Design with Computational Software, Cambridge University Press, 2021.
[44] D.I. Poll, Spiral vortex flow over a swept-back wing, Aeronaut. J. 90 (895) (1986) 185–199.
[45] S.M. Hitzel, O.J. Boelens, M. Rooij, A. Hövelmann, Vortex development on the AVT-183 diamond wing configuration – numerical and experimental findings, Aero. Sci. Technol. 57 (2016) 90–102.
[46] E.R. Keener, Flow-Separation Patterns on Symmetric Forebodies, 1986. NASA TM 86016.
[47] E.C. Polhamus, A Concept of the Vortex Lift of Sharp-Edged Delta Wings Based on a Leading-Edge Suction Analogy, NASA TN D-3767, 1966.
[48] U. Brennenstuhl, D. Hummel, Vortex foemation over double-delta wings, ICAS (1982) paper 82-6.6.3 1133-1146.
[49] D.S. Miller, R.M. Wood, Leeside flows over delta wings at supersonic speeds, AIAA Journal of Aircraft 21 (9) (1984) 680–686.
[50] J.M. Brandon, J.B. Hallissy, P.W. Brown, J.E. Lamar, In-Flight Flow Visualization Results of the F-106B with a Vortex Flap. RTO-MP-069(I), NATO, 2003. Paper 43.
[51] J.B. Hallissy, W.E.J. Schoonover, T.D.J. Johnson, J.M. Brandon, Wind-Tunnel Investigation of the Multiple Vortex System Observed in Flight Tests of the F-106B Vortex Flap Configuration, NASA, 1993. NASA TP-3322.
[52] C. Breitsamter, Unsteady flow phenomena associated with leading-edge vortices, Prog. Aero. Sci. 44 (1) (2008) 48–65.
[53] N.C. Lambourne, D.W. Bryer, The bursting of leading-edge vortices - some observations and discussion of the phenomenon, ARC R&M 3282 (1962).
[54] S. Leibovich, The structure of vortex breakdown, Annu. Rev. Fluid Mech. 10 (1978) 221–246.
[55] Jr WH. Wentz, D.L. Kohlman, Vortex breakdown on slender sharp-edged wings, AIAA Journal of Aircraft 8 (3) (1971) 156–161.
[56] M. Menke, H. Yang, I. Gursul, Experiments on the unsteady nature of vortex breakdown over delta wings, Exp. Fluid 31 (9) (1999) 262–272.
[57] T. Sarpkaya, Vortex breakdown in swirling conical flows, AIAA J. 9 (9) (1971) 1792–1799.
[58] S. Leibovich, Vortex stability and breakdown: survey and extension, AIAA J. 22 (9) (1984) 1192–1206.
[59] J.H. Faler, S. Leibovich, Disrupted states of vortex flow and vortex breakdown, Phys. Fluids 20 (1977) 1385–1400.
[60] J.H. Faler, S. Leibovich, An experimental map of the internal structure of a vortex breakdown, J. Fluid Mech. 86 (1978) 313–335.
[61] S. Görtz, Realistic Simulations of Delta Wing Aerodynamics Using Novel CFD Methods, PhD dissertation, KTH Royal Institute of Technology, 2005. Report No.: TRITA-AVE 2005:01.
[62] M.G. Hall, Vortex breakdown, Annu. Rev. Fluid Mech. 4 (1972) 195–218.
[63] A. Rizzi, J.M. Luckring, Historical development and use of CFD for separated flow simulations relevant to military aircraft, Aero. Sci. Technol. 117 (2021) 1–42.
[64] R.E. Gordnier, M.R. Visbal, I. Gursul, Z. Wang, Computational and experimental investigation of a nonslender delta wing, AIAA J. 47 (8) (2009) 1811–1825.
[65] I. Gursul, R. Gordnier, M. Visbal, Unsteady aerodynamics of nonslender delta wings, Prog. Aero. Sci. 41 (2005) 515–557.
[66] M.R. Visbal, D. Gaitonde, High-order accurate methods for complex unsteady subsonic flows, AIAA J. 37 (1999) 1231–1239.
[67] M. Menke, I. Gursul, Unsteady nature of leading edge vortices, Phys. Fluids 9 (10) (1997) 2960–2966.
[68] R. Gordnier, M.R. Visbal, Unsteady vortex structure over a delta wing, AIAA Journal of Aircraft 31 (1) (1994) 243–248.
[69] O.K. Redinoitis, H. Stapountzis, D.R. Telionis, Periodic vortex shedding over delta wings, AIAA J. 31 (9) (1993) 1555–1561.
[70] I. Gursul, Unsteady flow phenomena over delta wings at high angle of attack, AIAA J. 32 (2) (1994) 225–231.
[71] I. Gursul, W. Xie, Buffeting flows over delta wings, AIAA J. 37 (1) (1999) 58–65.
[72] D. Rockwell, Three Dimensional Flow Structure on Delta Wings at High Angle-Of-Attack: Experimental Concepts and Issues. AIAA 1993-0550, AIAA, 1993.
[73] H. Xiaoa, P. Cinnellab, Quantification of model uncertainty in RANS simulations: a review, Prog. Aero. Sci. 108 (2019) 1–31.
[74] D.C. Wilcox, Turbulence Modeling for CFD, third ed., D C W Industries, 2006.
[75] S.M. Hosseini, R. Vinuesa, P. Schlatter, A. Hanifi, D.S. Henningson, Direct numerical simulation of the flow around a wing section at moderate Reynolds number, Int. J. Heat Fluid Flow 61 (Part A) (2016) 117–128.
[76] S. Ghosal, An analysis of numerical errors in large-eddy simulations of turbulence, J. Comput. Phys. 125 (1996) 187–206.
[77] N.J. Georgiadis, D.P. Rizzetta, C. Fureby, Large-eddy simulation: current capabilities, recommended practices, and future research, AIAA J. 48 (8) (2010) 1772–1784.
[78] D. Garmann, M. Visbal, Investigation of the Unsteady Tip Vortex Structure on a NACA0012 Wing at Fixed Incidence. AIAA 2017-1002, AIAA, 2017.
[79] D. Garmann, M. Visbal, Analysis of tip vortex near-wake evolution for stationary and oscillating wings, AIAA J. 55 (8) (2017) 2686–2702.
[80] R.M. Hall, D.G. Murri, G.E. Erickson, D.F. Fisher, D.W. Banks, W.R. Lanser, Overview of HATP Experimental Aerodynamics Data for the Baseline F/A-18 Configuration, NASA, 1996. NASA TM-112360.
[81] F. Ghaffari, J.M. Luckring, J.T. Thomas, B.L. Bates, Navier-Stokes solutions about the F/A-18 forebody-leading-edge extension configuration, AIAA Journal of Aircraft 27 (9) (1990) 737–748.
[82] F. Ghaffari, J.L. Luckring, J.T. Thomas, B.L. Bates, R.T. Biedron, Multiblock Navier-Stokes solutions about the F/A-18 wing-LEX-fuselage configuration, AIAA Journal of Aircraft 30 (3) (1993) 293–303.
[83] J.E. Lamar, C.J. Obara, B.D. Fisher, D.F. Fisher, Flight, wind-tunnel, and computational fluid dynamics comparison for cranked Arrow wing (F-16XL-1) at subsonic and transonic speeds, NASA TP (2001) 2001–210629.
[84] RTO, Understanding and Modeling Vortical Flows to Improve the Technology Readiness Level for Military Aircraft, RTO-TR-AVT-113. NATO, RTO, 2009.
[85] A. Rizzi, O. Boelens, A. Jirásek, K. Badcock, What Was Learned from Numerical Simulations of F-16XL (CAWAPI) at Flight Conditions, vols. 2007–683, AIAA Paper, 2007.
[86] A. Rizzi, A. Jirásek, J.E. Lamar, S. Crippa, K.J. Badcock, O.J. Boelens, Lessons learned from numerical simulations of the F-16XL aircraft at flight conditions, J. Aircraft 46 (2) (2009) 423–441.
[87] J. Larsson, S. Kawai, J. Bodart, I. Bermejo-Moreno, Large eddy simulation with modeled wall-stress: recent progress and future directions, Mechanical Engineering Reviews 3 (1) (2016) 1–23.
[88] P.R. Spalart, W.H. Jou, M. Strelets, S.R. Allmaras, Comments on the feasibility of LES for wings, and on a hybrid RANS/LES approach. Advances in DNS/LES, 1st AFOSR Int. Conf. on DNS/LES, 1997.
[89] U. Piomelli, E. Balaras, Wall-layer models for large-eddy simulations, Annu. Rev. Fluid Mech. 34 (2002) 349–374.
[90] C.C. Kiris, A.S. Ghate, O.M. Browne, J. Slotnick, J. Larsson, HLPW-4/GMGW-3: Wall-Modeled LES and Lattice-Boltzmann Technology Focus Group Workshop Summary, 2022. AIAA 2022-3294.
[91] C.L. Rumsey, J.P. Slotnick, C. Woeber, HLPW-4/GMGW-3: Overview and Workshop Summary, 2022. AIAA 2022-3295.
[92] J.R. Forsythe, K.D. Squires, K.E. Wurtzler, P.R. Spalart, Detached-eddy simulation of the F-15E at high Alpha, AIAA Journal of Aircraft 41 (2) (2004) 193–200.
[93] M. Han, O. Ryozo, Large-Eddy Simulation Based on the Lattice Boltzmann Method for Built Environment Problems, Springer Nature Singapore, 2023.
[94] S. Chen, G.D. Doolen, Lattice Boltzmann method for fluid flows, Annu. Rev. Fluid Mech. 30 (1) (1998) 329–364.
[95] M. Tomac, A. Rizza, D. Charbonnier, J.B. Vos, A. Jirásek, S.H. Peng, et al., Unsteady Aero-Loads from Vortices Shed on A320 Landing Gear Door: CFD Compared to Flight Tests. AIAA 2016-0803, AIAA, 2016.
[96] S. Morton, Detached-eddy simulations of vortex breakdown over a 70-degree delta wing, AIAA Journal of Aircraft 46 (3) (2009) 746–755.
[97] S. Morton, High Reynolds Number DES Simulations of Vortex Breakdown over a 70 Degree Delta Wing, vols. 2003–4217, AIAA, 2003.
[98] L.A. Schiavetta, O.J. Boelens, S. Crippa, R.M. Cummings, W. Fritz, K.J. Badcock, Shock effects on delta wing vortex breakdown, AIAA Journal of Aircraft 46 (3) (2009) 903–914.
[99] J.T. Thomas, S.L. Taylor, W.K. Anderson, Navier-Stokes Computations of Vortical Flows over Low Aspect Ratio Wings. AIAA 1987-0207, AIAA, 1987.
[100] M.R. Visbal, R.E. Gordnier, On the Structure of the Shear Layer Emanating from a Swept Leading Edge at Angle of Attack, 2003. AIAA 2003-4016.
[101] J.M. Luckring, Initial experiments and analysis of blunt-edge vortex flows for VFE-2 configurations at NASA Langley, USA, Aero. Sci. Technol. 24 (1) (2013) 10–21.

[102] D.J. Hummel, The international vortex flow experiment 2 (VFE-2): background, objectives and organization, Aero. Sci. Technol. 24 (2013) 1–9.
[103] Numerous, Special issue: VFE-2, Aero. Sci. Technol. 24 (1) (2013) 1–88.
[104] J.M. Luckring, D. Hummel, What was learned from the new VFE-2 experiments? Aero. Sci. Technol. 24 (1) (2013) 77–88.
[105] J.M. Luckring, Reynolds Number and Leading-Edge Bluntness Effects on a 65° Delta Wing, 2002. AIAA 2002-0419.
[106] D. Hummel, Private Communication, 2002.
[107] J.M. Luckring, O.J. Boelens, C. Breitsamter, A. Hövelmann, F. Knoth, D.J. Malloy, et al., Objectives, approach, and scope for the AVT-183 diamond-wing investigations, Aero. Sci. Technol. 57 (2016) 2–17.
[108] N.T. Frink, M. Tomac, A. Rizzi, Collaborative study of incipient separation on 53o-swept diamond wing, Aero. Sci. Technol. 57 (2016) 76–89.
[109] STO, Reliable Prediction of Separated Flow Onset and Progression for Air and Sea Vehicles, STO-TR-AVT-183. NATO, STO, 2017.
[110] Numerous. Special issue, Diamond wing aerodynamics, Aero. Sci. Technol. 57 (2016) 1–118.
[111] A. Hövelmann, F. Knoth, C. Breitsamter, AVT-183 diamond wing flow field characteristics Part 1: varying leading-edge roughness and the effects on flow separation onset, Aero. Sci. Technol. 57 (2016) 18–30.
[112] A. Hövelmann, M. Grawunder, A. Buzica, C. Breitsamter, AVT-183 diamond wing flow field characteristics Part 2: experimental analysis of leading-edge vortex formation and progression, Aero. Sci. Technol. 57 (2016) 31–42.
[113] S. Deck, J.M. Luckring, Zonal Detached Eddy Simulation (ZDES) of the flow around the AVT-183 diamond wing configuration, Aero. Sci. Technol. 57 (2016) 43–51.
[114] A. Buzica, C. Breitsamter, Turbulent and transitional flow around the AVT-183 diamond wing, Aero. Sci. Technol. 92 (9) (2019) 520–535.
[115] M.R. Visbal, D.J. Garmann, Effect of sweep on dynamic stall of a pitching finite-aspect-ratio wing, AIAA J. 57 (8) (2019) 3274–3289.
[116] S.I. Benton, M.R. Visbal, Effects of compressibility on dynamic-stall onset using large-eddy simulation, AIAA J. 58 (3) (2020) 1194–1205.
[117] A. Schütte, Numerical investigations of vortical flow on swept wings with round leading edges, AIAA Journal of Aircraft 54 (2) (2017) 572–601.
[118] D. Garmann, M. Visbal, High-fidelity simulations of afterbody vortex flows, AIAA J. 57 (9) (2019) 3980–3990.
[119] D.S. Bulathsinghala, R. Jackson, Z. Wang, I. Gursul, Afterbody vortices of axisymmetric cylinders with a slanted base, Exp. Fluid 58 (60) (2017) 1–24.
[120] F. Novak, T. Sarpkaya, Turbulent vortex breakdown at high Reynolds numbers, AIAA J. 38 (5) (2000) 825–834.
[121] O. Lucca-Negro, T. O'Doherty, Vortex breakdown: a review, Prog. Energy Combust. Sci. 27 (2001) 431–481.
[122] J.N. Sorensen, I.V. Naumov, V.L. Okulov, Multiple helical modes of vortex breakdown, J. Fluid Mech. 683 (2011) 430–441.
[123] S. Zhang, H. Zhang, C.W. Shu, Topological structure of shock induced vortex breakdown, J. Fluid Mech. 639 (2009) 343–372.
[124] Z. Rusak, D. Lamb, Prediction of vortex breakdown in leading-edge vortices above slender delta wings, J. Aircraft 36 (4) (1999) 659–667.
[125] S. Wang, Z. Rusak, On the stability of an axisymmetric rotating flow in a pipe, Phys. Fluids 8 (4) (1996) 1007–1016.
[126] M. Jones, A. Hashimoto, Y. Nakamura, Criteria for vortex breakdown above high-sweep delta wings, AIAA J. 47 (10) (2009) 2306–2320.
[127] RTO, Vortex Breakdown over Slender Delta Wings, TR-AVT-080. NATO, RTO, 2009.
[128] A.M. Mitchel, P. Molton, D. Barberis, J. Delery, Oscillation of vortex breakdown location and control of the time-averaged location by blowing, AIAA J. 38 (5) (2000) 793–803.
[129] A. Mitchel, S. Morton, P. Molton, Y. Guy, Flow control of vortical structures and vortex breakdown over slender delta wings, RTO MP-069(I), Paper 20. NATO, RTO (2003).
[130] M.S. Son, J.H. Sa, S.H. Park, Y.H. Byun, K.W. Cho, Delayed detached-eddy simulation of vortex breakdown over a 70° delta wing, J. Mech. Sci. Technol. 29 (8) (2015) 3205–3213.
[131] L. Shen, Cy Wen, Oscillations of leading-edge vortex breakdown locations over a delta wing, AIAA J. 56 (6) (2018) 2113–2118.
[132] T. Nonomura, H. Fukumoto, Y. Ishikawa, K. Fujii, Mach-number effects on vortex breakdown in subsonic flows over delta wings, AIAA J. 51 (9) (2013) 2281–2285.
[133] I.M. Kalkhoran, M.K. Smart, Aspects of shock wave-induced vortex breakdown, Progress in Aerospce Sciences 36 (2000) 63–95.
[134] R.E. Gordnier, M.R. Visbal, Compact difference scheme applied to simulation of low-sweep delta wing flow, AIAA J. 43 (8) (2005) 1744–1752.
[135] I. Gursul, Review of unsteady vortex flows over slender delta wings, AIAA Journal of Aircraft 42 (2) (2005) 299–319.
[136] B. Yaniktepe, D. Rockwell, Flow structure on a delta wing of low sweep angle, AIAA J. 42 (3) (2004) 513–523.
[137] G. Taylor, I. Gursul, Buffeting flows over a low-sweep delta wing, AIAA J. 42 (9) (2004) 1737–1745.
[138] M. Visbal, Onset of vortex breakdown above a pitching delta wing, AIAA J. 32 (8) (1994) 1568–1575.
[139] M. Hadidoolabi, H. Ansarian, Computational investigation of vortex structure and breakdown over a delta wing at supersonic pitching maneuver, J. Braz. Soc. Mech. Sci. Eng. 40 (78) (2018) 1–17.
[140] I. Gursul, I. Yang, Vortex breakdown over a pitching delta wing, J. Fluid Struct. 9 (1995) 571–583.
[141] K.J. Forster, T.R. White, Numerical investigation into vortex generators on heavily cambered wings, AIAA Jiurnal 52 (5) (2014) 1059–1071.
[142] M. Meunier, V. Brunet, High-lift devices performance enhancement using mechanical and air-jet vortex generators, AIAA Journal of Aircraft 45 (6) (2008) 2049–2061.
[143] F. Moen, J. Dandoi, Optimization of passive flow control devices of a slatless high-lift configuration, AIAA Journal of Aircraft 53 (1) (2016) 189–201.
[144] Y. Ito, K. Yamamoto, K. Kusunose, K. Nakakita, M. Murayama, K. Tanaka, Effect of vortex generators on transonic swept wings, AIAA Journal of Aircraft 53 (6) (2016) 1890–1904.
[145] N. Namura, K. Shimoyama, S. Obayashi, Y. Ito, S. Koike, K. Nakakita, Multipoint design optimization of vortex generators on transonic swept wings, AIAA Journal of Aircraft 56 (4) (2019) 1291–1302.
[146] M. Zastawny, Numerical simulation of wing vortex generators – methodologies and validation, Aeronaut. J. 120 (1226) (2016) 627–650.
[147] E.H. Hirschel, A. Rizzi, C. Breitsamter, W. Staudacher, Separated and Vortical Flow in Aircraft Wing Aerodynamics, Springer-Verlag, Berlin, 2021.
[148] C.L. Rumsey, S.X. Ying, Prediction of high lift: review of present CFD capability, Prog. Aero. Sci. 38 (2002) 145–180.
[149] H. Hansen, P. Thiede, F. Moens, Overview about the European High Lift Research Programme EUROLIFT, AIAA Paper 2004-767. AIAA, 2004.
[150] R. Rudnik, H. von Geyr, The European High Lift Project EUROLIFT II – Objectives, Approach, and Structure, AIAA Paper 2007-4296. AIAA, 2007.
[151] J.P. Slotnick, J.A. Hannon, M. Chaffin, Overview of the First AIAA CFD High Lift Prediction Workshop, AIAA Paper 2011-862. AIAA, 2011.
[152] M. Koklu, J.C. Lin, J.A. Hannon, L.P. Melton, M.Y. Andino, K.B. Paschal, et al., Investigation of the nacelle/pylon vortex system on the high-lift common research model, AIAA J. 59 (9) (2021) 3748–3763.
[153] H. von Geyr, N. Schade, J.W. van der Burg, P. Eliasson, S. Esquieu, CFD Prediction of Maximum Lift Effects on Realistic High-Lift Commercial-Aircraft Configurations within the European Project EUROLIFT II, AIAA-Paper-2007–4299. AIAA, 2007.
[154] J.P. Slotnick, Integrated CFD validation experiments for prediction of turbulent separated flows for subsonic transport aircraft, STO-MP-AVT-307 (2019). Paper 6. NATO.
[155] S.E. Sherer, M.R. Visbal, R.E. Gordnier, T.O. Yilmaz, D.O. Tockwel, 1303 unmanned combat air vehicle flowfield simulations and comparison with experimental data, AIAA Journal of Aircraft 48 (3) (2011) 1005–1019.
[156] G.M. Billman, R.A. Osborne, High L/D extended range/payload fighter aircraft technology. AFRL-VA-WP-TR-1999-3084. US Air Force Research Laboratory, Air Vehicles Directorate (1998).
[157] S.J. Woolvin, A Conceptual Design Study of the 1303 UCAV Configuration, AIAA, 2006. AIAA 2006-2991.
[158] R.M. Cummings, A. Schütte, Integrated computational/experimental approach to unmanned combat air vehicle stability and control estimation, AIAA Journal of Aircraft 49 (6) (2012).
[159] Numerous, Special section: SACCON UCAV, AIAA Journal of Aircraft 49 (6) (2012) 1541–1651.
[160] RTO, Assessment of Stability and Control Prediction Methods for NATO Air and Sea Vehicles, RTO-TR-AVT-161. NATO, RTO, 2012.
[161] N.T. Frink, M. Tormalm, S. Schnidt, Three unstructured computational fluid dynamics studies on generic uninhabited combat air vehicle, AIAA Journal of Aircraft 49 (6) (2012) 1619–1637.
[162] A. Schütte, D. Hummel, S.M. Hitzel, Flow physics analyses of a generic unmanned combat aerial vehicle configuration, AIAA Journal of Aircraft 49 (6) (2012) 1638–1651.
[163] STO, Extended Assessment of Stability and Control Prediction Methods for NATO Air Vehicles, STO-TR-AVT-201. NATO, STO, 2016.
[164] STO. Multi-Disciplinary Design and Performance Assessment of Effective, Agile NATO Air Vehicles, STO-TR-AVT-251. NATO, STO, 2021.
[165] J.E. Lamar, Cranked Arrow Wing (F-16XL-1) Flight Flow Physics with CFD Predictions at Subsonic and Transonic Speeds, RTO-MP-069(I), Paper 44. NATO, RTO, 2003.
[166] RTO, Symposium on Advanced Flow Management. Part A – Vortex Flows and High Angle of Attack for Military Vehicles, RTO-MP-069(I). NATO, RTO, 2003.
[167] C.J. Obara, J.E. Lamat, Overview of the cranked-arrow wing aerodynamics project international, AIAA Journal of Aircraft 46 (2) (2009) 355–368.
[168] Numerous, Specfial section: prediction of F-16XL flight-flow physics, AIAA Journal of Aircraft 46 (2) (2009) 354–441.
[169] Numerous, Special section: prediction of F-16XL IN-flight aerodynamics, AIAA Journal of Aircraft 54 (2) (2017) 377–455.
[170] Numerous. Special Section, F-16XL flight aerodynamics predictions at a high angle of attack, AIAA Journal of Aircraft 54 (6) (2017) 2013–2114.
[171] A. Elmiligui, K. Abdol-Hamid, P.A. Cavallo, E.B. Parlette, USM3D simulations for the F-16XL aircraft configuration, AIAA Journal of Aircraft 54 (2) (2017) 417–427.
[172] A. Rizzi, J.M. Luckring, What was learned in predicting slender airframe aerodynamics with the F-16XL aircraft, AIAA Journal of Aircraft 54 (2) (2017) 444–455.
[173] A.J. Lofthouse, R.M. Cummings, Numerical simulations of the F-16XL at flight-test conditions using delayed detached-eddy simulation, AIAA Journal of Aircraft 54 (6) (2017) 2077–2099.
[174] J.M. Luckring, M.A. Park, S.M. Hitzel, A. Jirásek, A.J. Lofthouse, S.A. Morton, et al., Synthesis of hybrid computational fluid dynamics results for F-16XL aircraft aerodynamics, AIAA Journal of Aircraft 54 (6) (2017) 2100–2114.
[175] A. Schütte, R.M. Cummings, T. Loeser, An integrated computational/experimental approach to X-31 stability & control estimation, Aero. Sci. Technol. 20 (2012) 2–11.

[176] Numerous Special Issue, The X-31, Aero. Sci. Technol. 20 (1) (2012) 2–60.
[177] O.J. Boelens, CFD analysis of the flow around the X-31 aircraft at high angle of attack, Aero. Sci. Technol. 20 (2012) 38–51.
[178] A. Schütte, O.J. Boelens, M. Oelhke, A. Jirásek, T. Loeser, Prediction of the flow around the X-31 aircraft using three different CFD methods, Aero. Sci. Technol. 20 (2012) 21–37.
[179] N.J. Taylor, Summary of Findings Concerning the Prediction of Vortex Flow Interactions about Generic Missile Configurations, STO-TR-AVT-316 Chapter 11. NATO, STO, 2023.
[180] S.M. Hitzel, Status of Vortex Interaction on Combat Aircraft - Physics Understood, Simulation Tool Demands, Quality & Cost, 2023. STO-TR-AVT-316 (Chapter 21). NATO, STO.
[181] STO, Vortex Interaction Effects Relevant to Military Air Vehicle Performance, STO-TR-AVT-316. NATO, STO, 2023.
[182] J.M. Luckring, N.J. Taylor, S.M. Hitzel, Introduction: Vortex Interaction Aerodynamics Relevant to Military Air Vehicle Performance, STO-TR-AVT-316 Chapter 1. NATO, STO, 2023.
[183] M. Vissoneau, E. Guilmineau, Computational Analysis of Subsonic Vortex Interaction on Multi Swept Delta Wing Configurations. STO-TR-AVT-316, STO, NATO, 2024 (Chapter 14).
[184] T.L. Jeans, D.R. McDaniel, R.M. Cummings, W.H. Mason, Aerodynamic analysis of a generic fighter using delayed detached-eddy simulation, AIAA Journal of Aircraft 46 (4) (2009) 1326–1339.
[185] J. Slotnick, A. Khodadoust, J. Alonso, D. Darmofal, W. Gropp, D. Mavriplis, CFD Vision 2030 Study: A Path to Revolutionary Computational Aerosciences, NASA, 2014. NASA/CR–2014-218178.
[186] STO, Use of Computational Fluid Dynamics for Design and Analysis: Bridging the Gap between Industry and Developers, STO-MP-AVT-366. NATO, STO, 2022.
[187] A. Winkler, G. Heller, Virtualization of Military Aircraft Design by Means of CFD, STO-MP-AVT-366-KN1P. NATO, 2022.
[188] N. Leppard, Industrial Use and Future Requirements for Computational Fluid Dynamics in Support of Platform Design and Analysis – A BAE Systems Perspective, STO-MP-AVT-366 Paper 1. NATO, 2022.
[189] B.R. Smith, M.A. McWaters, Aerodynamic database requirements for the detailed design of tactical aircraft: implications for the expanded application of CFD, STO-MP-AVT-366 Paper 2. NATO (2022).
[190] P.R. Spalart, V. Venkatakrishnan, On the role and challenges of CFD in the Aerospace industry, Aeronaut. J. 120 (1223) (2016) 209–232.
[191] E.J. Nielsen, The impact of emerging architectures on engineering and leadership class computational fluid dynamics, big compute [cited 2024 February 28. Available from: https://bigcompute.org/bc22-speaker-series/the-impact-of-emerging-architectures-on-engineering-and-leadership-class-computational-fluid-dynamics/, 2022.
[192] P.S. Volpiani, J.B. Chapelier, A. Schwöppe, J. Jägersküpper, S. Champagneux, Simulating the common research model using the new CFD software from ONERA. DLR, and Airbus, AIAA Paper 2023-3275. AIAA, 2023.
[193] S. Görtz, Private Communication, 2023.
[194] G. Subbian, R. Radespiel, Assessment of extensions for an eddy viscosity turbulence model for vortical flows, in: A. Dillmann, G. Heller, E. Krämer, C. Wagner, C. Tropea, S. Jakirlić (Eds.), New Results in Numerical and Experimental Fluid Mechanics XII, Springer, 2018, pp. 131–141.
[195] A.P. Singh, S. Medida, K. Duraisamy, Machine-learning-augmented predictive modeling of turbulent separated flows over airfoils, AIAA J. 55 (2017) 2215–2227.
[196] K. Duraisamy, G. Iaccarino, H. Xiao, Turbulence modeling in the age of data, Annu. Rev. Fluid Mech. 51 (2019) 357–377.
[197] S.A. Morton, Bridging the Gap between High-Fidelity Multi-Disciplinary Simulation and the Design of Military Systems with Physics-Based Surrogates, NATO, STO, 2022. STO-MP-AVT-366 Paper 11.
[198] J.M. Luckring, S. Shaw, W.L. Oberkampf, R.E. Graves, Model validation hierarchies for connecting system design to modeling and simulation capabilities, Prog. Aero. Sci. 142 (2023).
[199] S. Shaw, J.M. Luckring, W.L. Oberkampf, R.E. Graves, Exploitation of a validation hierarchy for modeling and simulation, AIAA J. (2022).
[200] K.E. Wilcox, D. Bingham, C. Chung, J. Chung, C. Cruz-Neira, C. Grant, et al., Foundational Research Gaps and Future Directions for Digital Twins (2023): National Academies of Sciences, Engineering, and Medicine, National Academies Press, 2023.
[201] Rumsey CL. Langley research center trubulence modeling resource. [Online]. [cited 2022. Available from: https://turbmodels.larc.nasa.gov/easmko.html.